Award Number:
W81XWH-11-2-0109

TITLE:
Toward Development of a Field-Deployable Imaging Device for TBI

PRINCIPAL INVESTIGATOR:
Pierre D. Mourad, Ph.D.

CONTRACTING ORGANIZATION:
University of Washington, Seattle, WA 98107

REPORT DATE:
March 2013

TYPE OF REPORT:
annual r

PREPARED FOR: U.S. Army Medical Research and Materiel Command
Fort Detrick, Maryland 21702-5012

REPORT DOCUMENTATION PAGE

Form Approved
OMB No. 0704-0188

1. REPORT DATE	**2. REPORT TYPE**	**3. DATES COVERED**
March 2013	annual	15 February 2012-14 February 2013

4. TITLE AND SUBTITLE

Toward Development of a Field-Deployable Imaging Device for TBI

5a. CONTRACT NUMBER

5b. GRANT NUMBER
W81XWH-11-2-0109

5c. PROGRAM ELEMENT NUMBER

6. AUTHOR(S)

Pierre D. Mourad, PhD

E-Mail: pierre@apl.washington.edu

5d. PROJECT NUMBER

5e. TASK NUMBER

5f. WORK UNIT NUMBER

7. PERFORMING ORGANIZATION NAME(S) AND ADDRESS(ES) AND ADDRESS(ES)
University of Washington,
Seattle WA 98195-6470

8. PERFORMING ORGANIZATION REPORT NUMBER

9. SPONSORING / MONITORING AGENCY NAME(S) AND ADDRESS(ES)
U.S. Army Medical Research and Materiel Command
Fort Detrick, Maryland 21702-5012

10. SPONSOR/MONITOR'S ACRONYM(S)

11. SPONSOR/MONITOR'S REPORT NUMBER(S)

12. DISTRIBUTION / AVAILABILITY STATEMENT
Approved for Public Release; Distribution Unlimited

13. SUPPLEMENTARY NOTES

14. ABSTRACT

Improvised explosive devices (IEDs) produce head injuries in nearly a majority of surviving soldiers. Most brain-injured soldiers do not, however, receive the necessary, rapid brain imaging studies as would their civilian counterparts. Instead they are flown to rear-echelon medical service centers such as in Germany for those studies, as well as additional medical care. There exists, therefore, a critical need for robust brain imaging systems at and near the battlefield. This gap in patient care reduces the quality of care and potentially, therefore the quality of life of injured soldiers. This gap also defines a critical need for rugged, field deployable systems capable of imaging injured brain. For a variety of reasons it is reasonable to expect that changes in the stiffness of brain accompany TBI, and that ultrasound-based 'sonoelastic' imaging modalities responsive to some measure of stiffness might offer a useful means for imaging the changes to brain due to TBI. Use of such systems in and near the field should improve clinical outcome for patients suffering from TBI. Our long-term goal is to develop a field deployable brain imaging system, capable of transcranial application, responsive to brain stiffness.

15. SUBJECT TERMS
traumatic brain injury, ultrasound, sonoelasticity, brain imaging.

16. SECURITY CLASSIFICATION OF:			**17. LIMITATION OF ABSTRACT**	**18. NUMBER OF PAGES**	**19a. NAME OF RESPONSIBLE PERSON**
a. REPORT	**b. ABSTRACT**	**c. THIS PAGE**			USAMRMC
U	U	U	UU	105	**19b. TELEPHONE NUMBER** *(include area code)*

Table of Contents

Page

Introduction…….…….. pg #4

Body…….. pg #5

Key Research Accomplishments…….. pg #16

Reportable Outcomes…… pg #17

Conclusion…… pg #18

Appendix..... pg #19

INTRODUCTION – subject. Improvised explosive devices (IEDs) produce head injuries in nearly a majority of surviving soldiers. Most brain-injured soldiers do not, however, receive rapid brain imaging studies as would their civilian counterparts. Instead they are flown to rear-echelon medical service centers such as in Germany for those studies, as well as additional medical care. This is because magnetic resonance imaging is unavailable in or near the theatre of war (and a bad idea for many patients because of the presence of metal fragments) and because of the lack reliably operational CT machines at medical centers in Iraq. In the mean time, due to the lack of adequate neuro-imaging, acute neurosurgical care in response to closed TBI often requires a complete hemicraniectomy (removal of one side of the patient's skull) simply to assay the extent and location of injured brain. There exists, therefore, a critical need for robust brain imaging systems at and near the battlefield. Also, more subtle brain injuries are apparent clinically but difficult to definitively diagnose, hence treat. These gaps in patient care reduce the quality of care and potentially, therefore the quality of life of injured soldiers. This gap also defines a critical need for rugged, field deployable systems capable of imaging injured brain.

INTRODUCTION - purpose. For a variety of reasons (summarized in a recent book chapter of mine – Mourad, 2013) it is reasonable to expect that changes in the stiffness of brain accompany TBI, and that ultrasound-based 'sonoelastic' imaging modalities responsive to some measure of stiffness might offer a useful means for imaging the gross and subtle changes to brain due to TBI. Use of such systems in and near the field should improve clinical outcome for patients suffering from TBI. Our long-term goal is to develop a field deployable brain imaging system responsive to brain stiffness. Our system would do so through the use of ultrasound applied transcranially.

INTRODUCTION – scope of the research. To met the goal of this proposal we sought to test the following hypothesis: Rodent brain after closed TBI (blast, controlled cortical impact (CCI); ischemic stroke) manifest spatial patterns of endogenous and exogenous tissue displacement, hence patterns of brain-tissue stiffness, sufficient to map and identify the extent of each of hemorrhage, edema, and TAI, as tested via the following iterative aims.

Specific Aim #1: Quantify via histology and MR the spatial position and extent of each of hemorrhage, edema and TAI within each of the blast and CCI models of brain injury.

Specific Aim # 2: Directly measure the intrinsic stiffness of brain tissue of different types: normal gray and white matter; hemorrhagic brain; edematous brain; traumatized axons.

Specific Aim # 3: Use displacement-based ultrasound to image intrinsic brain tissue stiffness of normal versus traumatized rodent brains and their component parts.

Specific Aim #1: Quantify via histology and MRI the spatial position and extent of each of hemorrhage, edema and diffuse axonal injury (DAI) within each of the blast and CCI models of brain injury, with comparable studies for ischemic stroke.

Task (1): Generate closed TBI (mild and moderate-to- severe) in rats using blast methodology.

1) We will perform this work in Fall 2013-Winter 2013.

Task (2): Generate closed TBI (mild, moderate-to-severe) using CCI methodology in 'mito' mice and in rats and ischemic stroke using an occlusion model in mice.

2) We at each of UW (University of Washington) and UVa (University of Virginia) have achieved all of these goals. Of particular interest is the TBI induction, whose critical parts include (a) the cranial window, made after exposing the cranium of the animal while it was under anesthesia. We made it to have a radius of 2mm in order to fit the tip of the controlled cortical impact device (Model: AMS 201; AmScien Instruments, Richmond, VA - Figure 1). The cortical impact device was then used to create a mild TBI (depth of injury = 0.5mm; rod speed = 3m/s) through the craniotomy.

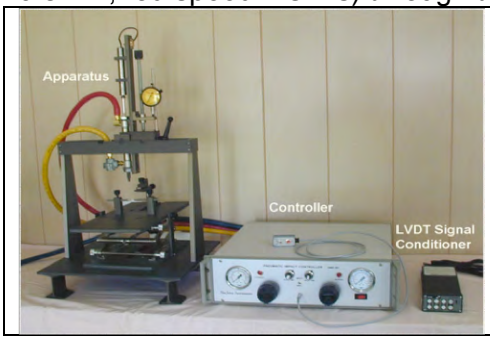

Figure 1. The device here creates a controlled cortical impact in the cortex of mice and rats. The working element is the 'apparatus' where the rodents are placed in order to receive the impactor tip on their exposed brain. Red and yellow hoses facilitate movement of compressed gases that actuate the device as controlled by the ancillary devices.

Task (3): MR image rodent brains.

3) UVa has performed its all of its of MRI studies of CCI rats (Figure 2a,b). They are now working on the co-registration of those MR images with immunohistochemical images, in order to develop direct correlation of the brain-injury features in each imaging modality (Figure 2c). The tools we are creating to accomplish this task will likely find clinical application for bringing together different imaging modalities, as well as non-imaging data, for TBI and other etiologies. Specifically, spatial normalization of both brain histological slides and corresponding MRI are achieved primarily through the various tools found within the Advanced Normalization Tools (ANTs) repository. The coordinate system for statistical analysis is defined by constructing a population-specific MRI rat template from individual rat images. Individual subject brain histological slides are synthesized into a brain volume via slice stacking with intra-slice registration to smooth out any possible discontinuities derived from the histology protocol. These whole brain histologies are then registered to their corresponding MRI. The transforms used to derive the template are then use to warp each whole brain histology to the standardized coordinate system for subsequent analysis.

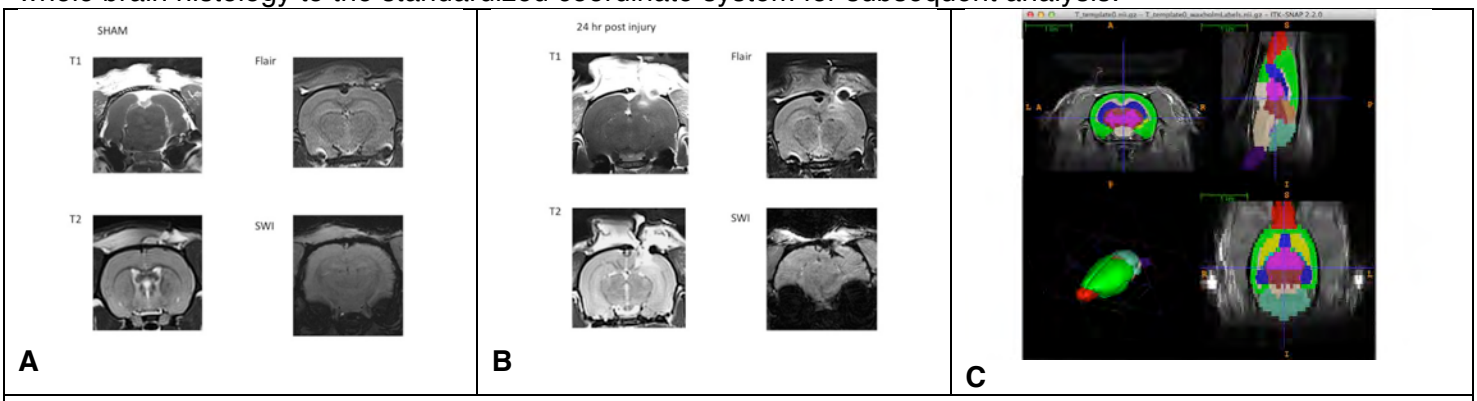

Figure 2. Images of rat brain after (sham) controlled cortical impact (CCI) injury. (A) shows various MRI images of coronal views of sham injured rat brains. **(B)** shows various comparable MRI images of injured rat brains. The injury manifests in the upper right-hand quadrant of the brain, encompasses the cortex down to the hippocampus. 'T1' highlights the basic structural abnormality generated by the CCI, 'T2' highlights fluid buildup at the site of CCI, 'Flair' refers to fluid attenuated inversion recovery that suppresses fluid-specific signals to highlight changes in tissue structure, 'SWI' refers to susceptibility weighted imaging that is sensitive to venous blood and hemorrhage. **(C)** shows co-registration of MRI images with a rat-brain atlas, each of the major components of brain highlighted in different colors. Follow-on co-registration of the atlas with histological images will complete a useful triad of MRI/Atlas/histology.

Task (4): Immunohistochemical assays.

4a) Each of UW and UVa have performed all of their immunohistochemical assays for CCI rats (e.g., Figure 5e,f). At UW we are using those results to finish two papers detailing the ability of different modalities of ultrasound (shear-wave imaging (SWE) and vibro-acoustography) to detect traumatic brain injury (TBI), described below under Specific Aim #3.

4b) We at UW have collected wide field fluorescent microscopy brain-tissue images from mito-mice subjected to TBI via CCI (Figure 3). (These mice have the unique property that the mitochondria within the neurons in their brain fluoresce when healthy.) We have identified unanticipated *increases* in fluorescence at the site of injury, pointing to possible decreases in the ability of the neurons and axons to transport mitochondria, or, to changes in mitochondria morphology and function. These changes may be amenable to a variety of drug treatments.

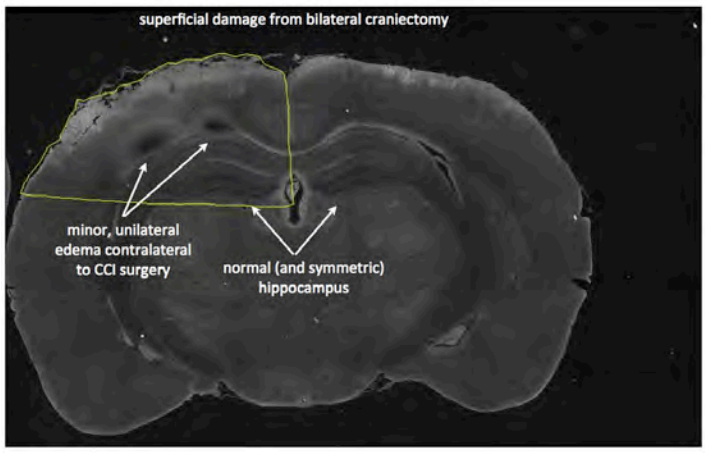

A

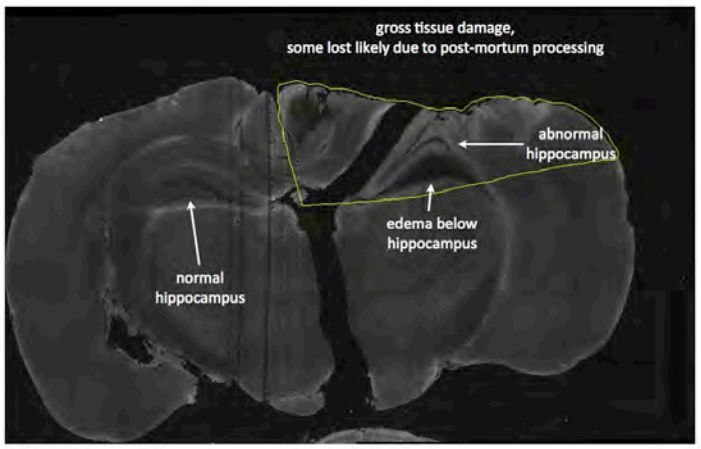

B

Figure 3. mitoMice brains – lighter gray has greater concentration of mitochondria than darker gray. **(A)** This figure shows a coronal slice of brain subjected to the initial surgery to create TBI via CCI then the subsequent surgery to widen the craniectomy ipsilateral to the sham surgery site and contralateral to the sham surgery site. **(B)** This figure shows a coronal slice of brain subjected to actual CCI. Note the enhanced fluorescence within the hippocampus (as well as edema and large-scale necrosis), suggestive of mitochondrial dysfunction and/or reduced transport, each of which is potentially amenable to treatment with existing, FDA approved drug treatments

Specific Aim # 2: Directly measure the intrinsic stiffness of brain tissue of different types: normal gray and white matter; hemorrhagic brain; edematous brain; ischemic brain; traumatized axons.

Task (5): Calibrate indenter system and apply it in vitro as well as to rodent brain tissue samples dominated by one of each of normal gray and white matter; hemorrhagic brain; edematous brain; traumatized axons.

5) This system is calibrated and working after quite extensive development of the technique. We have shown statistically significant changes in brain tissue viscoelastic structure at the site of CCI – Figure 4. We are writing up this paper now, for submission in spring 2013 (Gabler et al, 2013).

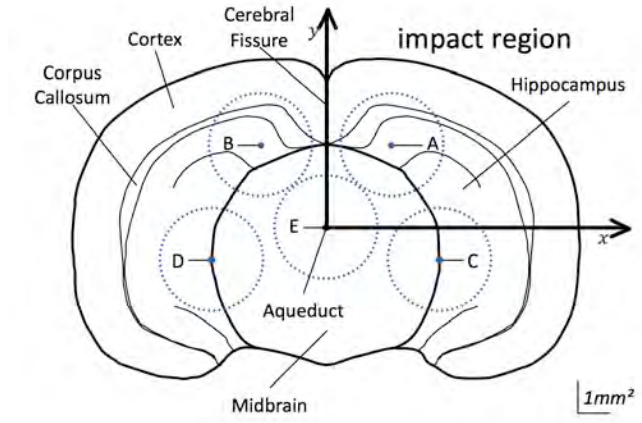

A

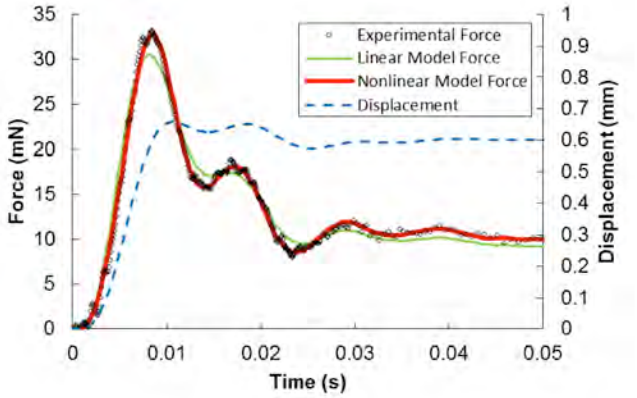

B

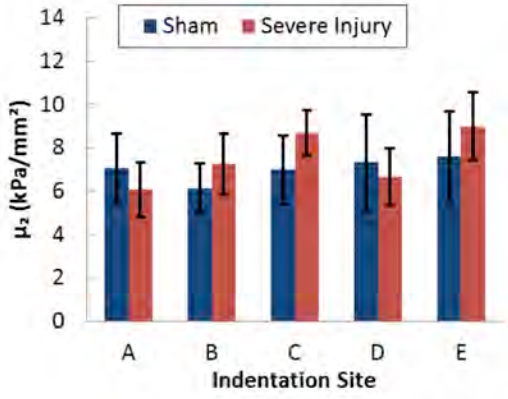

C

Figure 4 shows our indenter results for CCI rats. Figure **(A)** shows a schematic of indenter position measurements while Figure **(B)** shows measurements of rat-brain displacement (horizontal axis) versus measured elastic response in milliNewtons, all as a function of time, along with associated mathematical modeling. Figure **(C)** shows the results that demonstrate changes in the viscoelasticity of brain after CCI at the various spots within the brain from which data was collected.

Specific Aim # 3: Use displacement-based ultrasound to image intrinsic brain tissue stiffness of normal versus traumatized rodent brains and their component parts.

Task (6): Optimize commercial ultrasound-imaging device based on measurement of exogenous and endogenous brain palpation.

6a) We have established a procedure for optimizing the analysis of images from the commercial ultrasound imaging system, based on exogenous brain palpation by the SuperSonic Imagine (SSI) machine via the acoustic radiation force and subsequent monitoring of the propagation of the shear wave. We have performed this procedure for stroke animals and published the results, where this grant supported the analysis of that data. In Figure 5 we demonstrate this analysis procedure, along with the accompanying histopathology analysis, for TBI. Below in Task 8 we show the results of this analysis applied to TBI in each of mice and rats induced by the CCI method.

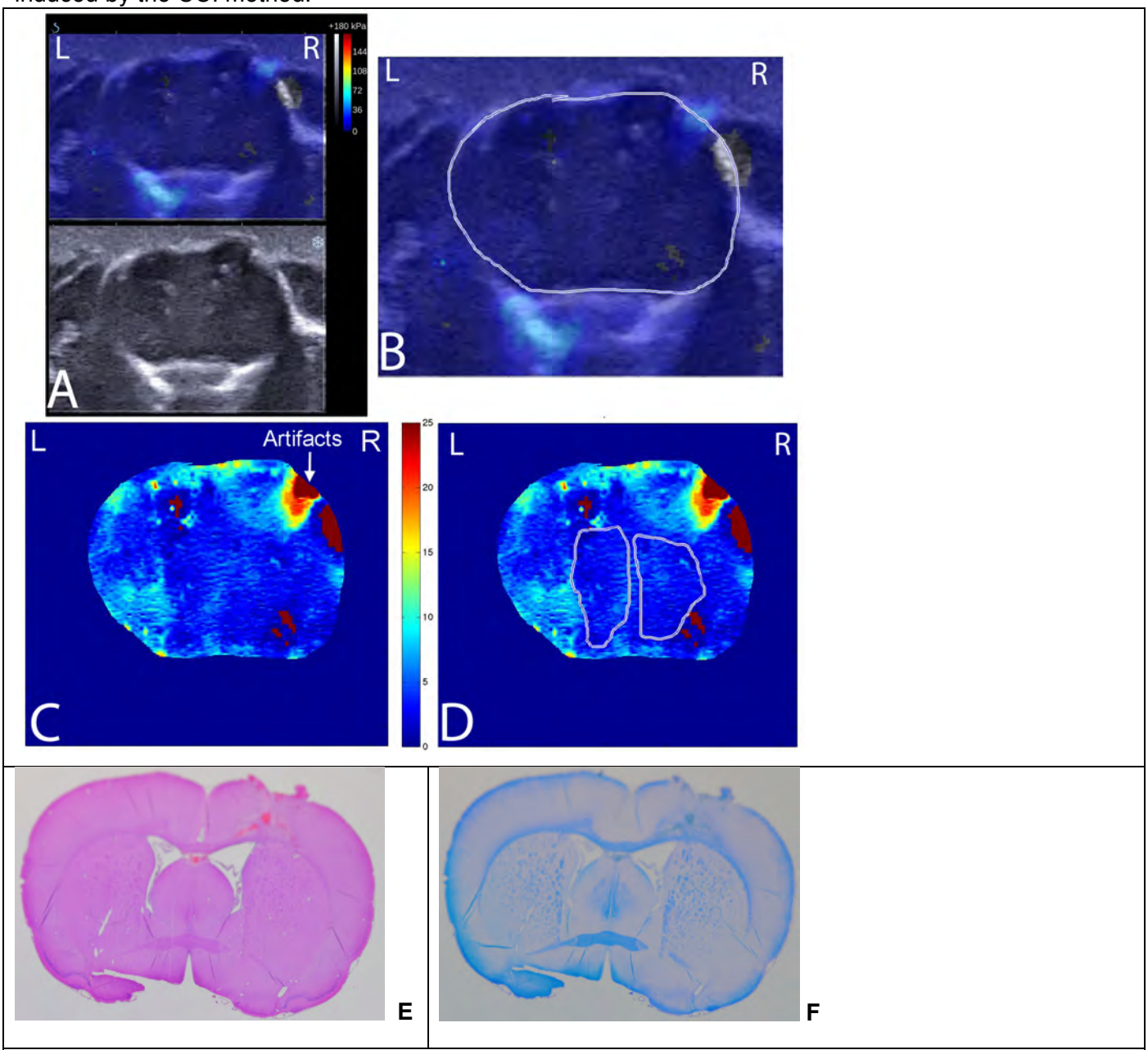

Figure 5. Image Processing. (A) Aixplorer images in SWE mode (top) and B-mode (bottom) (B) The brain region was selected from the elastographic image (0-180 kPa) with reference to the B-mode image. (C) The SWE image of the brain was rescaled to 0-35 kPa to enhance the contrast. (D) Regions of Interest selected manually to avoid skull and artifacts (large values of Young's Modulus greater than that of brain). (E) Hematoxylin and Eosin and (F) Cresyl Violet staining of corresponding brain.

6b) We have also identified a fundamental limitation of the commercial system, discussed in Figure 6.

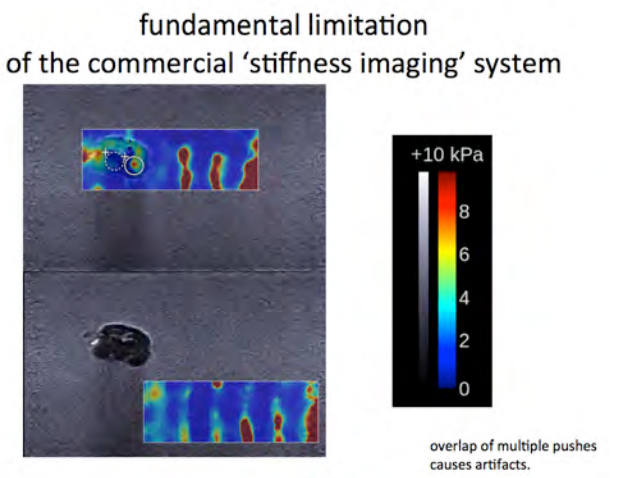

Figure 6. Here we demonstrate intrinsic artifacts within the shear-wave images generated by the commercial imaging machine (the SSI). We show two B-mode images (shades of gray), each with the superposition of a shear-wave image (color, with its scale of kPa) of brain within alginate. In the top figure, the brain sits within the shear-wave template. In the bottom figure, the brain sites outside of the shear-wave template. Critical here, in each shear-wave image there exist evenly spaced maxima in shear modulus. We believe these maxima represent artifacts that arise from the specific image processing built into the commercial system combined with their use of multiple shear waves to create a given image.

Task (7): Optimize research ultrasound-imaging device based on measurement of exogenous and endogenous brain palpation.

7a) We can generate images of shear-wave propagation using our research ultrasound-imaging device (the VUE system) – Fig. 7a. We have minimized image artifacts in alginate through identification of an efficient means of tracking the propagation speed of the shear wave. In addition, we have compared our analysis of shear-wave propagation data from the commercial device (the SSI – Fig. 7b) and from our research device derived from the same alginate (comparison in Fig. 7c). The presence of enhanced vertical maxima in the shear-modulus maps from the SSI vs from the VUE demonstrates that those maxima are intrinsic to the data generated by the SSI likely due to residual reverberation of multiple propagating shear waves.

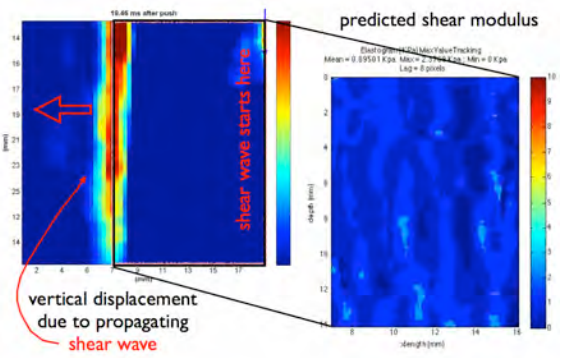

A

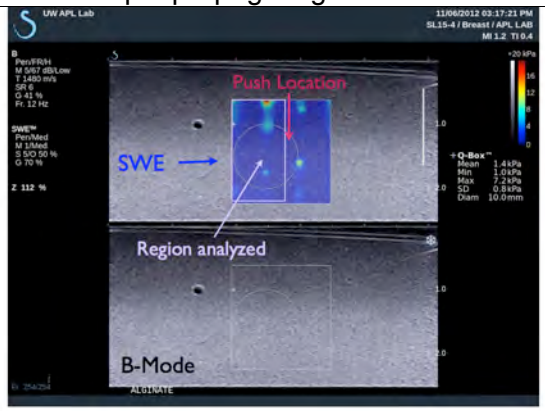

B

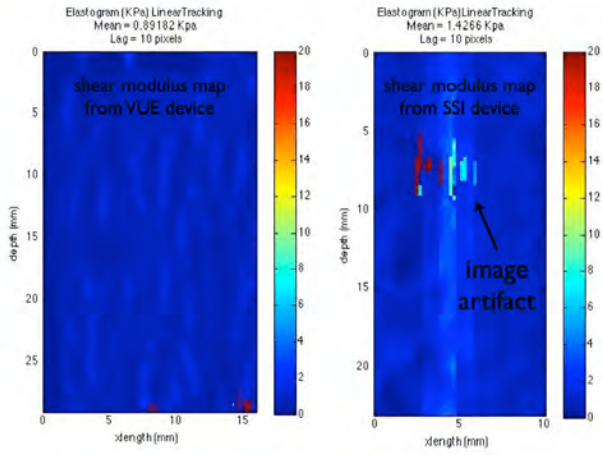

C

Figure 7. Quantification of shear wave propagation in alginate – research versus commercial system. (A) We can create a focal and vertically elongated, vertical push within alginate (and tissue – below) that generates a horizontally propagating shear wave, whose speed we can quantify and translate via a commercial algorithm into a prediction of the shear modulus. **(B)** The commercial system generates simultaneous images of B-mode and shear-wave elastography (SWE), here of alginate. Note the relatively large, vertically oriented peaks in predicted shear modulus. **(C)** Here we compare predicted shear modulus images taken by our VUE (research) and by our SSI (commercial) devices and derived via our analysis. An image artifact remains in the SSI image, even though we used our analysis. We will therefore move forward with our VUE system in future studies.

7b) We have tested on sham and actual TBI rats an exogenous brain palpation system based on vibrating brain with focused ultrasound, whose methodology we review in Figure 8a and demonstrate capable of measuring acoustic emissions from brain (Figure 8b).

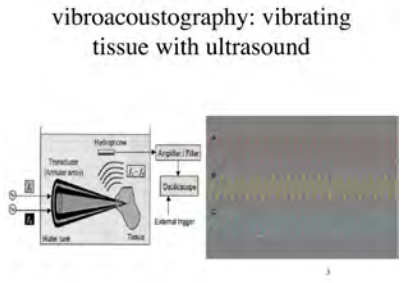

A

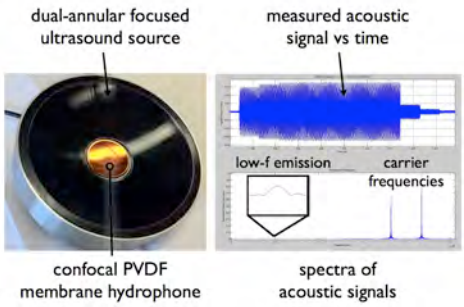

B

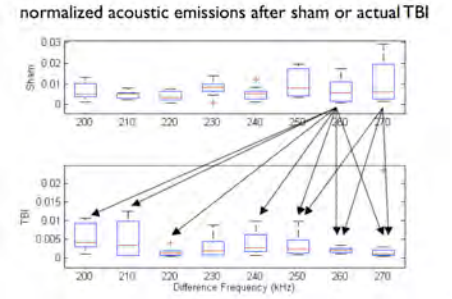

C

Figure 8. Vibro-acoustography as a means of assaying for the presence of traumatic brain injury. **(A)** In vibro-acoustography, a dual-transducer device ('transducer (annular array)") emits two, separate pulses of ultrasound at two different, but close frequencies – pulse train 'A' and 'B'. At their mutual focus, high frequency oscillations move the tissue slightly; their beat frequency generates a low-frequency emission, itself sampled from a separate hydrophone placed either in the water tank or within the iFU source itself for *in vivo* applications. **(B)** This figure shows our device and real data rather than the conceptualization of Figure 6A, highlighting a measured waveform that demonstrates the signal generated by the two, spatially overlapping high frequency iFU signals, and small amplitude, low-frequency acoustic emissions. **(C)** TBI rats show reduced acoustic emissions across a range of frequencies compared to sham TBI rats (N =5,3, respectively). Note that there does not exist a variation with frequency among the sham only and TBI only data, only between the data.

7c) To create endogenous ultrasound imaging results we have demonstrated that we can measure the pulsation of mouse brains completely enclosed within their crania, pulsations created by both their breathing and their heart beat (Figure 9). We will turn our attention to mice subjected to TBI next year.

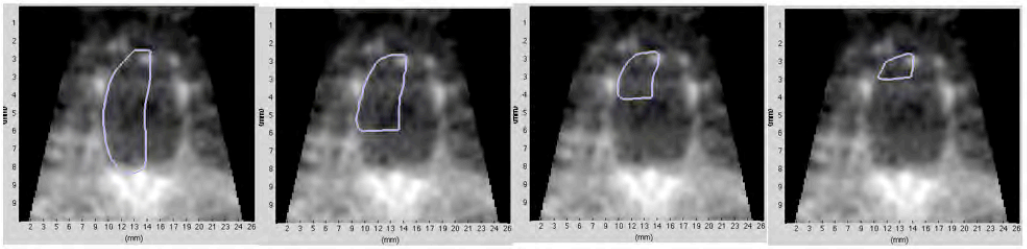

selection of various regions of interest from within a VUE-derived B-mode outline of a live mouse brain.

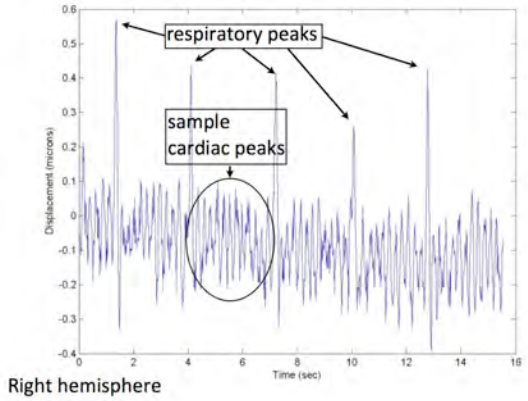

Figure 9 demonstrates our ability to collect tissue pulsatility images of mouse brain *in vivo* within the mouse's completely enclosed cranium. The top photo shows a series of images comprised of ultrasound-derived outline of a mouse head via B-mode imaging, over which we have superimposed a region of interest for which we will derive a measure of the average brain-tissue displacement. That measure, as a function of time, demonstrates both respiratory peaks (e.g., when the mouse breathes) as well as cardiac peaks (when the heart beats). Note that the respiratory peaks can approach 1 micron in diameter, while the cardiac peaks measure one tenth of that, on average.

Task (8): Image normal versus damaged rodent brains with commercial and research ultrasound devices.

(8a) We show statistically significant variations in acoustic emissions from within TBI rat brain relative to sham TBI rat brain, with data collected a few millimeters away from the TBI site (Figure 8c, above). We will next refine then write up these results (Dever et al, 2013) then begin design of a system capable of application to humans.

(8b) We have finished use of the commercial SSI system *without any modification* on stroke mice, with analysis of the data supported by the present grant. We have published this work Xu et al (2013a).

(8c) We have finished use of the commercial SSI system *without any modification* on TBI mice and rats. While we could not image brain damage with that commercial system, we could detect it (Figure 10). We are writing up these results now. Specifically, these results demonstrate changes in hemispherically averaged shear modulus for each of the hemispheres due to ipsilateral TBI. The ipsilateral decrease in shear modulus relative to control is consistent with the combination of focal ischemia and wide spread edema formation after CCI, a well-established phenomenon in this animal model for TBI. Unexpectedly, we also see a contralateral increase in shear modulus relative to control by 24 hours after CCI injury, consistent with other's observation of reduction of blood flow contralateral to injury as well as elevated global ICP. We report these results in a submitted paper (Xu et al, 2013b)

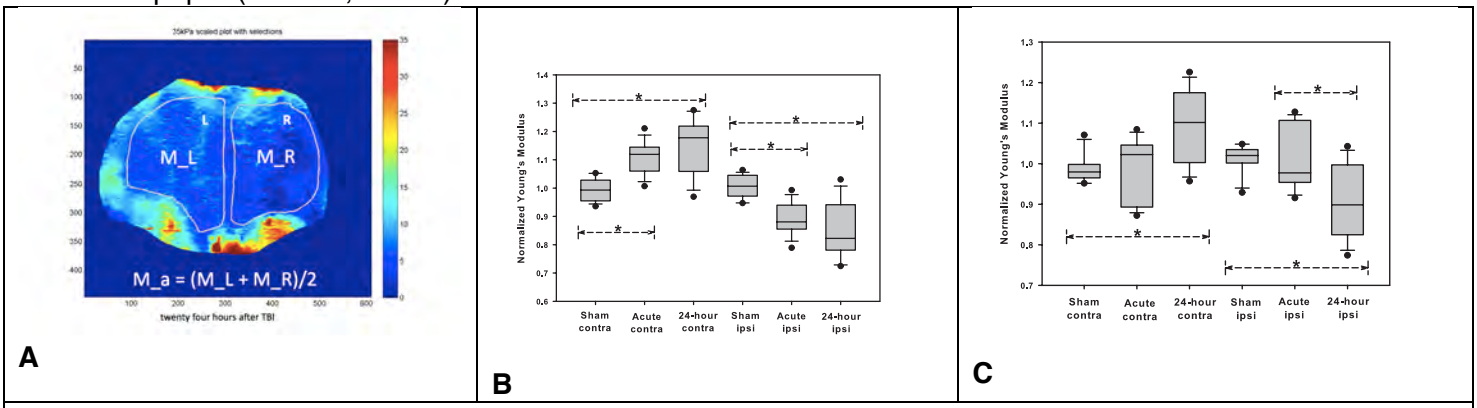

Figure 10 demonstrates our ability to detect changes in intra-hemispheric brain stiffness after TBI using our commercial imaging system. (A) Coronal slice of 'shear-modulus image' [replete with image artifacts – the hot colors] of brain-tissue stiffness of rat brain 24 hours after TBI induced via the CCI methods, with associated regions of interest [each of M_L and M_R] along with specification of their average value [M_a]. Imaging artifacts continue to manifest in these images, here as hot colors around the periphery of the image. Nonetheless, in this example, as well as on average for each of **(B)** mice and **(C)** rats the ipsilateral hemisphere has a lower mean, normalized shear modulus than the contralateral hemisphere by 24 hours after CCI injury. These values change also relative to sham TBI values, which themselves agree between hemispheres.

Task (9): Compare images of strain, and of bulk and shear modulus of brain with histological and MR-based images of hemorrhage, edema, ischemia and TAI.

9) We intend to start this research in Fall 2013–Winter 2014, after we deploy our VUE research device at the University of Virginia.

Task (10): Compare images of strain, and of bulk and shear modulus of brain tissue with images of bulk and shear modulus derived by assigning directly measured values of bulk and shear modulus to portions of histological images.

10) We intend to start this research in Fall 2013–Winter 2014, after we deploy our VUE research device at the University of Virginia.

Task (11): Generate first-order specifications for a device capable of imaging TBI in humans.

11) We can now specify one of what we anticipate to be three devices capable of imaging TBI in humans. That device will emit diagnostic ultrasound with a frequency around 2 MHz, with its data analyzed via 'tissue pulsatility imaging' [TPI] algorithms we have developed. The other two devices we anticipate will involve (a) vibro-acoustography in combination with TPI and (b) transcranial SWE.

KEY RESEARCH ACCOMPLISHMENTS

- We have developed and demonstrated *in vivo* a new means of detecting TBI on generation and detection of focal, low-frequency vibration within brain via a process known as vibro-acoustography.
- We have begun design of a novel ultrasound-based imaging system capable of translating diagnostic ultrasound images, derived transcranially, into images of endogenous brain-tissue displacement that highlight focal TBI, based on our ability to image *mouse- and rat-brain* pulsatility.
- We have observed changes in hemispherically averaged brain-tissue stiffness in TBI generated by the controlled cortical impact (CCI) method in mice and rats consistent with physiological changes in brain observed in rodent models of TBI as well as in patients with TBI. These observations include ipsilateral edema and hemorrhage formation (observed in rodents and in patients) and short-term contralateral reduction in blood flow (observed in patients and sometimes in rodents) along with a reduction in cerebral perfusion pressure.
- We have made progress on the image-analysis methods based on tracking propagating shear-wave images necessary to resolve intra-hemispheric changes in brain *in vivo* due to TBI. We will likely have to place the brains within alginate to successfully capture images.
- We are developing a means of co-registering MR and immunohistochemical images, in order to develop direct correlation of the brain-injury features in each imaging modality. The tools we are creating to accomplish this task will likely find clinical application, for bringing together different imaging modalities for TBI and other etiologies.
- We have demonstrated our direct means of measuring brain-tissue stiffness from rats, data that will give us ground-truth measurements of that stiffness for comparison with our ultrasound-based means of imaging brain-tissue stiffness variations in the context of TBI.
- We anticipate deployment at UVa of a research ultrasound imaging system capable of generating tissue-pulsatility and shear-wave images of the brains of rats after blast injury. Successful collection and analysis of these data, along with direct measures of brain-tissue stiffness and associated MRI and immunohistochemical images, will allow us to demonstrate in a direct fashion that we can use ultrasound to produce high-contrast images of damaged versus normal brain in the context of TBI.

REPORTABLE OUTCOMES

(copies of relevant documents are attached to the end of this document)

Gabler LF, Stone JR, Mourad PD, Crandall JR, Salzar RS (2013) Region Specific Viscoelastic Properties of the Adult Rat Brain under Indentation following Traumatic Brain Injury. Submitted to *Proc. Ircobi Conf.*

Mourad PD (2013), "Therapeutic Ultrasound, with an emphasis on applications to the brain" in Nakamura K, Ueha S, eds. Ultrasonic transducers - materials design and applications**.** Woodhead Publishing Ltd, pp545-568.

Xu JS, Chu S, Lee RJ, Paun M, Yao A, Murphy S, Mourad PD (2013a) Evidence of diaschisis after ischemic stroke through ultrasound-based elastography. *J. Ultrasound in Medicine.* 32(3):485-494.

Xu JS, Yao A, McClintic AM, Illian PR, Mourad PD (2013b) Traumatic brain injury can change the stiffness of brain tissue, *in vivo.* Submitted to *European Journal of Radiology.*

CONCLUSIONS

We have generated evidence supportive of the hypothesis that ultrasound-derived brain-tissue stiffness imaging using exogeneous 'palpation' of brain with diagnostic ultrasound can successfully detect changes in rat brain caused by both ischemic stroke and in TBI. We have also generated evidence supportive of the hypothesis that we can detect endogeneous palpation of roent brain by cerebral blood flow. We have made direct measurements of brain-tissue stiffness in rats *ex vivo* that show a change in brain tissue viscoelasticity due to TBI. We have nearly completed a novel means of co-registering imaging and histological data that together highlight TBI. We have begun designs of two ultrasound systems capable of creating images of TBI in humans.

Taken together, these results among the others reported here demonstrate that we are making appropriate progress, relative to our milestones, towards creation and demonstration of the ability of ultrasound to image TBI with a field-deployable device.

Region Specific Viscoelastic Properties of the Adult Rat Brain under Indentation following Traumatic Brain Injury

Lee F. Gabler, James R. Stone, Pierre D. Mourad, Jeff R. Crandall, Robert S. Salzar

Abstract Traumatic Brain Injury (TBI) is a serious health epidemic that places high societal and economic burdens on victims and their caregivers. Further, the associated neuropathological consequences that result from TBI are often complex and cause secondary injuries that are focal, diffuse and time dependent. Current computational models can predict loading and deformation associated with TBI; however, accurate knowledge of region specific material properties from both healthy and mechanically damaged brain is needed. In this study, the mechanical properties of both uninjured and traumatically injured brain tissue are presented. Adult male Sprague-Dawley rats were injured through a controlled cortical impact protocol. Ramp and hold indentation tests were performed at five locations on the surface of tissue samples excised from whole brain specimens. Force displacement data were analyzed using quasi-linear viscoelastic theory. An analysis revealed the tissue to be viscoelastic and spatially nonlinear with mechanical properties that depend on both region and level of injury. After normalizing the data, the nonlinear components of the instantaneous elastic force and shear modulus were found to be significantly lower, 26%, in the region containing the contusion cavity on severely injured samples compared to uninjured tissue at the same region in controls.

Keywords Traumatic brain injury, focal, diffuse, controlled cortical impact, mechanical damage, quasi-linear viscoelasticity

I. INTRODUCTION

Traumatic Brain Injury (TBI) is an important national health concern in the United States [1]. Approximately 1.7 million incidences and 52,000 deaths are reported annually due to automobile collisions, sports accidents, falls, and other head impacts [1]. Further, severe TBI has a high economic burden, costing nearly $76.5 billion each year in medical and societal costs [1]. On the battlefield, improvised explosive devices have led to TBI in as many as 62% of soldiers sustaining head injuries, and an estimated 360,000 service members have been affected by TBI over the past decade [2], [3]. Since the 1960s there has been a dramatic improvement in understanding the complex pathobiological behavior associated with TBI [4]. Brain injury, as a result of an impact or insult to the head, leads to a number of complex neuropathological consequences that result in further tissue dysfunction and eventually cell death [5]. However, injury quantification remains challenging because the neurochemical cascades that accompany TBI often involve complex secondary sequelae that are focal, diffuse, and time dependent [6]. A better understanding of the mechanical response of the brain during these events would improve diagnosis and treatment of TBI in both clinical and battlefield scenarios.

The material properties of brain during an injurious event were studied as early as the 1940s [7]. Not until more recently has an emphasis been placed on understanding the complex mechanical behavior of the brain during loadings that lead to TBI. Much of this can be attributed to an increase in awareness of the damaging, long-term effects following even mild brain injuries [1]-[3]. Material properties of brain are reported in the literature as viscoelastic [8]-[13], both spatially and temporally non-linear [9], [10], anisotropic [11], age-dependent [11]-[14], inhomogeneous [12], [13] and nearly incompressible [15]. Additionally, experimental factors such as specimen preparation, temperature [16] and level of hydration [14], [17] have been shown to influence these properties. There is considerable variation in the mechanical response reported in these

L.F. Gabler, B.A., J.R. Crandall, Ph.D., and R.S. Salzar, Ph.D., Department of Mechanical and Aerospace Engineering at the University of Virginia's Center for Applied Biomechanics, 4040 Lewis and Clark Drive, Charlottesville, VA 22911 USA (phone: (434) 296-7288 ext. 164, email: lfg4dc@virginia.edu). J.R. Stone, M.D., Ph.D., PI, Department of Radiology and Medical Imaging at the University of Virginia. P.D. Mourad, Ph.D., PI, Department of Neurological Surgery at the University of Washington.

studies. Much of this variation can be attributed to differences in the type of species, experimental protocols, and anatomical regions tested. Still, no definitive set of material properties exist for brain.

Computational models of TBI are commonly used to study the mechanical behavior of brain tissue during a traumatic event. Finite element modeling (FEM) can predict loading of various substructures through simulations of mild to severe TBI in rat brain [18]. These simulations have the added capability of predicting injury, because model-prediction of tissue strains were shown to correlate well with experimentally determined strain and strain rate injury tolerance criterion [19]-[21]. For more region-specific predictions of injuries, local material properties, including both traumatically injured and healthy brain tissue, need to be determined. Such knowledge would provide existing computational models with the added ability to predict the subsequent mechanical response of damaged tissue and allow for a better understanding of brain excitotoxicity beyond that of the initial trauma.

A survey of the literature revealed a number of studies that report thresholds for axonal damage. The reported mechanical limits for diffuse axonal Injury are between 0.1-0.2 Lagrangian strain at strain rates greater than $10s^{-1}$ [9], [19]-[22]. However, there is little information regarding changes in the mechanical properties of traumatically injured brain tissue. Shafieian et al. [23] used an impact acceleration model (IAM) to generate diffuse axonal injury (DAI) in the brainstem of adult male Sprague-Dawley (SD) rats. They reported a 35% reduction in the linear coefficient of the instantaneous shear modulus in injured rats compared to uninjured controls. Saxena et al. [24] studied traumatic spinal cord injury in adult female SD rats over the course of 2 and 8 weeks post injury. They observed a 50% reduction in elastic modulus for injured compared to healthy tissue. The goal of this study is to acquire accurate, region-specific material properties for both traumatically injured and uninjured rat brain to better understand the mechanical behavior of damaged tissue and to improve existing models of TBI.

II. METHODS

Animal Injury

All animal protocols were approved by the University of Virginia's Institutional Animal Care and Use Committee. Twenty adult male SD rats of average weight (mean ± SD), (320±27)gram, underwent surgical procedures for this study. Anesthesia was induced with a mixture of 4% isoflurane and 100% medical grade O_2 for 3-4 minutes in an induction chamber. Once the animals were sedated, the level of isoflurane was reduced to 2-2.5% and maintained for the duration of the surgery. The animals were then placed in a stereotaxic reference device (MyNeuroLab Leica Digital Stereotaxic Instrument, Leica Biosystems, Richmond, IL) and prepared for injury. A midline scalp incision was made along the forehead of each animal. The skin and underlying soft tissue were retracted exposing the sagittal, coronal, and lamboid sutures on the skull. A 4.5-5mm diameter hole was drilled from the skull above the right cerebral cortex exposing the dura at the coordinates of injury: A = -4mm bregma and L = 2mm (Ideal Micro-Drill™, Harvard Apparatus, Holliston, MA). An electromagnetically driven controlled cortical impact (CCI) device (MyNeuroLab Leica Impact One, Leica Biosystems, Richmond, IL) was used to deliver repeatable, severe, open head injury to nine of the animals; the remaining animals were prepared for *Sham* injury and used as controls. The 2mm diameter impact cylinder was positioned directly on the dura at the coordinates of injury. Contact between the probe tip and dura was verified via an electric circuit. The probe tip was then retracted from the dura and injury parameters were inputted to the device. Severe traumatic brain injury was delivered to the right ipsilateral cortex through a rapid 2.5mm compression of the dura, sustained for 200ms, with an initial impact velocity of 3.5m/s. In the instance of Sham injury, the impact probe was retracted from the dura, but no impact was performed on the tissue. The animals were then resuscitated and monitored for a period of twenty-four hours after which they were sacrificed and their brain tissue immediately collected.

Sample Preparation

Whole brain specimens were prepared for indentation tests immediately following tissue collection. To reduce the effects of temperature and level of hydration on the results, specimens were submerged in a physiological buffer (Millonig's Phosphate Buffer) for five minutes at room temperature (19-20)°C. Hydrated specimens were then placed into a coronal slice matrix (Braintree Scientific, Inc.) with incision planes spaced 1mm apart. Tissue cross-sections were cut to approximately 8mm in thickness from each whole brain specimen

using a 0.23mm thick razor blade (VWR Scientific, Media, PA). To accomplish this, two incisions were made in the coronal plane and parallel to each other. The first incision was made 1mm posteriorly to the injury plane at -5mm bregma and the second 8mm anteriorly to the first at 3mm bregma. In both Sham and severely injured specimens, the injury plane was identified by petechial hemorrhage on the dorsal surface of the tissue. However, in the case of a severe injury, the hemorrhage was more extensive and included a *contusion cavity*. Samples were then removed from the slicing matrix and placed on an aluminum test stage with the 5mm bregma coronal plane oriented upwards. The thickness of each sample deformed approximately 1mm under its own weight. The weight and dimensions of each sample were measured and recorded.

The coordinates of five regions, A-E, on the samples were determined using a stereotaxic reference frame [25] and are illustrated in Figure 1. Substructures of the brain under the indenter at these coordinates included both healthy and damaged tissue within the cerebral cortex, corpus callosum, hippocampus and midbrain. For severely injured samples, region A was located directly over the contusion cavity and within the injured hemisphere of the brain. Samples were assumed to be symmetric about the cerebral fissure, and regions B and D were located contralateral to regions A and C, respectively. Region E was positioned at approximately the center of the sample on the aqueduct. Coordinates were normalized to account for differences in the cross-sectional dimensions between samples due to intra-specimen variability. The normalization was performed by making length and width measurements on the cross-section of each sample; the five indentation coordinates were then multiplied by the ratio of the cross-sectional dimensions of the first sample tested under this protocol, ID NIB00287, to those of the sample of interest; the normalized coordinate locations were then dimensioned from region E using digital micrometers. Evan's Blue Dye was used to mark each coordinate on the tissue cross-section for a visual reference onto which the indenter could be positioned. The amount of dye under the indenter was assumed to have a negligible effect on the tissue properties. A total of 30 minutes were allotted for sample preparation, i.e. from the time of tissue collection to the time indentation testing began.

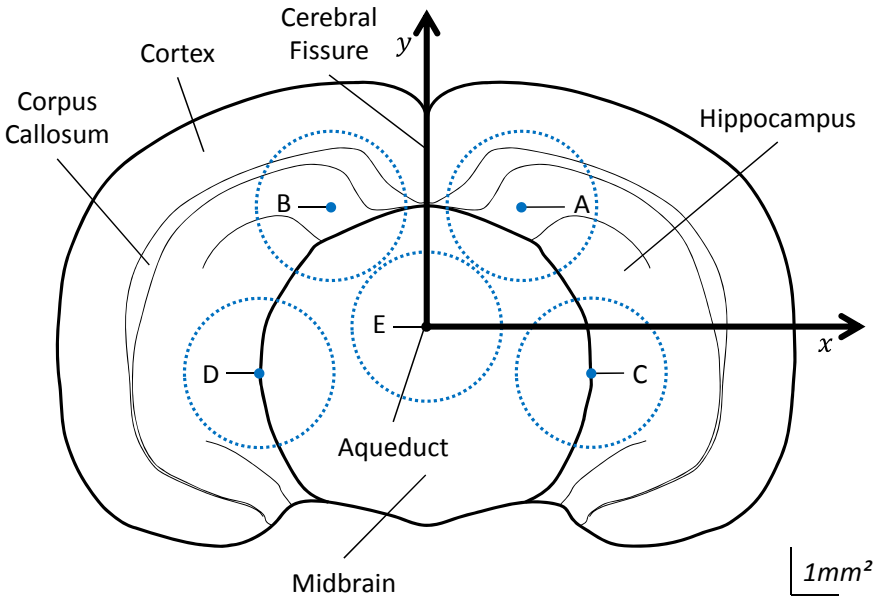

Figure 1: Schematic of a tissue sample showing the coordinate locations of the five un-normalized indentation regions (x, y): A = (2, 2.5), B = (-2, 2.5), C = (3.5, -1), D = (-3.5, -1) and E = (0, 0). Dashed circles represent the cross-sectional area of the indenter overlaid onto the tissue sample.

Indentation Testing

The aluminum test stage with sample was mounted atop a 50gram load cell (Model 31 Low, Honeywell International Inc., Golden Valley, MN), and beneath a 3.18mm diameter plane-ended cylindrical indenter mounted to a linear actuator equipped with an LVDT to measure displacement (ElectroForce® 3100 Test Instrument, Bose Corporation – ElectroForce Systems Group, Eden Prairie, MN). Excess compliance in the test frame due to the motion of the actuator induced an inertial based force response in the load cell. A 500g linear accelerometer (Model#: 7264B-500, Humanetics Innovative Solutions, Plymouth, MI) was mounted to the test stage to subtract off this effect. Force, displacement, and acceleration data were acquired at 20kHz (DEWE-

2010, Dewetron Inc., Wakefield, RI). Regions were tested in a randomized order for each experiment. At each coordinate the indenter was centered on the Evan's Blue Dye. This was accomplished by mounting a 1.3mm diameter spherical tip punch to the actuator and positing directly over the dye via visual inspection. The spherical punch was exchanged with the plane-ended cylindrical indenter, which was assumed to be centered over the indentation coordinate. The indenter was advanced slowly toward the tissue at a rate of 0.01mm/s until a tare load of 0.3gram was achieved. The indenter tip was then pressed 0.6mm into the tissue, normal with respect to the local surface, in approximately 8ms and then held for 30s to measure the tissue's relaxation. A peak displacement velocity of 120mm/s, at an approximate strain rate of $17s^{-1}$, was observed during the ramp portion of the displacement. After each test the indenter was carefully removed from the tissue. Five minutes were allotted between tests to allow for tissue recovery and instrumentation adjustments [26]. The tissue was sprayed with Millonig's in between each indentation test. The protocol was repeated for the remaining four regions and all testing was completed within 75 minutes of animal sacrifice.

Mathematical Modeling

All data were filtered in accordance to the SAE-J211 standard, CFC 1000, using a zero-phase, digital IIR 8 pole butterworth filter at a Low Pass frequency of 1650Hz. The data were resampled in a logarithmically scaled time step to give equal weights to both ramp and hold portions of the test. Samples were assumed to be incompressible and isotropic [9], [10]. The force response, $F(h,t)$, to the displacement input, $h = h(t)$, was modeled using a quasi-linear viscoelastic (QLV) mathematical framework [27]:

$$F(h,t) = \int_0^t G(t-t')\frac{\partial F^e(h)}{\partial h}\frac{\partial h}{\partial t'}dt' \tag{1}$$

where $F^e(h)$ is the instantaneous elastic response, $G(t)$ is the reduced relaxation function, t is the time, and t' is a dummy variable over which the convolution integral (1) is evaluated. The instantaneous elastic response was modeled using the solution to the Boussinesq problem for a flat-ended cylindrical punch [28]:

$$F^e(h) = \frac{4R\kappa\mu}{1-\nu}h \tag{2}$$

where R is the radius of the indenter, ν is Poisson's ratio, which was assumed to be 0.5, μ is the shear modulus, and κ is a constant used to incorporate the effect of substrate on finite sample thickness [29]. Values of κ were obtained for each sample and found to be between 1.26 and 1.3. The shear modulus was chosen to be a second-order, even function of h to capture the spatial nonlinearity of the tissue [23]:

$$\mu = \mu(h) = \mu_0 + \mu_2 h^2 \tag{3}$$

where μ_0 and μ_2 are the *instantaneous linear* and *nonlinear shear modulus coefficients*, respectively. Using this form for the shear modulus results in

$$F^e(h) = F_1 h + F_3 h^3 \tag{4}$$

where F_1 and F_3 are the *linear* and *nonlinear coefficients* of $F^e(h)$, respectively, described in (2). The mathematical solutions for the values of μ_0 and μ_2 in terms of F_1 and F_3 are determined through the use of equations (2-4).

$$\mu_0 = \frac{1-\nu}{4R\kappa}F_1 \qquad\qquad \mu_2 = \frac{1-\nu}{4R\kappa}F_3 \tag{5}$$

A six term prony series with five time constants was chosen to model the relaxation behavior of the tissue:

$$G(t) = G_\infty + \sum_{i=1}^{5} G_i \cdot e^{-\frac{t}{\tau_i}} \qquad \text{under the constraint that} \qquad G_\infty + \sum_{i=1}^{5} G_i = 1 \tag{6}$$

where G_i's are the normalized relaxation coefficients of the corresponding time decades and G_∞ is the coefficient of the steady-state response. Values for the thirteen coefficients F_1, F_3, τ_i, G_i, for i=1 to 5 and G_∞ were determined through a reduced gradient algorithm (Excel Solver®, Microsoft®, Redmond, WA) that was used to minimize the sum squared error between the model-predicted force, resulting from numerical integration of (1), and the experimental data. An individual set of optimal coefficients was determined for each indentation test. Preliminary analysis of the model fit to the first few data sets; test ID NIB00288A through NIB00288E, indicated marginal variability in the values for the optimized time constants, τ_1≈0.001s, τ_2≈0.01s, τ_3≈0.1s, τ_4≈1s, τ_5≈10s. To simplify the model the time constants were fixed at theses decades for the remainder of the analysis and only eight parameters needed to be optimized through model fitting.

Statistics

The number of terms, i, in equation (6) were determined via an F-test [30]. Data from test ID NIB00318E was modeled with four, five, and six time constants to see if there was a statistically significant improvement in the model's fit to the data. The model with five time constants gave a significantly better fit (F≈9, p < 0.001) than the model with four time constants and the model with six time constants showed no improvement in fit over five time constants (F≈0, p≈1). Therefore the model with five time constants was chosen for the analysis. The critical F-statistic at the α=0.05 level of significance for both tests was F_c ≈1. A total of n=8 indentation tests were performed per region, A-E, and per injury treatment, Sham and severe injury, for a total of 10 groups. For each group, an average $F^e(h)$ and $G(t)$ were determined using least squares optimization between the average and the eight individual measurements. The coefficients of the shear modulus, μ_0 and μ_2 were calculated from F_1 and F_3 of the eight individual curves using expression (5). An average μ_0 and μ_2 were then determined for each group. Additionally, the coefficients of $F^e(h)$ and $G(t)$ at regions A and C were normalized to the values at the contralateral regions B and D, respectively. Specifically, normalization was performed by dividing the value of a particular absolute coefficient F_1, F_3, μ_0 and μ_2 at region A by its corresponding absolute contralateral value at region B. For example, F_1 from indentation test ID NIB00290A was divided by F_1 from indentation test ID NIB00290B, etc. The process was repeated for the coefficients at region C, dividing by the corresponding contralateral values at region D. The absolute structural and material properties (F_1, F_3, μ_0, μ_2, G_i, for i=1..5 and G_∞) were compared separately to evaluate for the effect of region and injury treatment using a two-way ANOVA. *Post-hoc* comparisons were made using a student's t-test with the appropriate Bonferroni correction. Samples were assumed to be independent measurements of a particular tissue property, normally distributed and homoscedastic. To evaluate the differences observed in the normalized ratios, student's t-tests with a Bonferroni correction were used to make comparisons across injury treatment at a particular region. Specifically, a direct comparison was made between the normalized ratios of Sham and severely injured tissue at region A to evaluate the effect of injury at the location of the contusion cavity.

III. RESULTS

Eighty indentation tests were performed on the tissue samples, and data from 16 of the original 20 animals were used in analysis. The tissue from animal ID NIB00311 was damaged upon collection and the data from 3 additional experiments were compromised due to either unpreventable noise from the surroundings (animal ID NIB00287), or experimental error (animal IDs NIB00295 and NIB00298). Average $F^e(h)$ and $G(t)$ for region and injury treatment are shown in Figure 2. Region specific, *absolute* structural and material properties, *normalized* ratios, and results of the t-tests are reported in Table 1 (see appendix). ANOVA indicated significant (p < 0.05) main effects of both region and injury treatment on the absolute coefficients. On average, F_1 and μ_0 were higher (p < α=0.005) in region E compared to region A (F_1: +36.3mN/mm, p=0.002 and μ_0: +2.23kPa, p=0.002). The relaxation coefficient, G_1, was found to be higher while G_3 and G_∞ were lower (p < α=0.05) in severely injured samples compared to Sham controls (G_1: +0.011, p=0.0164, G_3: -0.003, p=0.008, and G_∞: -0.003, p=0.044). The student's t-test, revealed a significant decrease (p < α=0.025) in the value of the normalized ratios of F_3 and μ_2, (-26%, p=0.0084 each), in severely injured tissue compared to Sham controls. Conversely, the t-tests revealed a significant increase in the normalized ratios of F_3 and μ_2, (+38%, p=0.0156 each) on severely injured compared to sham controls in region C. The percentages reported here are calculated as percent differences in the sample means from Sham samples.

(Region A)

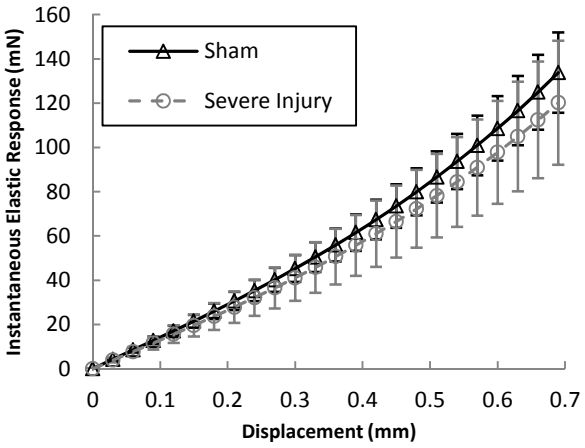

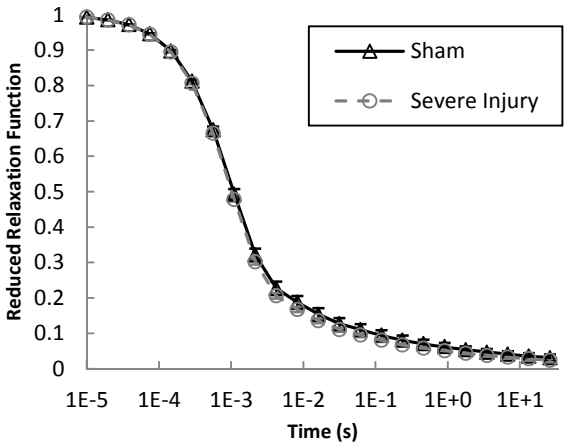

(Region B)

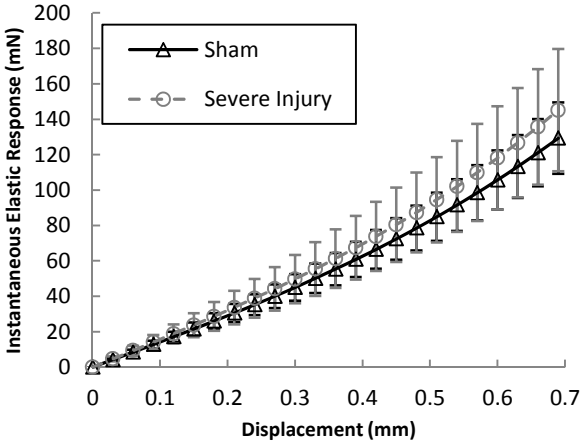

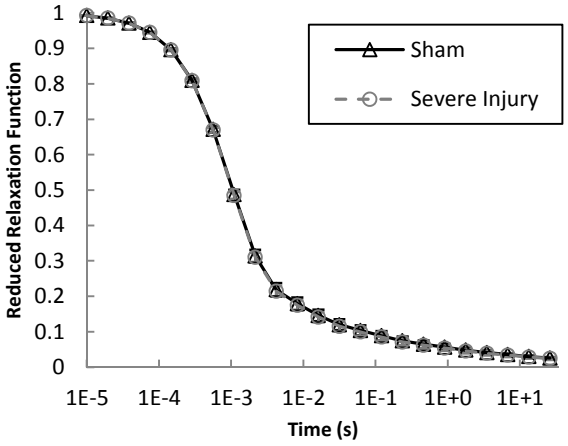

(Region C)

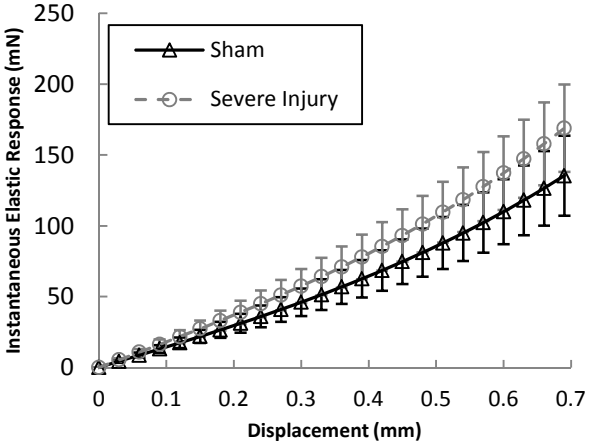

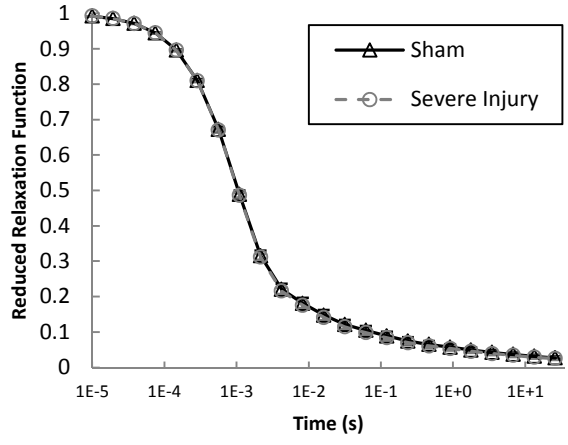

(Region D)

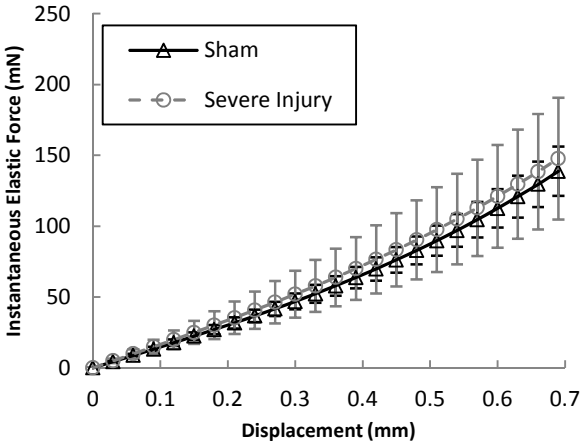

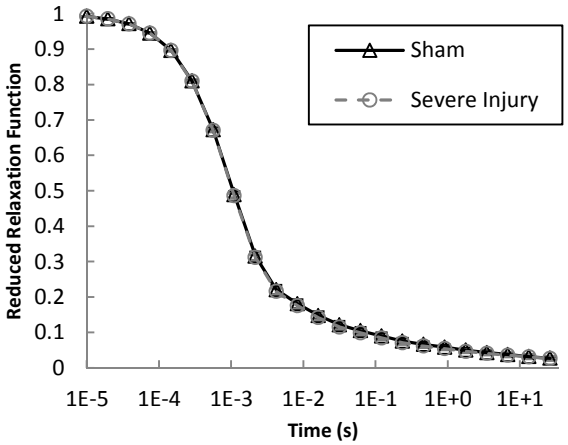

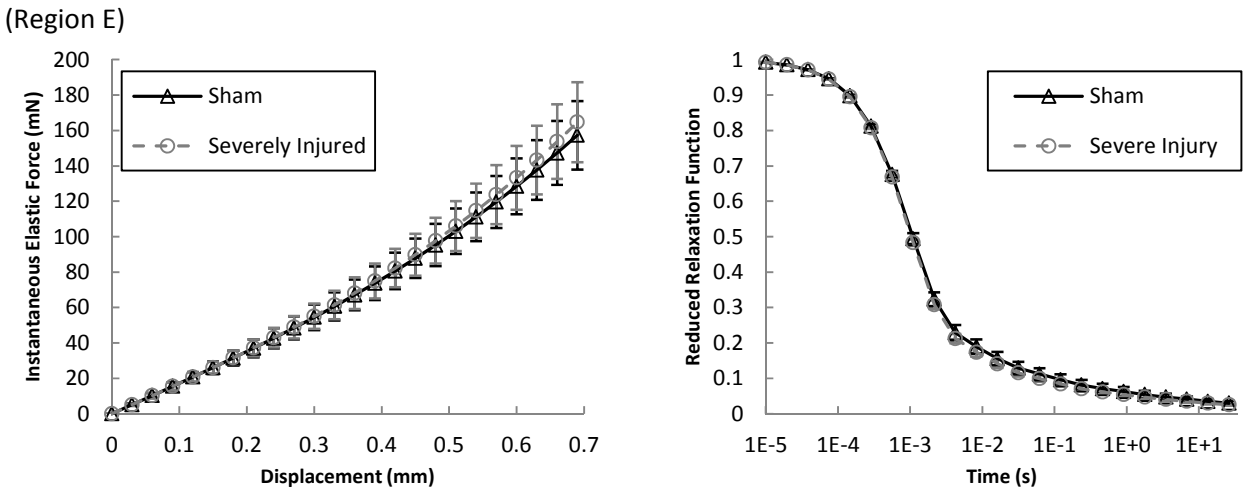

Figure 2: Average $F^e(h)$ and $G(t)$ for region and injury treatment. Error bars are 95% Confidence Intervals. Average $F^e(h)$ curves for severe injury were on average stiffer than the average Sham curves in all regions except for region A. The reduced relaxation functions were nearly identical in all cases.

IV. DISCUSSION

This study found the mechanical properties of the rat brain to be viscoelastic, spatially nonlinear, and dependent on both region and injury treatment. A linear viscoelastic model was fit to the experimental data, in addition to the QLV model, where equation (3) was assumed to be a function of μ_0 only. With the same number of prony series terms, the fits of both the linear and QLV models were visually assessed using tissue force time histories, and compared statistically using the F-test, Figure 3. The linear model fit the data well during the first of half of the ramp and long term relaxation of the tissue; however, the addition of the nonlinear term through QLV showed a statistically significant improvement in the model fit ($p < 0.001$) to the experimental data, capturing the entire ramp, peak force, and initial tissue relaxation, Figure 3a. To justify the use of QLV over a fully nonlinear viscoelastic model the ratio of the relaxation forces from two different displacement steps were calculated and then checked to be approximately constant in time using linear regression. Two displacement steps, the first to 0.6mm and the second to 1.2mm, were applied to tissue from a severely injured animal; ID NIB00291 at region A and region E. Results from the linear regression were used to evaluate whether or not the slope of the force ratio was statistically significant from zero. Data up to 100ms after the peak force were not included in the analysis due to transience of the displacement ramp. The value of the regression coefficient, the slope, was found to be statistically significant (slope = $0.035s^{-1}$, $p < 0.001$) at region A and (slope = $0.007s^{-1}$, $p < 0.001$) at region E. However, the magnitude of the slope was not thought to be meaningful. That is, the ability to detect small changes in the value of the slope was due to the large amount of data being used, and that the resulting values were not influential, suggesting a relatively constant response over time. These results indicated that the relaxation behavior of the tissue was independent of displacement and that no temporal nonlinearities were observed up to approximately 18% sample penetration.

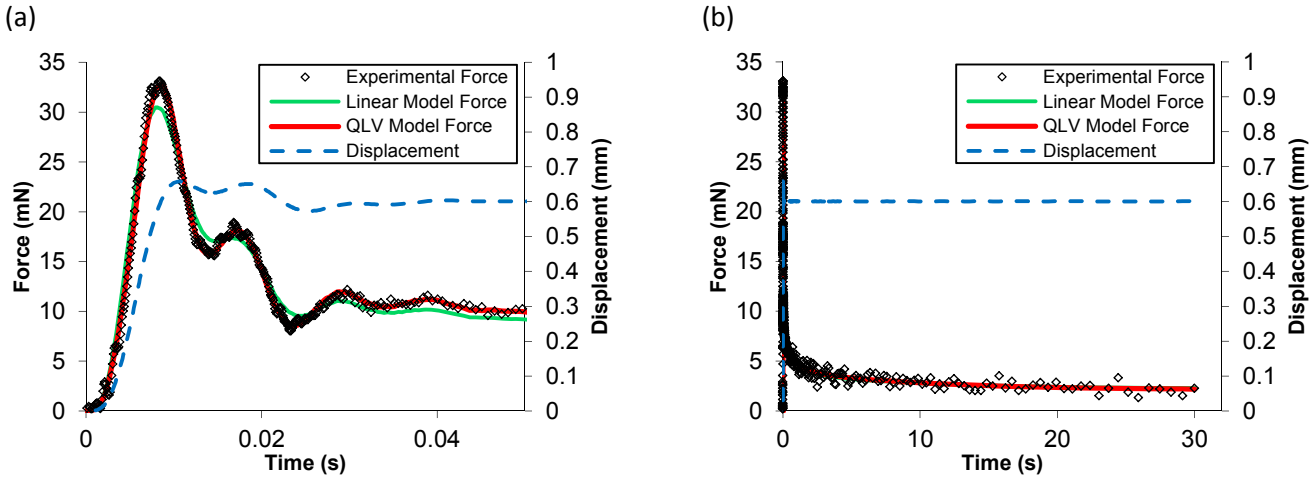

Figure 3: Examples of the QLV model fit to the experimental data for both the ramp (a) and hold (b) portions of an arbitrarily chosen indentation test (NIB00308B). The QLV model followed the experimental data more closely than the linear model during the ramp, peak, and initial relaxation of the tissue (a). Both models followed the data closely during the hold portion of the test (b). A similar result was observed when modeling other experimental data. The increase in force near 16ms and 30ms is due to the increase in displacement of the indenter into the tissue at these times.

Validation of the test methodology selected for the current study involves a comparison to other brain studies reported in the literature. The absolute mechanical properties and uncertainties found in the current study are consistent with those determined experimentally for shear [9], [31], compression [32] and indentation [23]. Further, the data fit within the reported range of shear moduli for brain tissue (0.1-22) kPa [8]-[16], [23] and [32]-[34]. Darvish and Crandall characterized bovine brain using QLV under oscillatory shear tests up to 200Hz and 20% Lagrangian strain [9]. They observed 16kPa and 2.62kPa for the linear and nonlinear instantaneous elastic shear moduli, respectively. On the other hand, Takhounts et al. tested both bovine and human brain up to 100% Lagrangian shear strain in ramp and hold tests and determined the instantaneous linear shear moduli to be approximately 2kPa and 1.5kPa, respectively [10]. Shuck and Advani found large variability in the shear modulus [31]. They performed oscillatory torsion tests on human brain up to 60Hz and observed (3-16)kPa. In each of these studies the brain was modeled under the assumptions of isotropy and incompressibility.

In regards to the results reported for indentation studies, Gefen et al. tested both young and mature rats in vivo and in situ under spherical indentation, and determined values for the instantaneous shear modulus between (1.2-3.3)kPa [15]. Further, Gefen and Margulies [33] compared the effects of in vitro, to in vivo and in situ on the material properties of porcine brain. They used a hemispherical indenter and found the short term shear modulus between (0.7-2.8)kPa. In both studies preconditioning was found to significantly reduce the value of the shear modulus and in vitro results tended to be lower than in vivo and in situ. Samples were not preconditioned in the current study as work by Shafieian et al. [23] suggests preconditioning may have damaged their samples and reduced the effect of injury. Various other studies have used micro-indentation to determine region specific material properties in rat brain [13], [34]. These studies observed values for the short term shear modulus on the order of (0.1-1.5)kPa, nearly one order of magnitude lower than the values reported in the current study. The material properties of brain have shown to be rate sensitive and increase with increasing strain rate or frequency [9] [10]. The load rates reported in these studies were less than 1mm/s, (0.4-0.5)s^{-1}, and much less than that of the current study which could explain this discrepancy. Additionally, these studies performed indentation tests up to depths of 40μm on the surface of tissue cross sections that had previously been blocked and then mechanically cut using a vibratome. Consequently, their findings may have been significantly altered from that of normal, healthy tissue. The tissue samples tested in the current study were hand cut and tested in vitro. As a result of sample preparation, a thin layer on the surface of the tissue likely sustained damage. Even though the indentation depths used in the current study were much higher than those used in micro-indentation, it is reasonable to expect some alterations in the mechanical properties from that of normal, healthy, living tissue.

In a similar study to the current, Shafieian et al. performed cylindrical indentation at two locations, PDx and PmJ, on the brainstem of impacted rats and found a statistically significant reduction in $F^e(h)$ between uninjured and injured specimens [23]. They reported values for μ_0 and μ_2 between (1-10)kPa and (1-25)kPa/mm^2, respectively with similar uncertainties to that of the current study. The reported reduction in μ_0 between injured specimens and Sham controls was 35%. This value was an average taken from both preconditioned and un-preconditioned samples and found to be in agreement with the work of Darvish and Crandall [12] who reported a 33% reduction in the linear shear modulus after non-recoverable strain conditioning. However, Shafieian et al. did not specify the significance of change in μ_0 and μ_2 with respect to injury treatment, making it unclear which parameter, if any, was driving the reduction in shear modulus after tissue damage [23]. On average, they saw a 28% and 47% reduction in μ_0 and μ_2, respectively, for un-preconditioned samples at PDx. Further, they observed a 14% and 29% reduction in μ_0 and μ_2 for un-preconditioned samples at PmJ; however, this result was not statistically significant. In the current study μ_0 and μ_2 were reduced on average 17% and 26%, respectively at the location of the contusion cavity, region A. This was observed after normalizing the data and the reduction in μ_0 was not statistically significant. In the case of

the absolute material properties, the observed differences in μ_0 and μ_2 between severely injured and Sham samples were not significant. Additionally, the reported 38% increase in μ_2 at region C on severely injured compared to sham tissue contradicts the findings for the normalized properties at region A. Further investigation into this matter is needed; however there was no evidence of mechanical damage in this region when compared to the visible damage of the contusion cavity in region A.

Possible reasons for these discrepancies can be attributed to a number of factors. In the current study, a CCI model was used to deliver injury directly to the cortex [35]. On the other hand, Shafieian et al. chose an impact acceleration model to generate DAI in the brainstem due to its predictable pattern of injury there [23], [36]. Further, regions tested in the current study incorporate both white and grey matter and are heterogeneous compared to the brainstem which is comprised of predominantly white matter and is relatively homogenous and stiffer than the cortex [37]. Another explanation for these discrepancies is the rate at which the tissue samples were loaded under indentation. Peak Loading rates determined from the tests conducted by Shafieian et al. [23] were between (16-33)mm/s, (8-16)s^{-1}, while that of the current study was approximately 120mm/s, 17s^{-1}. High rate inputs are necessary to characterize the mechanical response of the brain during TBI [38]. The peak loading rates reported in the current study are within the range of those reported for impact traumas [13], [38], and [39]. An understanding of the brain's mechanical response at high load rates would be useful for computational models of these events. However, testing at these rates may cause further damage to the tissue and reduce the effect of injury on the mechanical properties. Strain and strain rate tissue tolerance thresholds have previously been studied and the reported values associated with axonal injury are between 0.1-0.2 Lagrangian strain with strain rates greater than 10s^{-1} [9], [19]-[22].

The hypothesis that the tissue samples were damaged upon loading was examined in a separate analysis. A QLV model with only 1 time constant τ_1= 0.001s was fit to the ramp portion the experimental data (n=16) for region A. The form of $F^e(h)$ was kept the same as expression (4). The model was fit in three ways. The sum squared error was minimized between the model and experimental forces from: (1) the toe region to the force corresponding to the peak loading rate; (2) the force corresponding to the peak loading rate up to the peak force; and (3) over the entire ramp from the toe region to the peak force. Average $\mu_0$and μ_2 were determined from the (n=16) individual fits. ANOVA revealed significant ($p < 0.05$) differences between the three model fits. Post-hoc Bonferroni comparisons were made between individual samples and revealed the following information. The value of μ_0 was approximately constant across all three models, while the value of μ_2 decreased by 34% ($p < 0.001$) after the peak displacement rate of 120mm/s. This observation was made independent of injury treatment. The stability of the model was evaluated during each of the three fits due to the relatively small amount of data being fitted. Regardless of initial inputs, model parameters optimized to the same values, indicating a stable solution. These results suggest that the tissue may have been damaged during loading up to 5% tissue penetration and at a peak rate of 17s^{-1}.

V. CONCLUSIONS

This study presents an experimental methodology and analytical framework for modeling the region specific structural and material properties of mechanically injured and uninjured brain tissue. Force data were acquired under high rate loading inputs in the range of those related to impact traumas. Quasi-linear viscoelasticity, a popular, constitutive model that is commonly used to model soft biological materials was chosen to fit the experimental data over both linear and fully nonlinear viscoelastic models. The tissue was assumed to be isotropic and incompressible for model simplification. The mechanical properties were found to be viscoelastic, nonlinear, and regionally dependent. Additionally, these properties were quantified under a well characterized injury model capable of delivering repeatable levels of mechanical damage directly to the dura. To the authors' knowledge, this is the first study to examine the mechanical properties of the brain after CCI. The results for the shear modulus were within the range reported in the literature for shear, compression, and indentation tests. The material and structural properties were found to be roughly constant across region and injury treatment. However, after normalizing the region specific mechanical properties in regions A and C, there were statistically significant differences in the values of the nonlinear coefficients of the instantaneous shear and elastic response. A 26% reduction in the nonlinear material and structural coefficients were observed in severely injured samples compared to healthy controls at the location of the contusion cavity. The utility of this research is crucial for understanding the mechanical response of the brain after TBI. Knowledge of such

material properties may be useful to uniquely identify different types of brain injury and to better understand the mechanics of repetitive brain injuries.

VI. LIMITATIONS

There are a number of limitations that may influence overall response of the tissue samples during mechanical loading. First, the solution to the Boussinesq problem assumes indentation of a semi-infinite elastic half-space. The samples used in the current study have finite boundaries and exhibit damping as well as elastic properties. This solution was modified by [29] to incorporate the effect of a rigid substrate on finite sample thickness. The corrective factor κ was developed for indentation on articular cartilage and subsequently applied to indentation tests performed on other soft biological tissues including brain [13], [23]. The factor κ functions to reduce the applied load, measured within the tissue, by an amount that depends on the ratio of the indenter radius to sample height. As the indenter radius increases or sample height decreases, higher forces are transmitted from the substrate to the tissue. To avoid the effect of substrate on mechanical properties, a common rule of thumb is to limit indenter penetration to depths of no greater than 10% of the total sample thickness [40]. Penetration depths in the current study obey this rule. However, more recent work has observed noticeable substrate effects within 10% penetration and claim that the ratio of the indenter radius to sample height must be kept within 10% [41]. The ratio of radius to sample height is 20% in the current study and κ was implemented to adjust for this limitation. In addition to substrate effects, other boundary conditions have been violated. In all regions except E, the distance between the indenter and edge of the tissue sample was less than the recommended distance of one indenter's width. This would have the effect of reducing the material properties observed in regions A-D compared to E. Indenter interference is an additional concern in this study. The process by which the coordinates were dimensioned on the surface of the tissue was imperfect. Slight offsets in the dimensioning may have led to overlapping indentation tests. Further, the indentations made on the surface of the samples were within one diameter of each other. However, adequate time was allotted for tissue recovery in between subsequent tests. Finally, contusion cavities can be problematic for material studies [23]. They are often near the edge of the sample and create discontinuities in the tissue surface making it difficult to obey boundary conditions under most mechanical tests. It is suggested that future studies involving contusion cavities be made in vivo or situ with the brain left in the skull.

A number of studies including the current have used the F-test to statistically determine an appropriate model for fitting experimental brain data [13], [23], [34]; however, there are limitations. The F-test assumes the data to be independently measured and normally distributed. In addition, there must be a linear relationship between independent and dependent variables in the models chosen to fit the data. The force data in the current study are not normally distributed and not independent measurements in time. Further, in both the linear viscoelastic and QLV models the relationship between force and time is not linear. Therefore it is not clear that hypothesis testing using the F-test is suitable or meaningful to determine the most appropriate model. In this case, visual inspection of the model fit to the data may provide a better indicator of goodness of fit.

VII. ACKNOWLEDGEMENT

This work was performed at the University of Virginia, and in collaboration with the University of Washington. Funded in part by the Defense Medical Research and Development Program (DMRDP), award No. DM090796.

VIII. REFERENCES

[1] Faul M, Xu L, Wald MM, Coronado VG, "Traumatic brain injury in the United States: emergency department visits, hospitalizations, and deaths, Atlanta (GA): Centers for Disease Control and Prevention, National Center for Injury Prevention and Control, 2010", Internet: [http://www.cdc.gov/traumaticbraininjury/tbi_ed.html], January 7, 2013, [February 21, 2013]

[2] Owens BD, Kragh JF Jr, Wenke JC, Macaitis J, Wade CE, Holcomb JB, Combat wounds in Operation Iraqi Freedom and Operation Enduring Freedom, *Journal of Trauma-Injury Infection & Critical Care*, 64(2):295-299, 2008.

[3] Pascrell B Jr, Congressman, Introduction to the report of the international conference on behavioral health and traumatic brain injury, *The Clinical Neuropsychologist*, 23(8):1281-1290, 2009.

[4] Farkas O, Povlishock JT, Cellular and subcellular change evoked by diffuse traumatic brain injury: a complex web of change extending far beyond focal damage, *Progress in Brain Research* 161:43-58, 2007.
[5] McAllister TW, Neurobiological consequences of traumatic brain injury*, Dialogues in Clinical Neuroscience*, 13(3):287-300, 2011.
[6] Povlishock JT, Katz DI, Update of neuropathology and neurological recovery after traumatic brain injury, *The Journal of Head Trauma Rehabilitation* 20(1):76-94, 2005.
[7] Holbourn AHS, Mechanics of head injury, *The Lancet*, 2, 6267, 438-441, 1943.
[8] Galford JE, McElhaney JH, A viscoelastic study of scalp, brain, and dura, *Journal of Biomechanics*, 3(2):211-221, 1970.
[9] Darvish K, Crandall JR, Nonlinear viscoelastic effects in oscillatory shear deformation of brain tissue, *Medical Engineering & Physics*, 23:633-645, 2001.
[10] Takhounts EG, Crandall JR, Darvish KK, On the importance of nonlinearity of brain tissue under large deformations, *Stapp Car Crash Journal*, 47:79-92, 2003.
[11] Gefen A et al., Age-dependent changes in the material properties of the brain and braincase of the rat, *Journal of Neurotrauma*, 20(11):1163-1177, 2003.
[12] Prange MT, Margulies SS, Regional, directional, and age-dependent properties of the brain undergoing large deformation, *Journal of Biomechanical Engineering*, 124:244-252, 2002.
[13] Finan JD, Pearson EM, Morrison III B, Viscoelastic properties of the rat brain in the horizontal plane, *Proceedings of IRCOBI Conference*, Dublin, Ireland, pp. 474-485, 2012.
[14] Thibault KL, Margulies SS, Age-dependent material properties of the porcine cerebrum: effect on pediatric inertial head injury criteria, *Journal of Biomechanics* 31(12):1119-1126, 1998.
[15] McElhaney JH, Roberts VL, Hilyard JF, Handbook of Human Tolerance, Japan Automobile Research Institute, Incorporated (JARI), p. 143, 1976.
[16] Arbogast KB et al., A high-frequency shear device for testing soft biological tissues, *Journal of Biomechanics,* 30(7):757-759, 1997.
[17] Dobbing J, The later development of the brain and its vulnerability. In: Davis J A, Dobbing J (Eds.), Scientific Foundations of Paediatrics, *Heinemann Medical*, London, UK, 1974.
[18] Mao H, Jin X, Zhang L, Yang KH, Igarashi T, Noble-Haeusslein LJ, et al., Finite element analysis of controlled cortical impact-induced cell loss, *Journal of Neurotrauma*, 27(5):877-88, 2010.
[19] Elkin BS, Morrison B III, Region-specific tolerance criteria for the living brain, *Stapp Car Crash Journal,* 51: 127-138, 2007.
[20] Cater HL, Sundstrom LE, and Morrison B, Temporal development of hippocampal cell death is dependent on tissue strain but not strain rate, *Journal of Biomechanics* 39(15):2810-2818, 2006.
[21] Morrison III B, Cater HL, Wang CC, Thomas FC, Hung CT, Ateshian GA, et al., A tissue level tolerance criterion for living brain developed with an in vitro model of traumatic mechanical loading, *Stapp Car Crash Journal*, 47:93-105, 2003.
[22] Bain AC, Meaney DF, Tissue-level thresholds for axonal damage in an experimental model of central nervous system white matter injury, *Journal of Biomechanical Engineering,* 122:615-622, 2000.
[23] Shafieian M, Darvish KK, and Stone JR, Changes to the viscoelastic properties of brain tissue after traumatic axonal injury, *Journal of Biomechanics,* 42(13):2136-2142, 2009.
[24] Saxena T, et al., Mechanical characterization of the injured spinal cord after lateral spinal hemisection injury in the rat, *Journal of Neurotrauma*, 29(9):1747-1757, 2012.
[25] Paxinos G, Watson C, The Rat Brain in Stereotaxic Coordinates 5th Edition, Bregma -5.04 mm, *Elsevier*, Oxford, UK, 2005.
[26] Hrapko M et al., The mechanical behavior of the brain tissue: Large strain response and constitutive modeling, Biorheology, 43:623-636, 2006.
[27] Fung YC, Biomechanics: Mechanical Properties of Living Tissues, 277-280, *Springer*, New York, NY, 1993.
[28] Sneddon IN, The relation between load and penetration in the axisymmetric Boussinesq problem for a punch of arbitrary profile, *International Journal of Engineering Science* 3(1):47-57, 1965.
[29] Hayes WC, Keer LM, Herrmann G, and Mockros LF, A mathematical analysis for indentation tests of articular cartilage, *Journal of Biomechanics*, 5(5):541-551, 1972.

[30]Motulsky HJ, Cristopoulos A, Fitting Models to Biological Data using Linear and Nonlinear Regression. A Practical Guide to Curve Fitting. 2003, GraphPad Software Inc., San Diego CA, www.graphpad.com.
[31]Shuck LZ, and Advani SH, Rheological response of human brain tissue in shear, *Journal of Basic Engineering*, 94 (D), 905-911, 1972.
[32]Estes MS and McElhaney JH, Response of the brain tissue of compressive loading. ASME, No 70-BHF-13, 1970.
[33]Gefen A, Margulies SS, Are in vivo and in situ brain tissues mechanically similar? *Journal of Biomechanics*, 37:1339-1352, 2004.
[34]Elkin BS, Ilankovan A, and Morrison III B, A detailed viscoelastic characterization of the rat brain*, Journal of Neurotrauma* 28:2235-2244, 2011.
[35]Lighthall JW, Controlled cortical impact: a new experimental brain injury model, *Journal of Neurotruama*, 5(1):1-15, 1988.
[36]Marmarou A et al., A new model of diffuse brain injury in rats, *Journal of Neurosurgery* 80:291-300, 1994.
[37]Arbogast K, Margulies S, Material characterization of the brainstem from oscillatory shear tests, *Journal of Biomechanics* 31(9):801–807, 1998.
[38]Mertz HJ, Anthropomorphic test devices, In: Nahum, A.M., Melvin, J.W. (Eds.), Accidental Injuries. *Springer,* New York, pp. 72–88, 2002.
[39]Hardy WN et al., A study of the response of the human cadaver head to impact, *Stapp Car Crash Journal* 51:17, 2007.
[40]Bückle H, Progress in micro-indentation hardness testing, *Metallurgical Reviews*, 4(1):49-100, 1959.
[41]Wang M et al., Nanoindentation of polymeric thin films with an interfacial force microscope, *Journal of the Mechanics and Physics of Solids*, 52:2329-2354, 2004.

IX. APPENDIX

Table 1: Absolute Structural and Material Coefficients of $F^e(h)$, $G(t)$, and $\mu(h)$ and Normalized Ratios for Region and Injury Treatment.

Absolute		A		B		C	
Unit	Coef.	Sham	Severe Injury	Sham	Severe Injury	Sham	Severe Injury
mN/mm	F_1	140.8 ± 19.2	128.2 ± 33.0	141.1 ± 24.1	155.2 ± 44.7	143.4 ± 30.7	179.0 ± 38.7
mN/mm³	F_3	111.6 ± 24.1	96.6 ± 19.7	97.3 ± 17.4	115.6 ± 22.3	110.8 ± 23.6	138.1 ± 16.4
kPa	μ_o	8.66 ± 1.23	7.89 ± 2.04	8.68 ± 1.51	9.55 ± 2.76	8.85 ± 2.00	11.02 ± 2.40
kPa/mm²	μ_2	6.88 ± 1.57	5.95 ± 1.23	5.99 ± 1.12	7.11 ± 1.38	6.83 ± 1.53	8.50 ± 1.03
-	G_1	0.739 ± 0.021	0.763 ± 0.010	0.749 ± 0.021	0.752 ± 0.015	0.746 ± 0.018	0.750 ± 0.010
-	G_2	0.122 ± 0.007	0.117 ± 0.007	0.121 ± 0.006	0.123 ± 0.004	0.122 ± 0.006	0.126 ± 0.004
-	G_3	0.057 ± 0.005	0.053 ± 0.004	0.055 ± 0.002	0.053 ± 0.006	0.057 ± 0.003	0.054 ± 0.003
-	G_4	0.029 ± 0.005	0.026 ± 0.002	0.029 ± 0.008	0.028 ± 0.003	0.027 ± 0.005	0.027 ± 0.002
-	G_5	0.023 ± 0.007	0.020 ± 0.005	0.023 ± 0.008	0.022 ± 0.006	0.023 ± 0.004	0.021 ± 0.002
-	G_∞	0.029 ± 0.009	0.022 ± 0.005	0.024 ± 0.003	0.022 ± 0.003	0.025 ± 0.004	0.023 ± 0.004

Absolute		D		E	
Unit	Coef.	Sham	Severe Injury	Sham	Severe Injury
mN/mm	F_1	145.7 ± 18.4	163.6 ± 54.1	170.8 ± 24.0	170.7 ± 21.8
mN/mm³	F_3	116.2 ± 33.5	106.0 ± 20.6	120.2 ± 32.3	142.8 ± 24.5
kPa	μ_o	8.96 ± 1.15	10.07 ± 3.35	10.49 ± 1.42	10.51 ± 1.39
kPa/mm²	μ_2	7.17 ± 2.15	6.52 ± 1.28	7.42 ± 2.07	8.79 ± 1.54
-	G_1	0.746 ± 0.015	0.750 ± 0.009	0.737 ± 0.024	0.756 ± 0.015
-	G_2	0.122 ± 0.006	0.125 ± 0.003	0.122 ± 0.007	0.118 ± 0.004
-	G_3	0.055 ± 0.004	0.054 ± 0.003	0.059 ± 0.004	0.056 ± 0.004
-	G_4	0.028 ± 0.004	0.026 ± 0.002	0.029 ± 0.005	0.024 ± 0.004
-	G_5	0.024 ± 0.007	0.020 ± 0.004	0.025 ± 0.010	0.023 ± 0.005
-	G_∞	0.025 ± 0.005	0.025 ± 0.006	0.028 ± 0.006	0.024 ± 0.002

Normalized Ratios		A			C		
Unit	Coef.	Sham		Severe Injury	Sham		Severe Injury
-	F_1	1.017 ± 0.144		0.843 ± 0.145	0.999 ± 0.228		1.187 ± 0.357
-	F_3	1.149 ± 0.182	*	0.848 ± 0.144	0.992 ± 0.158	†	1.361 ± 0.275
-	μ_o	1.017 ± 0.144		0.843 ± 0.145	0.999 ± 0.228		1.188 ± 0.357
-	μ_2	1.149 ± 0.182	**	0.848 ± 0.144	0.992 ± 0.158	††	1.362 ± 0.276

All symbols indicate a statistically significant result. Asterisks (*,**) and daggers (†,††) are comparisons between injury treatment at a particular region. (p = resulting p-value from a student's t-test and α = 0.025 is the Bonferroni corrected significance level). (*p = 0.0084, **p = 0.0085, †p = 0.0156, ††p = 0.0156. All uncertainties are ±95%CI.

Mourad PD (2013), "Therapeutic Ultrasound, with an emphasis on applications to the brain" in Nakamura K, Ueha S, eds. Ultrasonic transducers - materials design and applications**.** Woodhead Publishing Ltd.

Chapter title: Therapeutic Ultrasound with an emphasis on applications to the brain.

P. D. Mourad, University of Washington, USA

Abstract

Diagnostic and therapeutic ultrasound have their roots in early studies targeting applications to the brain dating back to the 1920s and 30s, with an early apogee in their activity due to the seminal work of the Fry brothers in the 1950s. Since then, there has been a quite significant resurgence over the last two decades in applications of diagnostic and therapeutic ultrasound to the central nervous system as technology has finally caught up with the visions of the founders of this field. Here in this book chapter I first give a review of how ultrasound interacts with tissue in general terms. Following that I'll touch upon diagnostic ultrasound in sufficient detail to highlight issues relevant to therapeutic applications of ultrasound. I'll close the diagnostic ultrasound portion of this chapter summarizing its application to imaging the peripheral nervous system and brain. I'll then turn to the topic of therapeutic ultrasound. I will start by covering basic concepts, most extensions or enhancements of concepts useful for diagnostic ultrasound. I'll close by summarizing several recent advances in the use of therapeutic levels of ultrasound closing with a review of very recent work, whose roots lie in again with the Fry brothers, on the topic of neuromodulation with ultrasound.

Key words.

Ultrasound, diagnostic ultrasound, therapeutic ultrasound, central nervous system, tumors, blood clots, drug delivery, neuromodulation.

Mourad PD (2013), "Therapeutic Ultrasound, with an emphasis on applications to the brain" in Nakamura K, Ueha S, eds. Ultrasonic transducers - materials design and applications**.** Woodhead Publishing Ltd.

1. Introduction and summary.

Here I review diagnostic and therapeutic ultrasound, discussing examples that target applications of ultrasound to the central and peripheral nervous systems. I make liberal use (paraphrases, quotes, concepts) from the existing general review literature on diagnostic and/or therapeutic ultrasound, for example, O'Brien (2007), Leighton (1994), ter Haar G and Coussios (2007), and Mourad (1999), among others. I will also directly cite specialized literature. Frankly, given the on-line resources these days, any interested reader can dig quite quickly through a number of dedicated websites and find relevant materials. My goal here, therefore, is to walk the reader through the concepts with a minimum of distractions rather than exhaustively review the literature. I will therefore cite a mix of classic papers and books, and recent review articles, primarily.

Here I first offer a general summary of ultrasound's interaction with tissue, starting with a description of its propagation, absorption, and scattering.

Important phenomena involved in acoustic propagation includes the fundamental non-linearity of this process, which produces down-stream effects from the ultrasound source that form the basis of a number of important diagnostic and therapeutic phenomena. In particular ultrasound absorbs as it propagates in proportion to the local intensity of ultrasound, intrinsic properties at the molecular level of the medium supporting the propagation, among other factors. Such absorption adds heat and momentum to the tissue. That heat increases the tissue's temperature; the associated strain pushes the tissue. Ultrasound will induce heat both as it propagates, and especially at its focus, of concern for diagnostic ultrasound, generally desired for therapeutic applications. If the tissue has low enough internal coherence, or is instead a

fluid, ultrasound's absorption will cause local flow known as "acoustic streaming." That heat and/or local strain can also cause "cavitation," that is the generation and/or stimulation of gas-filled voids within the material, described generically as bubbles, where stimulation causes the bubbles to grow and shrink and sometimes to break up or collapse. Cavitation can, in turn, produce local strains in the tissue and fluid that are close to the bubbles. (For example, local fluid flow around a bubble is called "acoustic microstreaming.")Oscillating bubbles generate more ultrasound focally, at the carrier frequency of the incident ultrasound as well as at higher frequencies. (Lower-period motions can also occur, at fractional subharmonics of the incident wave.) Monitoring of these acoustic emissions forms the basis for some novel imaging practices. Their production also tends to cause an increase in the energy absorbed from the incident sound field thereby producing more cavitation as well as more momentum and heat. Local cavitation generally also increases the subsequent scatter of ultrasound. The biological effects of ultrasound have their therapeutic effect in these thermal, mechanical, and chemical processes.

Typical applications of ultrasound for diagnostic purposes use short pulses (generally one to a few acoustic cycles) of intense (up to 5 MPa of instantaneous pressure, with instantaneous, spatially focal intensities of up to a few W/cm^2) ultrasound spaced fairly far apart in time (typically on the order of a millisecond) at frequencies (generally 1 to 10 MHz) high enough to resolve, via the generation and measurement of acoustic backscatter, fine-scale biological structure (with length scales of fractions of a millimeter and larger). The specific choices of these parameters balance the need to maximize the backscattered signal strength and imaging resolution, by increasing the

intensity and frequency of the sound, with the need to avoid harmful biological effects, achieved by decreasing the length and increasing the spacing of the pulses to help minimize the production of heat and mechanical forces within the imaged tissue.

With regard to diagnostic ultrasound, much research has been devoted to learning how to avoid altering tissue while using it, through what is known as study of ultrasound 'bioeffects'.

However, as in many things, a *desired* bioeffect can produce a desired therapeutic effect, and therapeutic ultrasound has as its guiding principle the study of their possible benefits, that is, its ability to treat disease with ultrasound, rather than to simply diagnose. Therapeutic ultrasound, especially for the brain, remains a research tool, one with significant promise that I will highlight here.

As summarized for diagnostic ultrasound, therapeutic ultrasound generates beneficial bioeffects by using a wider range of frequencies (0.02 to 10 MHz), focal pressures (1–50 MPa) and instantaneous, spatially focal intensities (10–10,000 W/cm^2) applied either in pulsed mode as compared with diagnostic ultrasound, often with greater pulse lengths and more pulses per second than in diagnostic ultrasound, or with "continuous waves," where there is no break in the application of ultrasound from the time it is first turned on until it is finally turned off.

To understand its promise for therapy, I'll first review the fundamentals of ultrasound's interaction with tissue then highlight its diagnostic usefulness before turning directly to its applications for therapy.

2. Fundamentals of Propagation and Absorption of Ultrasound

Almost all basic texts on ultrasound start by considering ultrasound waves as strictly and invariably periodic disturbances to the local density, pressure, location and velocity. Examples include Kinsler et al (1982) as well as Kremkau (1998).

When sound propagates in fluids it creates local, periodic perturbations in that fluid's density, pressure, and temperature as well as induces within the fluid small-scale displacements in the direction of wave propagation. When sound propagates in a simple solid, it generally does so both via "longitudinal" pressure waves, just described, and via "shear" waves, where the displacements and changes in pressure occur transverse to the direction of wave propagation. In the majority of biomedical applications the longitudinal waves dominate, and I restrict my discussion to this mode for this chapter. Am important exception is sonoelastic imaging, as I discuss below.

While sound propagation is always in principle a "nonlinear" process (e.g. Blackstock and Hamilton, 1997), that is, the qualities of the sound as it propagates vary as a complex function of its amplitude, in many practical applications the properties of the sound vary linearly with amplitude, so that doubling the amplitude of the ultrasound wave doubles the associated variations in pressure, density, displacement and particle velocity. Under those circumstances simple and useful formulae exist that relate the sound's frequency, amplitude, intensity, particle displacement, etc., assuming that the pressure wave varies sinusoidally in space and time (Again, Kinsler et al, 1982). However, those formulae and the sinusoidal concept on which they rest break down when the amplitude of the sound increases sufficiently and/or the wave propagates sufficiently far (Christopher and Carstensen, 1996). For example, in an unbounded

medium the initial "sine wave" form of the acoustic wave will evolve into a sharpened saw-tooth structure through the processes of diffraction, absorption, and focusing. A useful example comes from the field of lithotripsy (Sapozhnikov et al, 2007).There the application of high-intensity pulses of focused ultrasound breaks up calcified stones within the kidney and gallbladder, standard applications create a short acoustic wave train whose shape is far from sinusoidal, with peak positive pressures of up to 50 MPa that come and go within a few nanoseconds, and peak negative pressures of up to 1 MPa that last a few microseconds. One can represent these nonlinear waves via a Fourier series as a sum of sinusoids of increasing frequency relative to the frequency of the initial sinusoid. Within this description, one can say that that the acoustic wave becomes nonlinear via the generation of harmonics of the fundamental wave as the latter propagates and/or grows.

3. Acoustic Attenuation as Absorption Plus Scattering

As unfocused sound propagates through a medium, its amplitude decreases. It does so in part because the medium absorbs the sound and in part because the acoustic energy is scattered in a direction away from the propagation direction (Dunn et al, 1969). The relative amount of absorption versus attenuation in biological tissue depends significantly on the type of tissue. To appreciate why tissue attenuates sound, we start with quantifying how much sound tissue attenuates. The attenuation coefficient of ultrasound measures how much the amplitude of a propagating wave decreases as it propagates over a standard distance. For example, if a medium has an attenuation coefficient of 1 Np/cm (Np = Neper), this means that as the sound propagates 1 cm its

pressure amplitude has shrunk to 1/e of its original value. The book by Duck (Duck, 1990) organizes many fundamental constants describing ultrasound properties such as the attenuation coefficient, and is a required reference book for anyone working in ultrasound.

At 1 MHz the attenuation coefficient in water at room temperature is 0.00025 Np/cm, a negligible amount in the laboratory and significant only over kilometers in the ocean. In pure water, attenuation occurs through thermal relaxation of the water molecule, with a few additional molecular relaxation mechanisms that correspond to each of the typical chemicals in salt water. However, attenuation in biological tissue at 1 MHz is significantly higher, owing at least to increased absorption and also to increased scattering. For example, the attenuation coefficient for whole blood is 0.024 Np/cm while for plasma (whole blood minus red and white cells and platelets) it is 0.008 Np/cm. The different attenuation values for plasma and whole blood at the same frequency arise mostly because of scattering of the sound by the cells in whole blood, an attenuation mechanism missing from plasma. The different attenuation coefficients for plasma and water at the same frequency also arise because the individual proteins in the plasma absorb sound more efficiently than water, since proteins have many more degrees of freedom available than water molecules. However, although the levels of attenuation at 1 MHz differ as described, ultrasound attenuates more quickly in water as a function of increasing frequency than in biological tissue: attenuation increases as the square of the frequency in water but as only a little more than the first power of frequency in most tissue.(This means that the generation of higher and higher harmonics of a propagating ultrasound wave described above will eventually curtail due

to the increase in attenuation of the higher frequency waves.) At 1 MHz, liver has an attenuation coefficient of 0.08 Np/cm, larger than that of plasma, because liver has a greater concentration of proteins. Interestingly, pureed liver has a comparable attenuation coefficient to that of whole liver, thus showing that it is absorption on the molecular scale rather than at the scale of tissue structure that causes acoustic attenuation (Pauley and Schwan, 1971). The majority of papers on physical mechanisms of attenuation speak about multiscale springs within tissue responding in different, but coordinated ways as an ultrasound wave propagates through the tissue. (A particularly pleasing example of this is offered by Kelly and McGough (2009), who consider a fractal distribution of springs.)

Note, however, that scattering from discrete structures in tissue decreases the net transmission of ultrasound waves to a given point of interest, contributing to an effective increase in attenuation above the molecular mechanisms I have just discussed. Collagen is the common protein in biological tissue, and its concentration in tissue correlates well with acoustic attenuation due to absorption. For example, at 2.2 MHz and body temperature, white matter in the brain has an attenuation coefficient of 0.121 Np/cm, while gray matter has an attenuation coefficient of 0.072 Np/cm, and white matter absorbs more sound than gray matter. Finally, human lung tissue has an attenuation coefficient of 3.5 Np/cm at 1 MHz, owing almost entirely to the scattering of sound rather than to absorption, while bone at 1.0 MHz has an attenuation coefficient of 2.5 Np/cm, almost entirely owing to absorption rather than to scattering.

Absorption of sound in tissue can produce physical and chemical effects in biological media. These include the generation of heat, the addition of momentum, and

the production of bubbles, the latter known as "acoustic cavitation." I will now discuss these phenomena.

4. Physical and Chemical Processes Engendered by Medical Ultrasound

4.1 Heat Generation and Thermal Index

Sound absorbed by tissue generates heat at the site of absorption in a process described mathematically by the negative gradient of the energy flux vector of the sound field (Jain, 1983; ter Haar G and Coussios, 2007). When the acoustic waves are linear or weakly nonlinear, that heat-generation term reduces to a quantity proportional to the intensity of the signal and absorption (not attenuation) coefficient of the tissue, although for most applications the attenuation coefficient replaces the absorption coefficient, primarily because the attenuation coefficient is easier to measure than the absorption coefficient. The "bio-heat" equation describes the various processes that affect the translation of heat generated by ultrasound into increases in the temperature of tissue. It does so by codifying the net effect of tissue diffusion, heat capacity, and density along with the spatially integrated action of capillary beds, which can "perfuse" heat away from the acoustic source of heat as long as the tissue remains undamaged. Arteries or veins conduct heat away from a site also, and their presence within real and modeled tissue severely alters the temperature effects induced by ultrasound. Under therapeutic conditions, the temperature can approach 100°Cin a fraction of a second (ter Haar G and Coussios, 2007). This rapid temperature rise can denature tissue, useful for "cooking" cancer cells as a way to kill them, or even vaporize tissue, useful for ablation-based therapies for killing cancer, or for re-opening passages within the body, for

example. (We discuss these applications in the section on therapeutic ultrasound.) However, such effects are to be avoided when applying ultrasound diagnostically. The thermal index gives a measure of the temperature rise induced in tissue under diagnostic conditions (Kremkau, 1998). It is based on conservative estimates of the average heat generated within tissue and takes into account transducer characteristics that govern the intensity of sound at the site of acoustic heat generation as well as attenuation as the wave propagates through intervening tissue.

4.2 Acoustic Radiation Pressure

Sound absorbed by tissue and fluids not only adds heat but also adds momentum to those tissues and fluids via a force known as the "acoustic radiation force," created by the negative of the gradient of "radiation pressure" induced by acoustic waves (fun references include Rudenko et al, 1996; Sarvazyan, 2010). When an acoustic wave with constant properties (intensity, frequency well defined over a single pulse) deposits momentum in a substance away from boundaries, the sound effectively pushes the substance in a time-independent way in the direction of acoustic-wave propagation. In water, this process shows up as a steady current moving away from the transducer known as "acoustic streaming." Within tissue, this process strains the tissue by attempting to move it away from the acoustic source. Knightingale and colleagues (e.g., Palmeriand Nightingale, 2010) have developed sophisticated means of generating and analyzing the resulting tissue deformation (see Figure for an example of their technique, here applied transcranially to living rat brain). Myers (2006) offers a means of calculating the maximum displacement of tissue generated by this force.

Finally, the presence of a bubble or any large impedance mismatch increases the acoustic radiation force generated by the absorption of ultrasound.

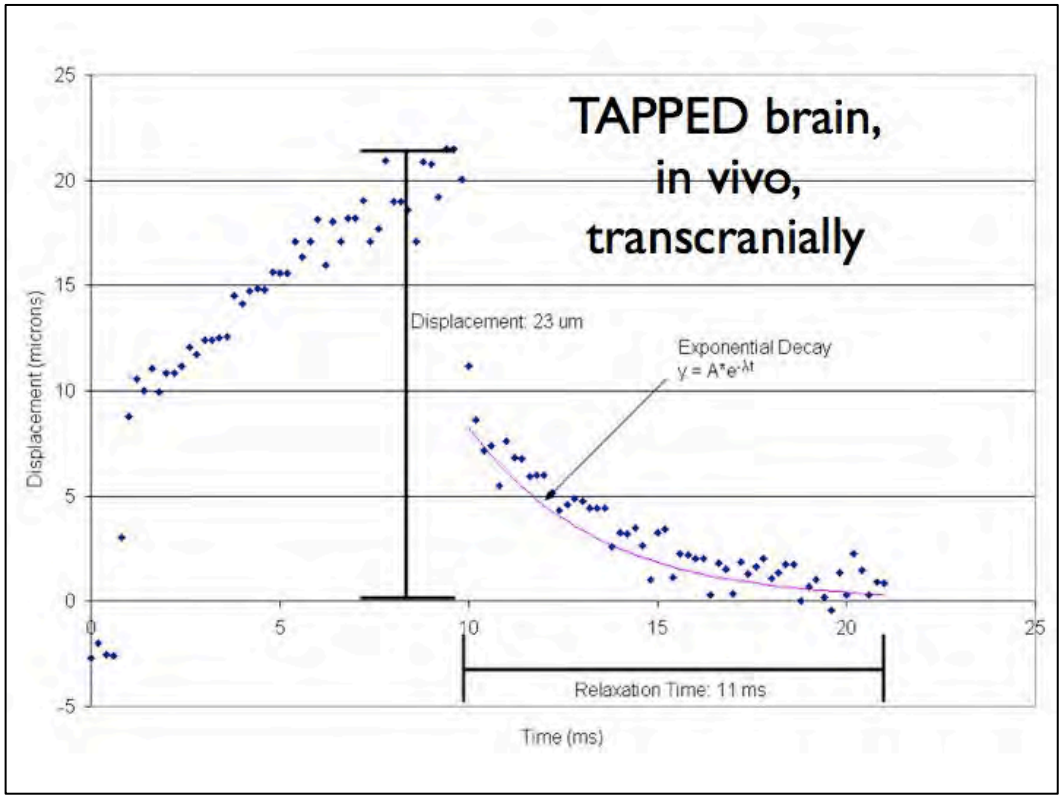

Figure 1. An example displacement of living rat brain, where a single pulse of focused ultrasound was applied through the skull of a rat for 10 milliseconds in duration, with a comparable relaxation time. The maximum displacement measures less than the radius of a typical human hair.

If two (or more) confocal transducers apply at their mutual focus ultrasound with slightly different frequencies, the resulting momentum will deposit with a 'beat' frequency such that the tissue will move at that frequency, in a field now known as vibroacoustography. Analysis of the resulting acoustic emissions gives information about the properties of the material at the focus, such as its stiffness. Greenleaf and

colleagues developed this original idea (Greenleaf BLAH), generating interesting images of arterial plaque, defects in industrially derived materials and other relevant examples where variations in stiffness can be expected. One may find a detailed study of the physics of vibroacoustography in Silva and Mitri (2011).

4.3 Acoustic Cavitation

Excellent surveys of cavitation review bubble formation and growth; bubble dynamics (the properties and behavior of isolated or communities of bubbles when stimulated by ultrasound, including bubble scattering and emission); mechanical effects of bubbles, including microstreaming and hydrodynamic jet and shock formation; and sonochemistry. Here I would include classics such as Leighton (1994); Brennan (1995); and Young (1989); with recent review articles focusing on cavitation and contrast agents (discussed below), such as Wu and Nyborg (2008 – early pioneers of ultrasound in its many forms) as well as Ferrarra's recent article (Caskey et al, 2011), among many. All these physical and chemical processes can occur in vivo with generally profound biological consequences. Given the existence of existing survey articles and books focused on cavitation, I shall highlight only essentials here before moving on to their applications. This general discussion of cavitation will focus on acoustic and bubble behavior in solutions, sometimes adjacent to (tissue) boundaries where current understanding has its firmest underpinnings. Exciting observations in vivo (e.g. Chen et al, 2011) support the utility of this approach.

5. Bubble Formation and Growth

In practice water will cavitate at low ultrasonic frequencies at pressure amplitudes of a few tenths of a MPa. However, in theory the threshold for cavitation of water should be a hundred times this pressure, based on the tensile strength of pure water. A significant reason for this disparity is the presence of impurities within water (Crum and Fowlkes, 1986). Examples include dust, which can trap minute quantities of gas within cracks on its surface, or microbubbles within the fluid stabilized by a skin of surfactant. (Electromagnetic radiation in the form of gamma rays represents another source of cavitation nuclei, independent of the purity of the liquid.) These are nascent bubbles, or “cavitation nuclei.” The amplitude necessary to form a bubble from these sources, known as the “cavitation threshold,” increases with increasing frequency and surface tension, for example, among a host of other parameters.

Once created, the oscillating sound field will cause the bubble's size to oscillate within an acoustic cycle. Continued acoustic stimulation of a free bubble will cause that bubble to grow, at least initially, via a process known as "rectified diffusion.”Rectified diffusion (Crum, 1984) describes the net effect on bubble size over a few to many acoustic cycles of changes in both the concentration gradient of diffusing gases near the bubble's surface (generally of prime importance) and the surface area of the bubble (generally of secondary importance) within an individual acoustic cycle. Briefly, as a bubble expands the bubble's surface area grows as does the concentration gradient of the gas adjacent to the bubble’s surface within the liquid. At the same time, the concentration gradient of the gas inside the bubble adjacent to the bubble surface decreases. All these factors increase the flux of gas from the outside of the bubble to

its inside. When the bubble's size decreases, the surface area decreases and the changes in gas concentration gradient adjacent to the bubble's surface reverse. The net result is an increase in the flux of gas from the inside to the outside of the bubble. However, because of asymmetry in this process (the surface area of the bubble is larger when the bubble is big compared to when it is small), the bubble grows minutely with each acoustic cycle and significantly over many acoustic cycles.

5.1 Bubble Dynamics

Bubbles, like springs, have a primary resonant frequency. For bubbles, this frequency varies inversely with the bubble’s radius and also strongly depends on gas content and surface tension among other factors. (Leighton, 1994 offers a masterful text on this and other processes involved in cavitation.) Newly formed bubbles within relatively weak acoustic fields often have a resonant frequency that is different from the applied frequency, making their temporal variations in volume both within an acoustic cycle and over many acoustic cycles initially small and sinusoidal. (“Stable” or non-inertial cavitation refers to bubbles undergoing such relatively simple volumetric changes where factors in addition or instead of the inertia in the surrounding fluid govern the bubble behavior.) Under these circumstances the bubbles both scatter sound (because of their geometric properties and their impedance mismatch with the surrounding fluid) and emit sound (via the compression and rarefraction of the liquid surrounding the bubble) at the frequency of the applied signal. Generally the emitted sound has a larger amplitude than the scattered sound. As the bubbles grow toward their resonant frequency (which can happen in only a few cycles) or, as the applied

sound field increases, the volumetric changes in the bubble evolve to more complex functions of time within an acoustic cycle, as do the acoustic emissions, whether or not those changes remain radially symmetric. As a function of growing bubble amplitude, those emissions first include the superharmonics of the applied signal. Eventually, the once stably oscillating bubble collapses violently and/or becomes asymmetric. The individual “mother” bubble may break down at this point into a small cloud of microbubbles - known as "daughter" bubbles. With continued acoustic stimulation, the process of bubble growth and eventual destruction will re-commence. Without continued acoustic stimulation the bubbles will eventually decay or float away. With an appropriately timed re-start of the applied sound, as in pulsed applications of ultrasound, these daughters may be optimally configured for acoustically driven growth or violent collapse, as desired. Before the finish of possible daughter production, but requiring continued acoustic stimulation, will be larger-amplitude, broad-band acoustic emissions over a greater range of frequencies and the eventual emission of multiples of the subharmonic of the applied signal. The detection of these emissions via a hydrophone(e.g. various papers by Ron Roy such as his early paper Roy et al (1990)offers a means of remotely assessing the level of cavitation activity within insonified material and often correlates with a variety of mechanical and chemical effects associated with cavitation, to which we now turn.

5.2 Microstreaming

Pulsating bubbles generate vorticity and hence a viscous boundary layer within the liquid adjacent to their surface. The shear in this layer will stress any material in the

solute close to the bubble. Also, the oscillations of the bubble help bring material from afar into the vicinity of the bubble via the induction of a generally steady flow in the fluid known as acoustic microstreaming (e.g. Nyborg, 1965; Leighton, 1994)

There exist a number of studies whose central scientific principle is the use of an isolated bubble (mounted on the end of a minute tube, for example, or induced by a vibrating wire) or a collection of isolated bubbles (formed by hydrophobic membranes containing gas-filled micropores) to allow controlled study of the stable-cavitation process. Rooney (1970) made use a 250-mm diameter bubble suspended at the end of a small tube within a vial of red blood cells stimulated by a 20-kHz sound source to measure the shear stresses necessary to create hemolysis. This value - about 450 Pa – was consistent with those determined experimentally with a standard viscometer, validating the supporting theory. Miller et al (1979) shows platelet aggregation created by a stably cavitating bubble. A much more recent example developed more analytical detail and documented analytically and in video the powerful shear forces around cavitating bubbles and their effect on cells (Marmottant and Hilgenfeldt, 2003). Also, Coakley and Nyborg (19778)make an instructive calculation of the strength and reach of microstreaming for a microbubble with a resting radius of 3.3 mm that is resonant at 1 MHz. For a weak, driving pressure of 5,000 Pa, the bubble's amplitude variation will be a tenth of its resting radius. Platelets in saline drawn to the bubble's surface will arrive there with a velocity of about 1.3 m/s, while platelets two resting radii away from the center of the bubble will approach with a velocity of 0.0004 m/s, which gives a sense of the reach of the streaming field. Nonetheless, these velocities are significant: they

calculate that it would take about 0.003 s to clear the space around the vibrating bubble out to two resting radii from the center of the bubble.

Bubbles are not ordinarily present within the fluid within human beings but can and have been introduced to enhancing imaging and to disrupt the blood-brain barrier, as we discuss below. (Tanter's group has performed an interesting study searching for cavitation in sheep's brain – Gateau et al, 2011.) This means that without their introduction, for medical ultrasound to be dangerous in vivo it must initiate as well as stimulate acoustic bubbles. This generally requires the production of "inertial cavitation," to which we now turn.

6. Inertial cavitation and associated material stresses

A bubble may collapse asymmetrically because its amplitude becomes large enough that only inertial forces govern the collapse (during the process of "inertial" cavitation) or because it is near an interface such as that formed by a container, blood vessel or another bubble. The result will be irregular and a-periodic microstreaming and hydrodynamic jet formation. This microstreaming has been recently documented using in vivo and ex vivo videography to stretch, deform and tear at blood vessels within reach of the bubble (again, Chen et al, 2011), a desirable process for therapeutic effects such as facilitating drug delivery, a dangerous process in the context of most diagnostic applications of ultrasound.

The inertial collapse of a bubble can occur within a single acoustic cycle, and therefore the potential for inertial cavitation cannot be eliminated even for very short pulses of ultrasound. This fact forms the basis of the analysis behind the creation of the

"mechanical index" (by Apfel and colleagues – Holland and Apfel, 1989; Apfel and Holland, 1991), an index used in diagnostic ultrasound machines to avoid the possibility of inertial cavitation in vivo, to which we turn now.

7. Mechanical Index

For diagnostic purposes, cavitation poses an obvious danger when one considers the mechanical, thermal, and chemical effects associated with it. Apfel and Holland, noted above, developed a conservative measure for the onset of inertial cavitation of a pre-existing bubble subjected to one cycle of applied acoustic pressure, called the "mechanical index." They chose inertial cavitation because associated with it are the potentially deleterious processes one can expect due to cavitation in the human body, where stable cavitation is quite unlikely. This measure is proportional to the peak negative pressure amplitude and inversely proportional to the square root of the frequency of the applied sound. Its governing assumptions include isothermal growth of an optimally sized bubble, the neglect of gas diffusion into the bubble, and that the fluid surrounding the bubble is incompressible. (All these assumptions produce the most violent bubble collapse, making the mechanical index as conservative as possible.) Their theory predicts the value of the mechanical index associated with the circumstances under which their theoretical bubble produces internal temperatures of 5,000°C, which they argue diagnostic ultrasound machines should not exceed. Their basic approach has been accepted, and diagnostic ultrasound machines display a measure of the mechanical index that varies from application to application based on extensions of the original work of Apfel and Holland.

Hynynen (1991) measured the cavitation threshold in muscle. It remains the definitive experimentally determined reference on the subject. Interestingly, cavitation in tissue may explain observations of significant (around 10°C) increases in temperature generated within tissue or in vitro, because of simultaneous measurements of strong, broadband acoustic emissions and hyper echogenicity within the tissue (e.g., Holt and Roy, 2001). This points to the presence and therefore possible thermal significance of bubbles in the same area as the large temperature rise of a size too large to be explained by standard, bubble-free absorption of ultrasound by the tissue. This represents an area of on-going research; the current consensus is that focal generation by cavitating bubbles of a large range of harmonics of the incident ultrasound energy causes rapid generation of heat local to the bubble due to the absorption of those harmonics, hence a rapid temperature rise in the tissue (Holt and Roy, 2005).

8. Diagnostic Ultrasound

8.1 Standard Diagnostic Imaging

There exist a multitude of useful and practical overviews of diagnostic ultrasound. A classic text is Kremkau (1998). The basic concept of diagnostic ultrasound resides in the notion that sound backscattered from tissue does so as a function of the acoustic impedance and position of that tissue, and that the acoustic impedance and position tell you something fundamental about the tissue. In standard applications, that "something fundamental" is the structure and hence identity of the tissue. So-called "A" mode ultrasound produces a simple, one-dimensional trace of backscattered echoes. This modality is useful for applications of diagnostic ultrasound to the eye, for example,

where capturing structure in more than one dimension is not the issue. In "B" mode imaging, a series of "A" mode scans at different angles from the diagnostic source are collected together to form two-dimensional maps of the backscatter values as functions of distance and angle relative to the acoustic source/receiver. In "M" mode imaging, an A mode scan is followed in time, producing a time-distance trace that finds particular use in imaging the heart with its periodic motion. Besides imaging stationary or moving structure, one can measure the speed and direction of moving tissue and fluids (blood is by far most analyzed in this fashion) via "Doppler imaging." Doppler imaging takes advantage of the fact that blood moves relative to the direction of acoustic wave propagation to create images based on the strength and direction of the Doppler shift in the backscattered signal.

Important clinical examples of Doppler for the brain including monitoring for vasospasm (the constriction of cerebral blood vessels, producing ischemic damage downstream of the blood vessel), and emboli entering the brain, which can occlude blood vessels through the formation of blood clots, again producing ischemic effects (e.g., Tsivgoulis et al, 2009).The practical details of these existing imaging methods, the avoidance of bioeffects, and the search for new imaging modalities make diagnostic ultrasound a challenge. As an example of an imaging detail, diagnostic ultrasound based on acoustic backscatter requires the careful interleaving of transmitted and received acoustic energy with the assumptions that one can translate time of flight into distance using a standard speed of sound. Artifacts in acoustic images can arise when these assumptions break down. Also, acoustic shadows form within tissue owing to the

strong absorption of sound by one tissue type that lies between the acoustic source and another tissue type.

However, when successful, diagnostic ultrasound can create spectacular images, useful for diagnostic of peripheral and central nervous system disorders. For example, a paper by Kermarrec et al (2010) demonstrated the surprising anatomical detail afforded by recent diagnostic ultrasound machines for imaging peripheral nerves and their associated diseases in a manner that compares favorably with MRI. Peripheral nerves consist of axons, Schwann cells, and connective tissue sheaths. The endoneurium is a connective tissue sheath consisting of loose vascular connective tissue and extracellular fluid. A peripheral nerve is held together by the epineurium and consists of one or more nerve fascicles, which in turn is made up of bundles of endoneurium and nerve fibers. Currently, ultrasound provides the greatest resolution for peripheral nerves, is non-invasive, and low-cost. It also provides dynamic imaging and is capable of being moved to image the entire length of a peripheral nerve. Some recent major improvements to ultrasound that make it even more useful for imaging peripheral nerves include high frequency high-resolution broadband transducers, artifact reduction software, and real-time spatial compound ultrasound. Ultrasound's high resolution allows clinicians to detect lesions on nerve fascicles and differentiate them from lesions of the interfascicular epineurium. Extended field-of-view techniques allow clinicians to more easily depict neurogenic tumors, as the technique displays the abnormal structure and the adjacent structures as a whole, making it possible to measure large lesions and tumors. MR, in contrast to ultrasound, does not have a high enough resolution to image small distal nerves. Ultrasound is also advantageous in that it is cheaper than an MRI

machine, has a higher spatial resolution, can travel along a nerve, and has dynamic imaging capabilities. Disadvantages to the use of ultrasound for diagnostic imaging of peripheral nerves include operator dependency, especially a steep learning curve, and the inability of high-frequency ultrasound to resolve deep nerves due to its high attenuation by the intervening tissues.

8.2 Sonoelastic Imaging

A physician's palpation of tissue--essentially, a low-frequency interrogation of the elastic properties of tissue--gives them information on tissue not contained within standard diagnostic images. Sonoelastic imaging works on the principle behind palpation by taking advantage of the fact that differences in elasticity between tissue types may range over several orders of magnitude, whereas differences in acoustic impedance (the sound velocity times the density of the material) vary by less than an order of magnitude. To perform sonoelastic imaging one first creates a standard B-mode image of the tissue in question. One then displaces the tissue, and collects another B-mode image. Direct comparisons of the two images – specifically, direct comparison of highlights in local ultrasound speckle patterns - highlight regions with different elastic properties. This is because softer tissue will move more for a given push than stiffer tissue from one B-mode image to another.

For example, consider Scholz et al (2007), who used 'exogenous' imaging to image tumors in patients with brain lesions. They achieved this exogenous imaging by vibrating the brain tissue directly using an ultrasound scan head. Selbekk et al (2005) has shown that elastographic imaging can be done intra-operatively through

'endogenous' imaging, using the natural pulsatility of the brain from the pulsatile arterial blood to generate tissue displacements and measure the stiffness of the brain tissue. These measurements of strain were used to aid in tumor interpretation based on spatial variations in the pattern of strain, images with larger dynamic range, hence greater contrast, than B-mode images, with their basis in differences in tissue density and bulk compressibility.

Kucewicz et al (2007, 2008) created images of endogenous brain tissue displacement in healthy humans, images whose average amplitude varied with arterial CO_2 blood gas concentration, a known determinant of brain tissue pulsitilty, and with brain use: in essence an ultrasound-based functional brain mapping technique. With that technique we have imaged traumatic brain injury in preliminary studies (Figure).

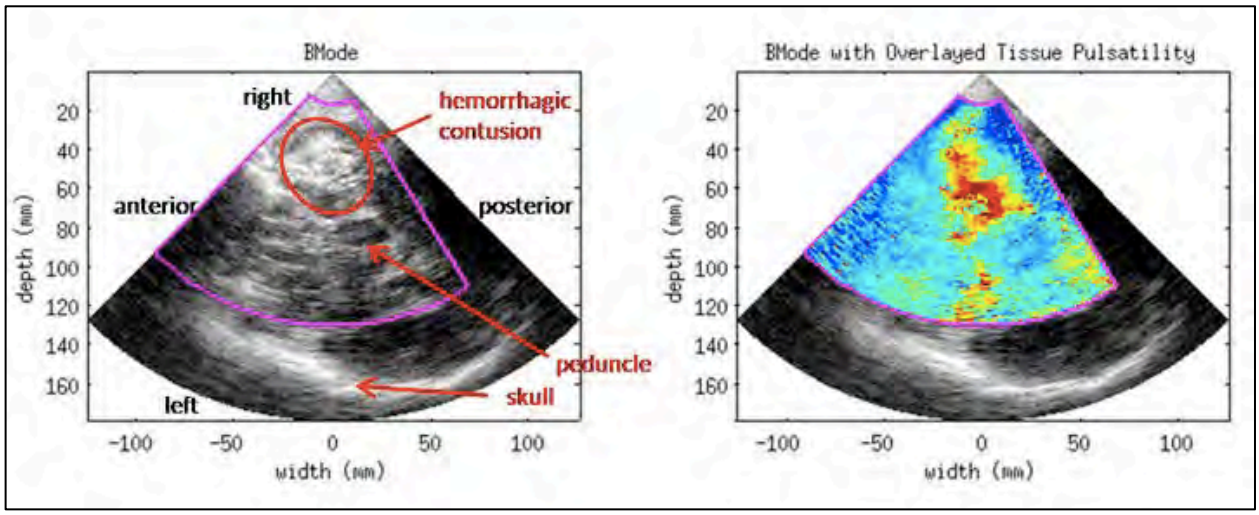

Figure 2. B-mode, transcranial image of human brain after TBI (left) with simultaneously measured endogenous tissue pulsatilty image (right). The hemorrhagic contusion preferentially scatters diagnostic ultrasound back to the scan head (B-mode imaging) and elevates the local pulsatility of the tissue.

Another ultrasound technique (Tanter et al, 2008) tracks shear waves propagating through tissue to create quantitative estimates of the shear modulus of tissue. Here, specialized sequencing of a conventional US diagnostic probe generates a series of impulsive pushes of tissue via the acoustic radiation force associated with focused diagnostic ultrasound, thereby creating transient, propagating and non-destructive shear waves. While the shear waves propagate the device rapidly switches its ultrasound protocol to an ultrafast diagnostic image acquisition (on the order of thousands of B-images per second) to image the propagating shear wave. Local measurement of shear-wave propagation yields a direct estimate of the local shear modulus of the tissue through which the shear wave propagated.

We used a diagnostic ultrasound machine produced by SuperSonic Imagine, Inc (SSI) to image variations in stiffness associated with ischemic stroke within the brain's of mice. A difference in stiffness values can be seen between ischemic brain and normal brain as seen in figure below. Tanter's group currently leads this effort, producing beautifully detailed images of rat brain using a commercial machine based on tracking propagating shear waves.

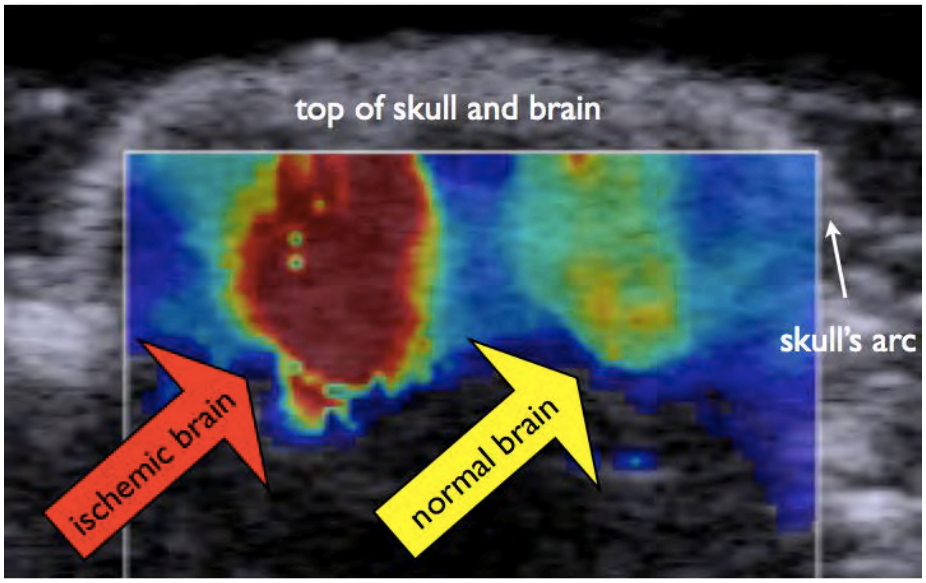

Figure 3. Coronal image of perfusion-fixed mouse brain after stroke taken with a research version of the commercial Super Sonic Imagine device. Color maps the quantitative modulus of the brain, with red denoting stiffer tissue, yellow to blue denoting softer tissue. Gray background denotes superimposed conventional B-mode ultrasound image. Here the ischemic tissue has taken up more fixative than normal tissue, producing stiffer brain tissue on imaging.

8.3 Contrast Agents

The previous discussion of cavitation has laid the groundwork for this section, in which I focus on exogenous acoustic contrast agents. Here we define "acoustic contrast agent" as an artificial bubble on the order of one micron in radius placed within the blood stream for the purpose of increasing the usefulness of an ultrasonic diagnostic process by virtue of the difference in acoustic properties between the agent and the biological tissue or fluid. One can attach a variety of substances to contrast agents –

DNA, drugs, antibodies – to facilitate their targeting for specific imaging purposes, or to create a therapeutic effect (reviewed in Caskey et al, 2011).

As stated above, manufactured acoustic contrast agents are typically micron-sized artificial bubbles placed within the blood stream for the purpose of increasing the brightness of (desirable parts of) images created with diagnostic ultrasound. Contrast agents are typically brighter than the tissue in which they reside most importantly because the contrast agents are acoustically active bubbles that ultrasound stimulates to emit sound more than the surrounding tissue can backscatter sound. In addition, contrast agents, like regular bubbles, oscillate in the presence of ultrasound, thereby emitting ultrasound, at both the incident frequency in addition to harmonics of that applied frequency. Monitoring those acoustic emissions with a diagnostic ultrasound machine lies at the foundation of "harmonic imaging."Specifically, one applies ultrasound at a given frequency to tissue perfused with contrast agents then listens for the emission by the contrast agents of sound at generally twice that frequency. Since those harmonic emissions have much larger amplitude--by a factor of 1000--than that scattered by tissue the regions carrying the contrast agents stand out significantly in images made using the harmonic emissions, thus facilitating the imaging of fine structure within the tissue.

Assaying the quality of the local vasculature represents a clinically useful application of contrast agents for imaging. The first step requires achievement of steady-state perfusion of tissue by contrast agents under ultrasound imaging, followed by application of a relatively intense burst of ultrasound within a volume of tissue of interest. This burst destroys the contrast agents at the focus, changing that region’s

ultrasound backscatter signature from bright to relatively dark. The user then tracks the temporal evolution of the re-entry of contrast into the region of interest by tracking the rate of return of high-ultrasound backscatter within that region. Relative to control tissue – either from a cohort of healthy volunteers or from contralateral tissue, gives a measure of the vascular health of local tissue. Meairs and colleagues (Meairs et al, 2000) produced a lovely early example of a clinical application of this approach, whereby they images two hemispheres of the brain of a patient who had an ischemic stroke. The hemisphere ipsilateral to the stroke took much longer to re-perfuse than the contralateral hemisphere, consistent with the reduced blood flow one would expect to find distal to a major stroke.

It is possible to target acoustic contrast agents to tissues of interest to the clinicians through placement on the bubbles ligands that bind the bubbles to that tissue. Where there exist unique and fairly common cell markers – often for peripheral tumors – acoustic contrast agents have found utility enhancing the ability of ultrasound to create clinically useful images. This remains very much an area of early investigation for brain, where unique and wide-spread cell-surface markers for primary brain tumors remain largely unidentified.

Imaging fine structure and blood flow within a fetus in utero represents another exciting (and potentially perilous) application of contrast agents with ultrasound for diagnostic purposes. A particularly fascinating study (Denbow et al, 1997) showed that contrast agents injected into one of a pair of fetal twins in utero led eventually to the appearance of those contrast agents in the other twin, thus confirming the diagnosis that the circulation system of each twin communicated with the other through their

connection with the mother. The researchers reported no adverse side effects. Concern for fetal harm makes such applications the exception rather than a rule.

Diagnostic ultrasound's safety has been extensively studied, as reviewed numerous times (Abramowicz, 1997; ISUOGEC, 2007). A recent paper raises interesting questions about large doses of diagnostic ultrasound, such as one might encounter during pregnancies that result from in vitro fertilization, where monthly monitoring, or more, is the norm. In this paper (Ang et al, 2006) they insonified pregnant mice in 15-minute sessions for a range of total insonification times from 15-60 minutes. They found disturbed neuronal migration into the cortex of the mice for total insonification times between 30-60 minutes relative to sham-treated controls. This is a topic worth watching. In the meantime, by all means use diagnostic ultrasound to assay the health of the fetus following the usual rules: use just enough to get the data you need for the assay, and stop. These are the guidelines in place now – worth following.

9. Therapeutic Ultrasound

The excellent book by Williams (1983) offers an extensive classic survey of the desired and undesired bioeffects of ultrasound as found in the literature prior to 1983. Readers interested in the roots of many aspects of therapeutic ultrasound should turn to this book. For a more recent survey, Jagannathan et al (2009) highlights the history of therapeutic ultrasound applied to the brain. This represents a quite important summary worthy of detailed study. Especially interesting to this reader is that the earliest applications of ultrasound were to the brain date to the time of the Great Depression, with serious and efficacious human trials in the 1950s led by the very famous Fry

Brothers, whose publications remain a source of inspiration and teaching, many decades later (Fry, 1958).

Therapeutic ultrasound acts via the physical, chemical and thermal forces that it can generate, with its efficacy often affected in very specific ways by the biological disease, and the biological tissue to which it is applied. In this section I first discuss general issues involving therapeutic ultrasound, then highlight several interesting applications specific to the brain.

9.1 Rapid heating with ultrasound for therapeutic effect

Cancer cells die when sufficiently warmed sooner than normal cells under the same conditions. This has been codified in the classic paper by Dewey and Sapareto (1984). Put briefly, for every 1°C increase in temperature above 43°C, where it takes approximately an hour to kill cells, the time necessary to kill cells via denaturation of proteins (this is what happens to the proteins in eggs when cooked for breakfast, for example) decreases by a factor of two. As an example, when cells are warmed to 50°C it takes approximately two minutes to kill them. Early work using ultrasound to create such modest increases in tissue temperature failed in practice because active and responsive perfusion by blood vessels at the capillary level (primarily) fought against the externally generated hyperthermia, made it difficult for researchers to maintain the appropriate temperature for the desired length of time. Thanks to new transducer technology, the current approach is to rapidly raise the temperature of tissue focally with high intensity focused ultrasound (HIFU), thereby creating a therapeutic effect before

significant perfusion and diffusion can bring the tissue temperature back down out of the therapeutic range.

From the beginning, Ter Haar and colleagues have been among the world leaders in this field, with an emphasis on liver and prostate (ter Haar G and Coussios, 2007). Since liver surgery often produces dangerous amounts of bleeding, the ability of this methodology to cauterize tissue around the edges of where it kills tissue is particularly attractive. Another attractive feature of acoustic surgery is its extracorporeal application, particularly compelling for treating prostate cancer, where damage to local neuronal tissue through standard surgery causes all kinds of issues for the patient.

Problems remain with this therapy, however. A particularly interesting issue is the unwanted generation of cavitation within the tissue of interest. Cavitation in the context of HIFU can cause the distortion of the intended acoustic lesion. In particular, the lesion tends to grow towards the transducer by pre-focal heating apparently created by the backscatter properties of the bubbles formed at the initial site of cavitation. This creates volumes of tissue destruction that may encompass tissue that the clinician would like to spare. At the very least, cavitation within a given lesion tends to shield tissue beyond the site of cavitation, due to the large increase in acoustic impedance at the site of cavitation.

Regardless of the kind of therapeutic effect one may wish to create within a given portion of the brain – heating, cavitation, or a combination there of, particularly problematic for using HIFU to treat the brain is the presence of the skull. As discussed above, bone severely attenuates propagating ultrasound. It also distorts that propagation, rendering what would be a tight focus of HIFU with the size and aspect

ratio of a grain of rice into one or several smears of ultrasound application. Clinical devices such as by Insightec use magnetic resonance imaging (MRI) to guide HIFU emitted transcranially from a hemispheric distribution of hundreds of individual transducers. (O'Reilly and Hynynen, 2012)To paint a therapeutic volume of HIFU with a desired shape, users generate asynchronous emissions of HIFU from those transducers – a pre-distortion, if you will - such that after the sound crosses into the brain the sound propagates synchronously to create the desired HIFU shape and intensity at the target of interest. Design of the initial pattern of HIFU emission often requires knowledge of the propagation path the HIFU will encounter, derivable from CT images of the patient's head. A more recent approach focuses HIFU experimentally, by MRI-based monitoring then modulation of the shape and position of the HIFU focus through monitoring of the shape and position of displaced brain generated created by the acoustic radiation force (again, see the very recent review article by O'Reilly and Hynynen, 2012).

Quite exciting work summarized in the review article by the Fry brothers dealt with the treatment of tremors in patients with Parkinson's disease (Fry, 1958; see the extensive review of the early literature – Jagannathan et al, 2009). The researchers report that they were able to repeatedly create within a given human patient (they successfully treated 18 different patients in this fashion) the reversible alleviation of tremors, which they eventually removed permanently by a larger dose of ultrasound than that required to create the transient effects. Apparently side effects of this procedure were minimal.

This original work required neurosurgical procedures to expose the brain to facilitate HIFU delivery. Very recently, Jeanmonod and colleagues (Martin et al,

2009)revisited this clinical problem, with modern, MRI-guided HIFU capable of generating therapeutic lesions in the central lateral thalamic nucleus of the brain's of patients experiencing chronic pain. The patients remained awake throughout the procedure, did not require any neurosurgical intervention to facilitate delivery of HIFU, suffered no adverse events, and months after the procedure a majority reported reduction of their pain.

9.2 Thrombolysis

Breaking up unwanted blood clots is a difficult process and often an invasive one. Studies over the twenty years or more (reviewed in Balucani and Alexandrov, 2010)indicate that 1-MHz ultrasound at intensities of 1—8 W/cm^2 accelerates the enzymatic reactions in thrombolysis rather than causing irreversible mechanical fragmentation, via a process known as ultrasound-enhanced thrombolysis. Ultrasound seems to do so by enhancing the transport of reactants, since experiments in vitro demonstrate that ultrasound increases transport of plasminogen activators both into and within thrombi. This is important because transport of reactants into and within thrombi is a rate-limiting step in fibrinolysis *in vitro* and therapeutically. The physical mechanism or mechanisms responsible for enhancement of fibrinolysis are unknown, but bulk heating alone is not a sufficient explanation. Cavitation could be important in systems exposed to air, for example, most in vitro experimental systems, or in animal models that include surgical exposure of the vessel. However, ultrasound also accelerates the destruction of blood clots in deep vessels within animal models under circumstances where cavitation is not likely to occur. One example is in animal models of small vessel

injury. Another is electrically induced thrombosis, in which the method of vessel injury does not include introduction of gas. Moreover, seminal in vitro work designed to assess the relative importance of cavitation versus other nonthermal acoustic mechanisms (acoustic streaming, for example) has found that only 50% of ultrasound-enhanced thrombolysis in vitro can be explained by cavitation (Everbach et al, 1997).

Despite uncertainty in the mechanisms by which ultrasound facilitates clot destruction, there exists clinical work using ultrasound alone (CLOTBUST–Alexandrov et al, 2004) or with acoustic contrast agents (TUSCON–Molina et al, 2009) have shown exciting results, with some reason for caution from TUSCON given the increased risk of too rapid reperfusion of the ischemic tissue and possibility of intracerebralhemorrhage.

10. Ultrasound-facilitated delivery of drugs and antibodies into the brain.

One of the more important and exciting applications of therapeutic ultrasound is to facilitate the delivery of therapeutic agents beyond the blood-brain barrier (BBB) into brain parenchyma to achieve a variety of therapeutic effects for big-time diseases such as tumors and any of the distressingly large number of neurodegenerative diseases. The BBB consists of specialized capillaries that form the lining of the blood vessels within the brain, a thick basement membrane, astrocytic endfeet and pericytes that restrict movement of chemicals that make it past or through the endothelial cells. The specialized endothelial cells restrict the diffusion of microscopic objects and large molecules into brain tissue in part by having unusually snug connections between adjacent endothelial cells (called tight junctions) as well as deploying an extensive array of pumps that pump back into the blood stream most chemicals that make it into the

endothelial cells themselves. One class of approach to getting drugs past the blood-brain barrier includes implantation of drug pumps where they can place chemicals into cerebral spinal fluid. Another approach consists of intra-hemispheric delivery of 'osmotic' agents (mannitol and the like) that disrupt the blood-brain barrier for 15-30 minutes. Another class of approach connects therapeutic drugs to peptides that are known to pass through the blood-brain barrier – a kind of Trojan horse approach. Like anything in life, these approaches have limitations, such as requiring a neurosurgical procedure, or exposing too much of the brain to the chemicals in the blood that can harm brain tissue, or delivering an insufficiency of drug.

There are hints of ultrasound's ability to disrupt the BBB in the 1950s and 1960s, always in the context of studying HIFU-induced lesions in brain. There was important new work in the field in the 1990s and early 2000s. Since then the technique has been honed extensively, primarily by the 'Harvard' group and their disciples ably reviewed recently in O'Reilly and Hynynen (2012).

HIFU has been explored as a way to increase BBB permeability to drugs, to treat tumors (Mourad and Silbergeld, 2005; Tempany et al, 2011), and movement disorders, Alzheimer's, etc (Hynynen, 2010; O'Reilly and Hynynen, 2012). HIFU has many advantages in that it can noninvasively deliver a focused beam to a discreet region of the brain with minimal effects in adjacent tissue fields. Originally, HIFU could only effectively be delivered through a cranial window (a hole in the skull). Original studies delivered so much energy that the HIFU not only produced BBB disruption, but also necrosis of the surrounding brain tissue. Later studies by Ballantine reduced energy levels that produced BBB disruption without tissue necrosis, although there were still

hemorrhagic areas (Ballentine et al, 1960). These results led to the conclusion that further adjustment to HIFU parameters could produce BBB disruption without any damage, including hemorrhage, something we showed using HIFU delivered via cranial window (Mesiwala et al, 2002). Moreover, our electron microscopy showed that this method of ultrasound disrupted the tight junctions between the endothelial cells, which are responsible for the impermeability of the BBB.

Follow-on work reported by Mourad and Silbergeld (2005) and at conferences made use of an intra-operative device working at comparable ultrasound parameters to disrupt the BBB at and near the surface of the brain (Figure 4) with dye flux volumes that were, on average, three times larger than the volume of damaged tissue. Parallel studies done with the same ultrasound system and tritiated chemotherapeutic agents relevant to the treatment of brain tumors demonstrated enhanced flux of those drugs from the bloodstream and into the same brain tissue that demonstrates enhanced dye flux. In this case, verapamil, a calcium channel blocker, was required to facilitate *net* drug flux, while dye always crossed the BBB.

A

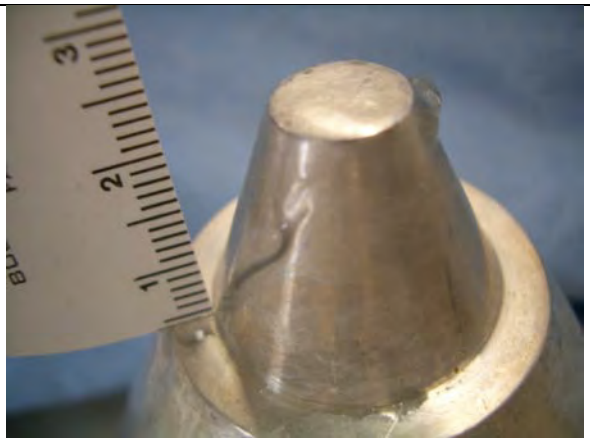

B

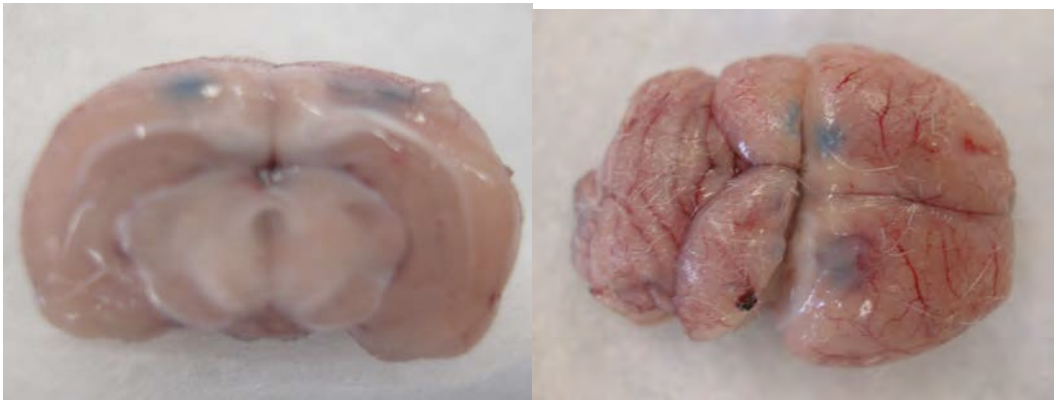

C

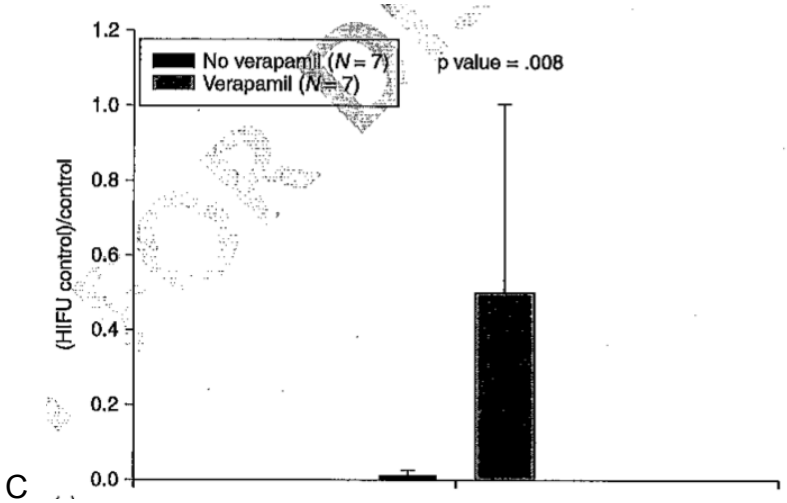

Figure 4. A solid cone HIFU device for opening the blood-brain barrier intra-operatively. (B) When applied to the exposed cortex of rats, it reliably produced BBB

opening to Evans blue. (C) This same procedure, with the addition of verapamil, facilitated net drug flux into brain tissue.

Important papers demonstrating drug flux into brain facilitated by ultrasound, including the earliest to do so, include Treat et al (2007) and Raymond et al (2008). These and other studies of BBB disruption using ultrasound have not required calcium channel blockade for the delivery of drugs or antibodies to brain tissue, consistent with observations there exist a variety of mechanisms by which HIFU can facilitate drug delivery across the BBB, tied in part to the physics behind the particular mechanism (among others, Hynynen, 2010; McDannold et al, 2008).

A particularly interesting set of papers includes Choi et al (2011) and Samiotaki et al (2011), who have explored the minimum ultrasound, by several measures, necessary to produce BBB disruption via the combined effect of HIFU and ACA. They and others explored a range of low pressure (0.13-0.51 MPA), pulse length (typically 1-10 cycles), pulse repetition frequency (10 Hz through 100 KHz) and duration (single session of 60s, or sets of 1000 pulses applied every 0.1 through 10 times per second for many minutes) with several ACAs (Definitity; Sonovue; etc).

Choi et al (2011) in particular sought to use the minimum amount of ultrasound to achieve spatially uniform and reliable BBB disruption through balance of several parameters that minimally stimulate ACA *in situ* while also facilitating their focal replenishment via blood flow from outside the region of HIFU application. They assayed for BBB disruption through quantification of dye flux into brain tissue. They successfully disrupted the BBB and minimized heterogeneity, which remained, however, pointing,

perhaps to a fundamental limitation of this technique, if clinical applications require homogeneous drug flux, that is.

11. Neuromodulation by ultrasound

The Fry brothers have been involved in much of the groundbreaking research in the application of therapeutic ultrasound to the brain. In one extensive review article, William Fry (1958) notes, among other things, that ultrasound applied to the visual cortex of cat's brains can repeatedly suppress in a transient manner various phases of cortical potentials normally evoked by flashing light into the cat's eye. This alteration of brain function by ultrasound has been the subject of recent work by Jamie Tyler, which I summarize here through attention to his latest articles.

Tyler and colleagues (e.g., Tufail et al, 2010) have investigated the influence of low-intensity, low-frequency ultrasound (LILFU) on neuronal activity by transmitting US waveforms through hippocampal slice cultures and within intact mice. They determined that LILFU can remotely and noninvasively excite neurons and network activity through activating voltage-gated sodium and calcium channels. For their work on mice they used single ultrasound pulses containing between 80 and 225 acoustic cycles per pulse for pulse durations lasting 0.16–0.57 ms and they were repeated at pulse repetition frequencies ranging from 1.2 to 3.0 kHz to produce spatial-peak temporal-average intensities of 21–163 mW/cm2 for total stimulus duration ranging between 26 and 333 ms. They studied the influence of these pulsed ultrasound protocols on intact motor cortex by measuring the electrophysiological and behavioral effects of brain activation. The results provide strong evidence that pulsed US can be used to directly stimulate

neuronal activity and action potentials in intact brain circuits. For example, they observed motor circuit responses to ultrasound stimulation by acquiring simultaneous fine-wire EMG and videos of muscle contractions. The US stimulation method shows the high specificity as they were able to map the spatial distribution of neuronal activation triggered by transcranial pulsed US.

To assess the safety of transcranial US brain stimulation in mice, they first examined how pulsed US influenced blood-brain barrier (BBB) integrity and observed no evidence that US produced damage to the BBB. Next they probed the cellular-level consequences of pulsed US on brain tissues using antibodies against cleaved caspase-3 to monitor cell death and no differences were found between the control mice and the mice underwent US stimulation. Indeed, in all the results they presented, none showed significant differences on the structure of the BBB, cerebrovasculature, cell death and brain ultrastructure between the control mice and the mice underwent US stimulation. Hence, they concluded that it is possible to stimulate mouse cortex with their ultrasound protocols in a safe manner.

12. Conclusion

Study of the fundamental physics of ultrasound's interaction with tissue leads directly to an understanding of both diagnostic and therapeutic ultrasound. At its heart, ultrasound consists of a physical phenomena whose reflection from tissue is sensitive to the relative variations in density and compressibility of tissue in a manner that can be enhanced through the introduction of microbubbles in to the vasculature. This forms the basis of diagnostic ultrasound imaging, while those same factors can curtail the

effective propagation of ultrasound to deep tissues. The passage of an ultrasound wave through tissue leaves residual amounts of heat and momentum, minimized for diagnostic purposes, maximized in ways that depend upon the ultimate application, for therapeutic purposes. When applied to the brain, the specifics of neuroanatomy, down to the molecular scale for drug delivery, must be taken into account to achieve ultimate clinical success. This makes applications of therapeutic ultrasound for the treatment of brain disorders a particularly challenging field, and an important one, given the general intractability of many therapeutic modalities for such fearsome diseases as Alzheimer's and Parkinson's disease as well as brain tumors.

References

J.S. Abramowicz, Ultrasound contrast media and their use in obstetrics and gynecology. *Ultrasound Med. Biol.,* 23, 1287–1298, 1997.

Alexandrov AV, Molina CA, Grotta JC, Garami Z, Ford SR, Alvarez-Sabin J, Montaner J, Saqqur M, Demchuk AM, Moyé LA, Hill MD, Wojner AW; CLOTBUST Investigators (2004) Ultrasound-enhanced systemic thrombolysis for acute ischemic stroke.N Engl J Med. 2004 Nov 18;351(21):2170-8.

Ang ESBC, Gluncic V, Duque A, Schafter ME, Rakic P (2006) Prenatal exposure to ultrasound waves impacts neuronal migration in mice. Proceedings of the National Academy of Science. 103(34):12903-12910.

R. E. Apfel and C. K. Holland, Gauging the likelihood of cavitation from short-pulse, low-duty cycle diagnostic ultrasound. *Ultrasound Med. Biol.*, 17(2), 179–185, 1991.

H.T. Ballantine, Jr., E. Bell and J. Manlapaz, Progress and problems in the neurological applications of focused ultrasound. *J. Neurosurg,* 17, 858–876, 1960.

Balucani C, Alexandrov AV (2010) Ultrasound- and microspheres-enhanced thrombolysis for stroke treatment: state of the art. Curr Cardiol Rep. 12(1):34-41.

D. T. Blackstock and M. F. Hamilton (eds.), *Nonlinear Acoustics*, New York: John Wiley & Sons, 1997.

C.E. Brennen, *Cavitation and Bubble Dynamics*. New York: Oxford Univ., 1995.

Caskey CF, Hu X, Ferrera KW (2011) Leveraging the power of ultrasound for therapeutic designs and optimization. J. Controlled Release. In Press.

Mourad PD (2013), "Therapeutic Ultrasound, with an emphasis on applications to the brain" in Nakamura K, Ueha S, eds. Ultrasonic transducers - materials design and applications**.** Woodhead Publishing Ltd.

Chen H, Kreider W, Brayman AA, Bailey MR, Matula TJ (2011) Blood vessel deformations on microsecond time scales by ultrasonic cavitation. Phys Rev Lett. 106(3):034301.

T. Christopher and E. L. Carstensen, Finite amplitude distortion and its relationship to linear derating formulae for diagnostic ultrasound systems*. Ultrasound Med. Biol.*, 22, 1103–1116, 1996.

Cho CW, Liu Y, Cobb WN, Henthron TK, Lillehei K, Christians U, Ng KY (2002) Ultrasound-induced mild hyperthermia as a novel approach to increase drug uptake in brain microvessel endothelial cells. *Pharmaceutical Research* 19(8):1123-1129.

Choi JJ, Selert K, Vlachos F, Wong A, Konofagou EE (2011) Noninvasive and localized neuronal delivery using short ultrasonic pulses and microbubbles. *PNAS* 108(40): 16,359-16,544.

W.T. Coakley and W.L. Nyborg, Cavitation: Dynamics of gas bubbles; Applications. In F.J. Fry (ed.), *Ultrasound: Its Application in Medicine and Biology*. New York, Elsevier, 1978. Chap. 6, pp. 77–159.

L.A. Crum and J.B. Fowlkes, Acoustic cavitation generated by microsecond pulses of ultrasound. *Nature,* 319*,* 52–54, 1986.

L.A. Crum, Acoustic cavitation series: Part Five, Rectified diffusion. *Ultrasonics*, September, 22, 215–223, 1984.

M.L. Denbow, M.J.K. Blomley, D.O. Cosgrove and N.M. Fisk, Ultrasound microbubble contrast angiography in monochorionic twin fetuses, *Lancet*, 349, 773-779, 1997

W.C. Dewey and S.A. Sapareto, Thermal dose determination in cancer therapy. *J. Radiat. Oncol. Biol. Phys.,* 10, 787–800, 1984.

Duck FA (1990) Physical Properties of Tissue: a comprehensive reference book. Academic Press, London.

F. Dunn, P. D. Edmonds and W. J. Fry, Absorption and dispersion of ultrasound in biological media, In Herman P. Schwan (ed.), *Biological Engineering*, Philadelphia: McGraw-Hill, 1969.

E.C. Everbach, J. White and C.W. Francis, Overpressure reduces acceleration of thrombolysis due to ultrasound. *J. Acoust. Soc. Am.,* 102(5), 3154, 1997.

Fatemi M, Greenleaf JF (1999) Vibro-acoustography: an imaging modality based on ultrasound-stimulated acoustic emission. Proc NatlAcadSci U S A. 96(12):6603-8.

W.J. Fry, Intense ultrasound in investigations of the central nervous system. In C.A. Tobias and J.H. Lawrence (eds.), *Advances in Biological and Medical Physics.* New York: Academic, 1958, pp. 281–348.

Gateau J, Aubry J-F, Chauvet D, Boch A-L, Fink M, Tanter M. (2011) in vivo bubble nucleation probability in sheep brain tissue. Phys. Med. Biol. 56:7001-7015.

G. R. ter Haar, Coussios C (2007) High intensity focused ultrasound: physical principles and devices. Int J. Hyperthermia. 23:89-104.

C. K. Holland and R. E. Apfel, An improved theory for the prediction of microcavitation thresholds, *IEEE Transactions on Ultrasonics, Ferroelectrics, and Frequency Control*, 36(2), 204–208, 1989.

Mourad PD (2013), "Therapeutic Ultrasound, with an emphasis on applications to the brain" in Nakamura K, Ueha S, eds. Ultrasonic transducers - materials design and applications**.** Woodhead Publishing Ltd.

Holt RG, Roy RA. (2001) Measurements of bubble-enhanced heating from focused, MHz-frequency ultrasound in a tissue-mimicking material. Ultrasound Med Biol. 2001 Oct;27(10):1399-412.

Holt RG, Roy RA (2005) Bubble dynamics in therapeutic ultrasound. In: Bubble and particle dyamics in acoustic fields – modern trends and applications, Edited by Doinikov AA. Research Signpost, Kerala, India.

K. Hynynen, The threshold for thermally significant cavitation in dog's thigh muscle *in vivo*. *Ultrasound Med. Biol.*, 17(2), 157–169, 1991.

Hynynen K, McDannold N, Vykhodtseva N, Jolesz FA (2001) Noninvasive MR Imaging-guided Focal Opening of the Blood-Brain Barrier in Rabbits. *Radiology.* 220(3):640–646.

Hynynen K (2010) MRI-guided focused ultrasound treatments.*Ultrasonics.* 50(2):221-9.

ISUOGEC - International Society of Ultrasound in Obstetrics & Gynecology Education Committee. *Sonographic examination of the fetal central nervous system: guidelines for performing the 'basic examination' and the 'fetal neurosonogram'.* Ultrasound Obstet Gynecol. 2007 Jan; 29(1):109-16.

Jagannathan J, Sanghvi NT, Crum LA, Yen CP, Medel R, Dumont AS, Sheehan JP, Steiner L, Jolesz F, Kassell NF (2009) High-intensity focused ultrasound surgery of the brain: part 1--A historical perspective with modern applications. Neurosurgery. 64(2):201-210.

R.K. Jain, Chapter 2: Bioheat transfer: Mathematical models of thermal systems. *Hyperthermia in Cancer Therapy,* F. K. Storm (ed.).Boston: G.K. Hall & Co., 1983.

Kelly JF, McGough RJ (2009) Fractal ladder models and power law wave equations. J. Acoust Soc Am, 126(4):2072-2081.

Kermarrec E, Demondion X, Khalil C, Le Thuc V, Boutry N, Cotten A*. Ultrasound and magnetic resonance imaging of the peripheral nerves: current techniques, promising directions, and open issues*. SeminMusculoskeletRadiol. 2010 Nov;14(5):463-72.

L.E. Kinsler, A.R. Frey, A.B. Coppens, and J.V. Sanders, *Fundamentals of Acoustics.* New York: Wiley, 1982.

F.W. Kremkau, *Diagnostic Ultrasound: Principles and Instruments.* 5th ed., Philadelphia, PA: W.B. Saunders, 1998.

Kucewicz JC, Dunmire B, Giardino ND, Leotta DF, Paun M, Dager SR, Beach KW. (2008) Tissue pulsatility imaging of cerebral vasoreactivity during hyperventilation. *Ultrasound Med Biol.* 34(8):1200-1208.

Kucewicz JC, Dunmire B, Leotta DF, Panagiotides H, Paun M, Beach KW. (2007) Functional tissue pulsatility imaging of the brain during visual stimulation. *Ultrasound Med Biol.* 33 (5):681-690.

T.G. Leighton, *The Acoustic Bubble.* New York: Academic, 1994.

Marmottant P, Hilgenfeldt S (2003) Controlled vesicle deformation and lysis by single oscillating bubbles. Nature 423:153-155.

Martin E, Jeanmonod D, Morel A, Zadicario E, Werner B (2009) High-intensity focused ultrasound for noninvasive functional neurosurgery. Ann Neurol. 66(6):858-861.

McDannold N, Vykhodtseva N, Hynynen K (2008) Blood-brain barrier disruption induced

by focused ultrasound and circulating preformed microbubbles appears to be characterized by the mechanical index.*Ultrasound Med Biol.* 34(5):834-40.

Meairs S, Daffertshofer M, Neff W, Eschenfelder C, Hennerici M (2000) Pulse-inversion contrast harmonic imaging: ultrasonographic assessment of cerebral perfusion. Lancet. 2000 355(9203):550-1.

Mesiwala, A. H. , L. Farrell, H. J. Wenzel, L. A. Crum, D. L. Silbergeld, H. R. Winn, and Mourad PD (2002) High Intensity Focused Ultrasound Selectively Disrupts the Blood-Brain Barrier *in vivo. Ultrasound in Medicine and Biology.* 28(1) 389-400.

D.L. Miller, W.L. Nyborg and C.C. Whitcomb, Platelet aggregation induced by ultrasound under specialized conditions in vitro. *Science*, 205, 505–507, 1979.

Molina CA, Barreto AD, Tsivgoulis G, Sierzenski P, Malkoff MD, Rubiera M, Gonzales N, Mikulik R, Pate G, Ostrem J, Singleton W, Manvelian G, Unger EC, Grotta JC, Schellinger PD, Alexandrov AV (2009) Transcranial ultrasound in clinical sonothrombolysis (TUCSON) trial. Ann Neurol. 66(1):28-38.

Mourad, PD (1999) Biological effects of ultrasound. In: Webster, J. L. (editor), "Encyclopedia of Electronics and Electrical Engineering," John Wiley & Sons (Philadelphia), V2, pp.368-386

Mourad PD, Silbergeld DL (2005) Breaking the blood-brain barrier: using high-intensity focused ultrasound to treat malignant brain tumors. *RT-Image.* V18(32):28-32.

Myers MR (2006) tissue deformation induced by radiation force from Gaussian transducers. J. Acoust. Soc. Am. 119(5): 3147-3152.

W.L. Nyborg, Acoustic streaming. In W.P. Mason (ed.), *Physical Acoustics.*Vol. 2, Part B. New York: Academic, 1965, Chap. 11, pp. 265–285.

O'Brien WD (2007) Ultrasound-biophysics mechanisms. Progress in Biophysics and Molecular Biology. 93:212-255.

O'Reilly M, Hynynen K (2012) Ultrasound enhanced drug delivery to the brain and central nervous system. International Journal of Hyperthermia. In press.

Palmeri ML, Nightingale KR. (2011) What challenges must be overcome before ultrasound elasticity imaging is ready for the clinic? Imaging Med. 3(4):433-444.

H. Pauly and H.P. Schwan, Mechanisms of absorption of ultrasound in liver tissue. *J. Acoust. Soc. Am.,* 50, 692–699, 1971.

Raymond SB, Treat LH, Dewey JD, McDannold NJ, Hynynen K, Bacskai BJ. *Ultrasound enhanced delivery of molecular imaging and therapeutic agents in Alzheimer's disease mouse models*. PLoS One. 2008 May 14; 3(5):e2175.

Raymond SB, Skoch J, Hynynen K, Bacskai BJ (2007) Multiphoton imaging of ultrasound/Optison mediated cerebrovascular effects in vivo. *J Cerebral Blood Flow & Metabolism*. 27: 393–403.

J. A. Rooney, Hemolysis near an ultrasonically pulsating gas bubble. *Science*, 169, 869–871, 1970.

R.A. Roy, S.I. Madanshetty and R.E. Apfel, An acoustic backscattering technique for the detection of transient cavitation produced by microsecond pulses of ultrasound. *J. Acoust. Soc. Am*, 87(6), 2451–2458, 1990.

O.V. Rudenko, A.P. Sarvazyan and S.Y. Emelianov, Acoustic radiation force and streaming induced by focused nonlinear ultrasound in a dissipative medium. *J. Acoust. Soc. Am.,* 99, 2791–2798, 1996.

Mourad PD (2013), "Therapeutic Ultrasound, with an emphasis on applications to the brain" in Nakamura K, Ueha S, eds. Ultrasonic transducers - materials design and applications**.** Woodhead Publishing Ltd.

Samiotaki G, Vlachos F, Tung YS, Konofagou EE (2011) A quantitative pressure and microbubble-size dependence study of focused ultrasound-induced blood-brain barrier opening reversibility in vivo using MRI. *Magnetic Resonance in Medicine.* doi: 10.1002/mrm.23063.

Sapozhnikov OA, Maxwell AD, MacConaghy B, Bailey MR (2007) A mechanistic analysis of stone fracture in lithotripsy. J. Acoust. Soc. Am. 121:1190-1202.

Sarvazyan A (2010) Diversity of biomedical applications of acoustic radiation force. Ultrasonics, 50:230-234.

Scholz M, Lorenz A, Pesavento A, Brendel B, Khaled W, Engelhardt M, Pechlivanis I, Noack V, Harders A, Schmieder K. (2007) Current status of intraoperative real-time vibrography in neurosurgery. *Ultraschall Med*. Oct;28(5):493-7.

Selbekk T, Bang J, Unsgaard G. (2005) Strain processing of intraoperative ultrasound images of brain tumours: initial results. *Ultrasound Med Biol.* Jan;31(1):45-51.

Sheikov N, McDannold N, Sharma S, Hynynen K (2008) Effect of focused ultrasound applied with an ultrasound contrast agent on the tight junctional integrity of the brain microvascular endothelium.*Ultrasound Med Biol.* 34(7):1093-1104.

Silva GT and Mitri FG (2011) Difference-frequency generation in vibro-acoustography. Phys. Med. Biol. 56:5985-59923.

Tanter M, Bercoff J, Athanasiou A, Deffieux T, Gennisson JL, Montaldo G, Muller M, Tardivon A, Fink M. (2008) Quantitative assessment of breast lesion viscoelasticity: initial clinical results using supersonic shear imaging. *Ultrasound Med Biol.* Sep;34(9):1373-86.

Tempany CM, McDannold NJ, Hynynen K, Jolesz FA (2011) Focused ultrasound surgery in oncology: overview and principles. *Radiology*. 259(1):39-56.

Treat LH, McDannold N, Vykhodtseva N, Zhang Y, Tam K, Hynynen K (2007) Targeted delivery of doxorubicin to the rat brain at therapeutic levels using MRI-guided focused ultrasound. *Int J Cancer.* 15:121(4):901-7.

Tsivgoulis G, Alexandrov AV, Sloan MA (2009) Advances in transcranial Doppler Ultrasonography. NeurolNeurosci Rep. 9(1):46-54.

Tufail Y, Matyushov A, Baldwin N, Tauchmann ML, Georges J, Yoshihiro A, Tillery SI, Tyler WJ. *Transcranial pulsed ultrasound stimulates intact brain circuits*. Neuron. 2010 Jun 10; 66(5):681-94.

Tung YS, Vlachos F, Choi JJ, Defflieux T, Selert K, Konofagou EE (2011) *In vivo* transcranial cavitation threshold detection during ultrasound-induced blood–brain barrier opening in mice. *Phys. Med. Biol*. 55 (2010) 6141–6155.

Vlachos F, Tung YS, Konofagou E (2011) Permeability dependence study of the focused ultrasound-induced blood-brain barrier opening at distinct pressures and microbubble diameters using DCE-MRI. *Magn Reson Med.* 66:821-830.

A. R. Williams, Ultrasound: *Biological Effects and Potential Hazards.* New York: Academic Press, 1983.

Wu J, Nyborg WL (2008) Ultrasound, cavitation bubbles and their interaction with cells. Advanced Drug Delivery Reviews. 60:1103-1116.

F. R. Young, *Cavitation*. New York: McGraw Hill, 1989.

Evidence of Changes in Brain Tissue Stiffness After Ischemic Stroke Derived From Ultrasound-Based Elastography

Zinnia S. Xu, BS, Rona J. Lee, BS, Stephanie S. Chu, BS, Anning Yao, BS, Marla K. Paun, BS, Sean P. Murphy, PhD, Pierre D. Mourad, PhD

Objectives—Ischemia, edema, elevated intracranial pressure, and reduced blood flow can occur in the brain as a result of ischemic stroke, including contralateral to the stroke via a process known as diaschisis. In this study, ultrasound elastography, an imaging process sensitive to the stiffness of tissue, including its relative fluid content, was used to study changes in the stiffness of individual cerebral hemispheres after transient ischemic injury.

Methods—Elastographic images of mouse brains were collected 24 and 72 hours after middle cerebral artery occlusion. The shear moduli of both ipsilateral and contralateral brain hemispheres for these mice were measured and compared to corresponding values of control animals.

Results—At 24 hours (but not 72 hours) after induction of ischemic stroke, there was a significant decrease in the shear modulus in the ipsilateral hemisphere ($P < .01$) and a significant increase in the shear modulus in the contralateral hemisphere compared to that of control animals ($P < .01$). Significant differences were also evident between ipsilateral and contralateral shear modulus values at 24 and 72 hours after infarction ($P < .01$ for both).

Conclusions—The differences between intrahemispheric averages of shear moduli of the brains of animals with stroke at 24 and 72 hours after stroke induction likely reflect the initial formation of edema and reduction of cerebral blood flow known to develop ipsilateral to ischemic infarction, the known transient increase in intracranial pressure, as well as the known initial reduction of blood flow and subsequent development of edema in the contralateral hemisphere (diaschisis). Thus, elastography offers a possible method to detect subtle changes in brain after ischemic stroke.

Key Words—cerebral stroke; diaschisis; elastography; middle cerebral artery occlusion; ultrasound

Received April 10, 2012, from the Departments of Bioengineering (Z.S.X., S.S.C., A.Y., P.D.M.) and Neurological Surgery (R.J.L., S.P.M., P.D.M.) and Applied Physics Laboratory (M.K.P., P.D.M.), University of Washington, Seattle, Washington USA. Revision requested June 16, 2012. Revised manuscript accepted for publication August 3, 2012.

This work was funded by the Congressionally Directed Medical Research Program.

Address correspondence to Pierre D. Mourad, PhD, Department of Neurological Surgery, University of Washington, Box 356470, Seattle WA 98195-6470 USA.

E-mail: pierre@apl.washington.edu

Abbreviations

MRI, magnetic resonance imaging; TTC, 2,3,5-triphenyltetrazolium chloride

Reduction of cerebral blood flow after stroke produces ischemia and edema in the ipsilateral hemisphere of the brain and globally elevated intracranial pressure as well as induces subtle effects in the contralateral hemisphere, the latter known as diaschisis.[1] Physiologic phenomena associated with diaschisis include a substantial decrease in regional cerebral blood flow of the contralateral hemisphere after middle cerebral artery occlusion, as shown in cats.[2] Furthermore, in addition to characterization of the progression of edema on the ipsilateral hemisphere,[3] others have observed edema in the contralateral hemisphere after ischemic injury on magnetic resonance imaging (MRI) as early as 9 hours after occlusion.[4]

Elastography has been used for many years to detect tissue stiffness and is growing in importance for breast cancer diagnoses.[5] One elastographic method evaluates tissue stiffness by analyzing the rate of propagation of mechanical shear waves generated within tissue through a variety of means, using various ways of monitoring the propagation of those shear waves, such as MRI[6] and sonography.[7]

Ultrasonic shear wave elastography measures local tissue stiffness by assaying ultrasound-induced shear wave propagation. Specifically, the transducer uses the acoustic radiation force to push on the tissue in a focal manner, which creates a shear wave that propagates transversely from its initiation site (Figure 1, A and C). The local speed of shear wave propagation is proportional to the Young modulus with the following relationship: $E = 3\rho c^2$, where E is the Young modulus (kilopascals), a measure of the resistance of tissue to shearing; ρ is the density (kilograms per cubic meter), and c is the speed of shear waves (meters per second). This particular version of ultrasound-based elastography (known as shear wave elastography) is sensitive to the average fluid content in tissue,[7] since shear waves do not propagate through fluid.

This imaging technique was developed to highlight small, stiff, calcified breast lesions within a large, relatively homogeneous field of view. In this study, following the technique shown by Derieppe et al,[8] we used it on small heterogeneous tissue (the brains of mice after stroke), where scattering of the propagating shear waves reduced details from the image (Figure 1, B and C), to assay the temporal evolution of hemispheric averages of brain tissue stiffness after ischemic injury.

Materials and Methods

Middle Cerebral Artery Occlusion

Male C57BL/6 mice (25–30 g) were used for the 45-minute middle cerebral artery occlusion. Anesthesia was induced by inhalation of 3% isoflurane and maintained with 1.5% to 2% isoflurane. Body temperature was monitored throughout the surgery with a rectal probe and maintained at 36°C to 38°C with a heating blanket. A midline incision was made on the ventral surface of the neck. The right common carotid artery was isolated and ligated, after which a 12-mm-long, 6-0 nylon filament was introduced and advanced up through the internal carotid artery and into the middle cerebral artery. Mice were kept under anesthesia for the entire duration of the 45-minute occlusion. After the occlusion, the filament was pulled back and removed from the artery to allow for reperfusion. Cerebral blood flow in the area was monitored during the occlusion and reperfusion with a laser Doppler device (MoorLab laser Doppler perfusion monitor; Moor Instruments, Inc, Wilmington, DE). Mice were euthanized either 24 or 72 hours later by cervical dislocation.

Control animals did not undergo surgical preparation. Pilot studies by us performed over the years have shown no difference in brain structure as shown by MRI and histopathologic examination between control animals that received the sham surgery and control animals that received no surgical procedure. Therefore, at the urging of our local Institutional Animal Care and Use Committee, we chose to use controls without surgery for this imaging study. There were a total of 13 control mice and 16 mice that underwent the middle cerebral artery occlusion procedure: 8 euthanized after 24 hours and 8 after 72 hours. All procedures were approved by the University of Washington Institutional Animal Care and Use Committee.

Ultrasound Image Acquisition

Anesthesia was induced in the animals by inhalation of 3% isoflurane and maintained at 1% to 2% isoflurane during data acquisition. Hair was removed from the head to decrease attenuation of ultrasound caused by air trapped within the hair. The skull and skin were left intact. A custom-made polyvinyl alcohol standoff[9] was used to maintain an optimal distance of approximately 30 mm between the transducer and the bottom of the mouse brain. Ultrasound gel (Polysonic multipurpose gel; Cone Instruments, Solon, OH) was applied to the mouse and the standoff. The standoff was placed over the mouse.

An Aixplorer multiwave ultrasound system (SuperSonic Imagine, Aix-en-Provence, France) with its linear SL 15–4-MHz transducer was used to measure the shear modulus of brain tissue in our animals. The transducer's imaging frequency ranged between 4.0 and 15.0 MHz, with a standard center frequency of 8.5 MHz. Two types of images were collected: shear wave elastography and B-mode. B-mode imaging assessed the 2-dimensional anatomy of the brain region from the echoes returning from tissue of different density.[10] The B-mode gain was adjusted for clear visualization of the skull. Shear wave elastography uses ultrasound-generated shear wave propagation to measure the absolute tissue elasticity displayed per pixel. In the shear wave elastographic mode, the penetration depth was approximately 30 mm.[7] Imaging was performed within a range of 0 to 180 kPa in an unblinded fashion to minimize gross imaging artifacts associated with the surrounding tissue and skull (Figure 2), since typical brain shear modulus values lie between 2.7 and 25 kPa, as reviewed below. This method therefore blinded the user to the imaging of the brain itself.[6,11]

Figure 1. Shear wave propagation within a tissue phantom. **A**, Shear wave propagation with no lesion at an early time. **B**, Shear wave propagation with scattering from a lesion on the top left side at an early time. **C**, Shear wave propagation with no lesion at a later time. **D**, Shear wave propagation with scattering from a lesion on left side at a later time. **A** and **C** show propagation without undue complexity in the shear wave, whereas **B** and **D** show the back-propagation of a portion of the shear wave due to its scattering by a lesion in the tissue phantom. Averaging of signals over time derived from shear waves propagating in multiple directions causes a given feature in the tissue to appear bigger than it is. The color scheme describes axial displacement in the direction of the transducer (top). Red represents maximum positive displacement, whereas blue represents maximum negative displacement. The color scale of each image is adjusted for the maximum and minimum displacement values for that particular image.

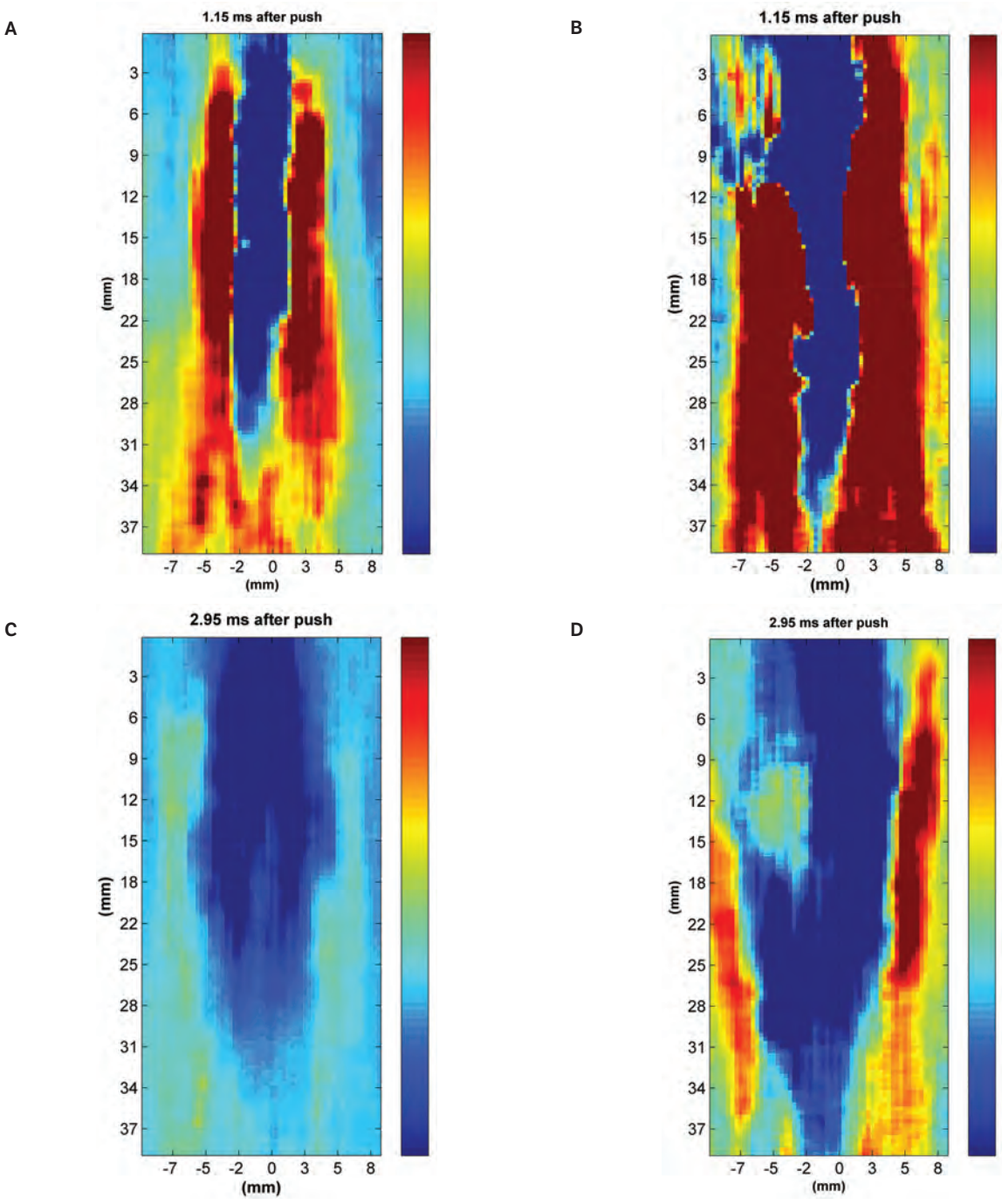

Specifically, ultrasound gel was applied to the ultrasound transducer, itself placed on the standoff. Coronal images of the mouse head including the brain were obtained. We defined the region of interest as the brain. The ultrasound was beamed into the brain inside the skull from its superior to its inferior aspect. The grayscale gain was adjusted to compensate for attenuation. The grayscale gain was set as low as possible to obtain a clear image and give priority to the quality of the shear wave image. The selected shear wave imaging region was reduced to the smallest size that still encompassed the brain to reduce the presence of artifacts from outside the mouse skull. The shear wave gain was adjusted for the same reason. The transducer was moved along the anteroposterior axis of the brain. Multiple coronal images were taken from the front, middle, and back sections of the brain. Image artifacts associated with the skull were avoided as much as possible when selecting images in the shear wave elastographic mode. Approximately 3 to 6 images were taken from each section of the brain.

2,3,5-Triphenyltetrazolium Chloride Staining

Mouse brains were removed after cervical dislocation and cut into eight 1-mm coronal sections. Slices were stained with 0.1% 2,3,5-triphenyltetrazolium chloride (TTC; Sigma-Aldrich, St Louis, MO) in phosphate-buffered saline for 40 minutes to 1 hour at room temperature in the dark (see Figure 3E). They were then fixed in 4% formalin and stored at 4°C. Nine mice that showed no infarct through TTC stain was excluded from the study.

Ultrasound Image Analysis

Ultrasound images were chosen for analysis from the same section of the brain (front, middle, or back) that showed an infarct after TTC staining. We chose 1 of the approximately 5 ultrasound images per mouse that had minimal imaging artifacts (eg, Figure 3A). Since the volume in the murine skull is small, shear waves reflect and scatter off the skull (eg, Figure 1, B and D). During the image-averaging process intrinsic to this commercial machine, the result is imaging artifacts that appear as high shear modulus areas, with their basis in the skull, that diffuse into the brain region. As in the study by Derieppe et al[8] on assaying kidney stiffness, discussed below, our postprocessing of the images sought not to highlight particular intrahemispheric features of brain but instead to simply avoid specific imaging artifacts and develop measures for average intrahemispheric brain tissue stiffness for comparison with control-derived stiffness images.

All postprocessing of the images was done with MATLAB (The MathWorks, Natick, MA). In postprocessing, the entire brain region within the skull was manually selected by a freehand technique using MATLAB software applied to the shear wave elastographic image obtained from the Aixplorer system (Figure 3B). Because the shear wave elastographic image shows the elastographic image on top of the B-mode image, the operator can directly select the portion of the brain within the cranium based on the structure of the skull seen in B-mode. After the selection,

Figure 2. A, Shear wave elastographic image from a mouse with middle cerebral artery occlusion showing a substantial image artifact (hot colors) diffusing intracranially. **B**, The skull can be distinguished in the B-mode image.

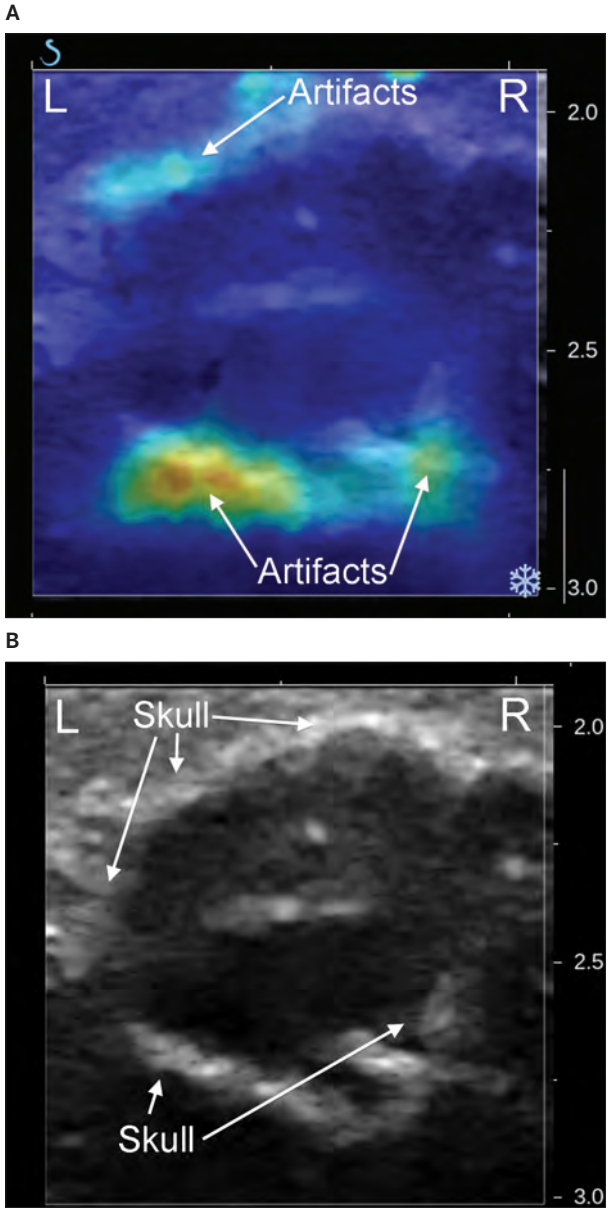

the elastographic image of the selected brain region was compressed to an elasticity range of 0 to 35 kPa (from 0–180 kPa) for increased visualization and contrast within the brain, which tends to have a lower shear modulus than the skull (Figure 3C). The ipsilateral and contralateral hemispheres of the brain were then manually selected directly from the elastographic image of the brain (Figure 3D). These regions were selected with care to avoid skull and imaging artifacts from the skull. These image artifacts are defined as areas with a high shear modulus (greater than that of the brain and tied anatomically to the skull) that extend from outside the brain into the brain region (Figure 3D). The shear moduli of the two hemispheric selections were then averaged to obtain a mean shear modulus for each mouse brain.

This feature extraction analysis was performed 3 times for each image in a blinded fashion to ensure that there was no operator bias. As an example of the robustness of this procedure, Figure 4 shows 3 region of interest analyses derived in a blinded fashion from the same raw shear wave elastographic image. The images were coded so that the operator did not know whether the image was from control, 24-hour stroke, or 72-hour stroke mice.

Finally, all selections were reviewed a posteriori, and shear wave elastographic selections (Figure 3D) were compared to TTC histologic specimens (Figure 3E) to ensure that all region of interest selections from the shear wave elastographic images included areas of damage according to TTC staining.

2,3,5-Triphenyltetrazolium Chloride Image Analysis

The TTC-stained brain slices were optically scanned. The operator who performed the TTC image analysis was blinded to whether the mouse had a stroke for 24 or 72 hours. By the same freehand technique described above, the entire portion of the image that contained brain was selected. The core infarct area was then selected. This area is distinguished by tissue that did not pick up the stain (white). The penumbra, surrounding the core, also includes damaged tissue but is less obviously distinguishable with the TTC stain. The number of pixels in the core infarct area was divided by the number of pixels within the entire brain. With this information, the percentage of the brain that contained a core infarct was calculated. The selection of the infarct area was done 3 times for every image, and the percentage of the brain with an infarct was averaged over the 3 images.

Data Analysis

Mean shear modulus values were normalized for each individual mouse. The mean shear modulus (G) of each hemisphere was divided by the average of the two hemispheres for each mouse:

$$G_{\mathrm{N\,ipsi}} = \frac{G_{\mathrm{ipsi}}}{\frac{G_{\mathrm{ipsi}} + G_{\mathrm{contra}}}{2}}$$

$$G_{\mathrm{N\,contra}} = \frac{G_{\mathrm{contra}}}{\frac{G_{\mathrm{ipsi}} + G_{\mathrm{contra}}}{2}} \quad .$$

The normalized shear modulus (G_{N}) reports the value of the shear modulus of each hemisphere for each given mouse relative to the average value across the entire brain. Note that a normalized value of 1 means that contralateral and ipsilateral hemispheres have the same average shear modulus.

The Student t test was used to compare the average shear modulus for each hemisphere (ipsilateral and contralateral) for 3 populations: control, 24-hour, and 72-hour mice. The t test values were calculated between respective hemispheres (contralateral or ipsilateral) among the 3 populations to see whether the mean shear modulus differed significantly between populations. The Student t test was also performed on the data for ipsilateral and contralateral hemispheres for each population to identify interhemispheric differences. Box plots showing the spread of normalized mean shear modulus values from control, 24-hour, and 72-hour mice were prepared for each hemisphere in SigmaPlot (Systat Software, Inc, San Jose, CA).

Results

Percentage of Stroke-Damaged Tissue

The area of infarct for 72-hour animals (mean, 15.2%) did not vary in a statistically significant fashion from the area of infarct for the 24-hour animals (mean, 10.9%; $P = .20$).

Normalized Shear Modulus of Hemispheres

Average normalized stiffness values for ipsilateral and contralateral brain hemispheres were measured, and the results are summarized in Figures 5 and 6 and Table 1. Figure 5A and Table 1 show that 24-hour animals had a significantly decreased ipsilateral shear modulus compared to control animals ($P < .01$). There was no difference between ipsilateral 72-hour stroke and control animal shear modulus values ($P = .09$). In addition, there was no difference between ipsilateral 72- and 24-hour stroke animal shear modulus values ($P = .13$).

The contralateral hemisphere of 24-hour stroke animals showed a significant increase in elasticity when compared to

Figure 3. Stroke image processing in a mouse with 72-hour middle cerebral artery occlusion. **A**, Aixplorer images in the shear wave elastographic mode (top) and B-mode (bottom). **B**, The brain was selected from the elastographic image (0–180 kPa) displayed on top of the corresponding B-mode image. There is a visible area with a lower shear modulus value in the right hemisphere (dark blue). **C**, The elastographic image of the entire brain was scaled to 0 to 35 kPa to enhance the contrast. Regions of high stiffness indicate image artifacts. **D**, The hemispheric regions to be analyzed were selected manually by the operator to avoid the skull and artifacts (hot color regions associated with large shear modulus values). **E**, Corresponding TTC histologic specimen from the same mouse showing damage in the right hemisphere, distinguished by the white region. This damage correlates with the location of the low shear modulus seen in the elastographic images.

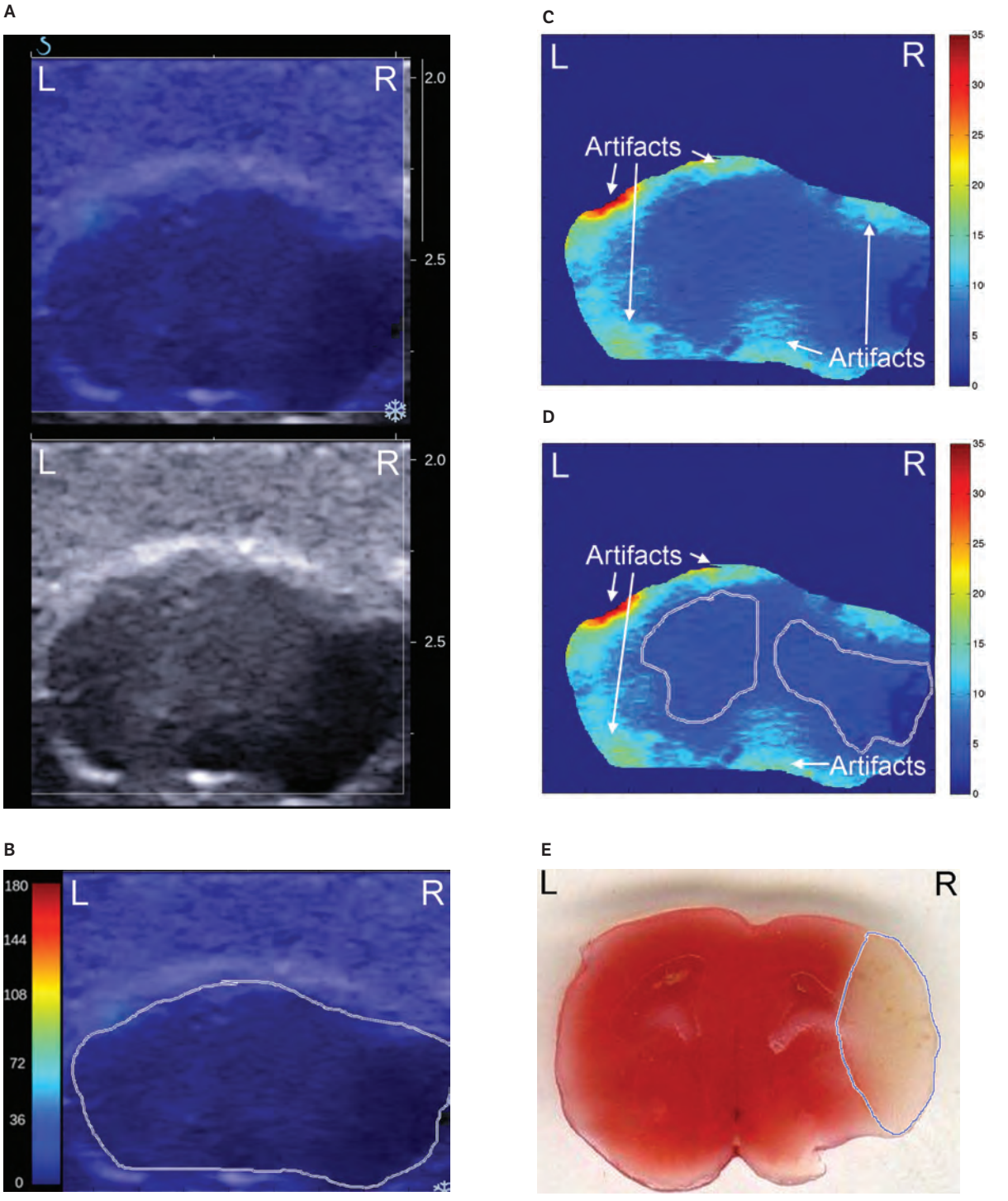

the control population ($P < .01$; Figure 5B). At 72 hours, stroke and control populations exhibited no difference ($P = .09$), nor was there a difference between contralateral hemisphere elasticity values at 24 versus 72 hours after stroke ($P = .13$).

Figure 6 shows that there was a difference between ipsilateral and contralateral shear modulus values both 24 and 72 hours after stroke ($P < .01$). There was also a weak difference in the interhemispheric shear modulus for the control animals ($P = .04$).

Discussion

Our observations included a weak but statistically significant difference ($P = .04$) between the stiffness measures of the 2 hemispheres of the control brain. This observed difference was more significant for the interhemispheric stiffness of brains in mice at both 24 and 72 hours after stroke ($P < .01$). We have therefore chosen to make our assertions of statistical significance at the more stringent *P* value of .01. This relatively weak difference for control animals could have arisen because of asymmetries in delivery of the focused ultrasonic pulse generated by our system or could reflect a real but weak interhemispheric difference in blood content between each hemisphere, due to the asymmetric input of blood from the heart into the brain.

Comparison to Other Measures of Brain Tissue Stiffness

Previous work describing magnetic resonance elastography has shown shear modulus measurements similar to what we found.[6,11] Kruse et al[6] reported the stiffness of white matter as 13.6 kPa and that of gray matter as 5.22 kPa in a study of 25 healthy people, whereas Green et al[11] reported findings that white matter measured 3.1 kPa and gray matter measured 2.7 kPa in a study of 5 healthy men. Moreover, recent work by Mace et al[12] using a research version of the clinical ultrasound machine we used reported shear modulus values from rat brain ranging between 2 and 25 kPa, with an average of 12 kPa.

Although our studies did not distinguish between white and gray matter of the brain, our elastographic measurements of tissue stiffness (4.32 kPa, control ipsilateral; and 4.49 kPa, control contralateral) are within the values noted for magnetic resonance elastography and research sonoelastographic machines.

Changes in the Ipsilateral Hemisphere

In animals 24 hours after stroke, the shear moduli of the ipsilateral hemispheres were significantly less than those of control animals. This finding was likely due to ischemia caused directly by the occlusion as well as the rapid development of edema.[4] According to Gotoh et al,[3] edema in the ipsilateral hemisphere can start developing a few hours after middle cerebral artery occlusion, increasing until it reaches a maximum at around 2 to 3 days. Edema slows the propagation of shear waves, thereby directly affecting the shear modulus of the tissue.[7] Magnetic resonance elastography of the brain has also shown that edema leads to a decrease in elasticity.[13] Ischemic brain edema results initially from cell swelling (cytotoxic edema) caused by depleted

Figure 4. A–C, Representative selections of average hemispheric shear moduli chosen for blinded analysis.

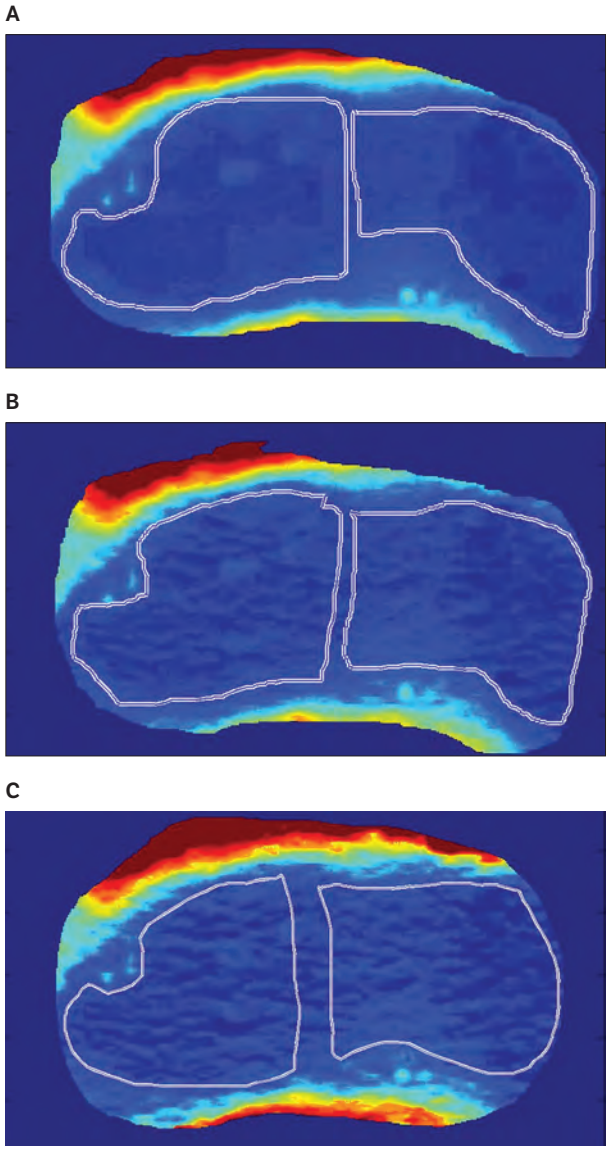

energy substrates in brain cells by ischemia. Eventually, vasogenic edema also develops, caused by increased blood vessel permeability.[14] Vasogenic edema causes the fluidity of the tissue to increase with a decrease in elasticity.[15] The decrease in ipsilateral elasticity reported here is also consistent with the work of Rousseaux and Steinling,[16] who found mean cerebral blood flow values in stroke patients to be generally lower than those of control participants in the ipsilateral hemisphere. Finally, this observation is also consistent with very recently published work on the elasticity of rat brains after stroke.[17]

In animals 72 hours after stroke, the mean ipsilateral shear moduli were not significantly different from those of control animals. One possible explanation is that brain edema ipsilateral to stroke reaches a maximum 2 to 3 days after ischemic injury and then began to decrease.[3] Another explanation is the evolution of intracranial pressure after stroke discussed by Jiang et al 2011,[18] who, in a rat model of middle cerebral artery occlusion stroke, found that intracranial pressure increased throughout the times they measured (up to 24 hours after the procedure). Perhaps an increase in intracranial pressure, caused by the buildup of edema in the brain, eventually worked to stiffen the tissue. Therefore, the average stiffness of the ipsilateral brain at 72 hours may have decreased back to baseline because of a combination of reduced edema relative to 24 hours, continued ischemia, and increasing intracranial pressure.

Changes in the Contralateral Hemisphere

We hypothesize that the observed increase in contralateral hemispheric tissue elasticity for the 24-hour animals arose because of a reduction in contralateral cerebral blood flow[1,16] in combination with elevated intracranial pressure created by the large volume of edema formed in the ipsilateral hemisphere. Although Warner et al[19] and Kim et al[20] showed that elasticity decreases with decreased perfusion, these experiments were done in the liver and kidney, where the internal pressure applied by the blood within the freely suspended organs provides a meaningful source of tissue stiffness, quite like air blown into a balloon. In contrast, the brain is enclosed within a hard skull, nearly filling it. After stroke, observations show not only a reduction in fluid content within the brain contralateral to stroke but also increased intracranial pressure within the entire cranium. Increased intracranial pressure (measuring high at least 24 hours after middle cerebral artery occlusion induction[18]) will put pressure on contralateral (as well as ipsilateral) brain tissue. Therefore, brain tissue may increase in stiffness contralateral to stroke due to both the intracranial pressure increase and the reduction in fluid content within the contralateral hemisphere, instead of sagging like liver or kidney. At 72 hours, the elasticity values for the contralateral cerebral hemisphere of stroke animals are no different than those of control animals. Observations by Gotoh et al[3] show that edema develops in the contralateral hemisphere after infarction and reaches a peak within 2 to 3 days of infarction. We hypothesize that development of edema may decrease the overall tissue elasticity due to increasing fluid content, accounting perhaps for the difference seen between contralateral tissue stiffness in 24- and 72-hour animals.[18]

Figure 5. A, Normalized ipsilateral shear modulus values for control, 24-hour, and 72-hour mice. **B**, Normalized contralateral shear modulus values for control, 24-hour. and 72-hour mice. *$P < .01$.

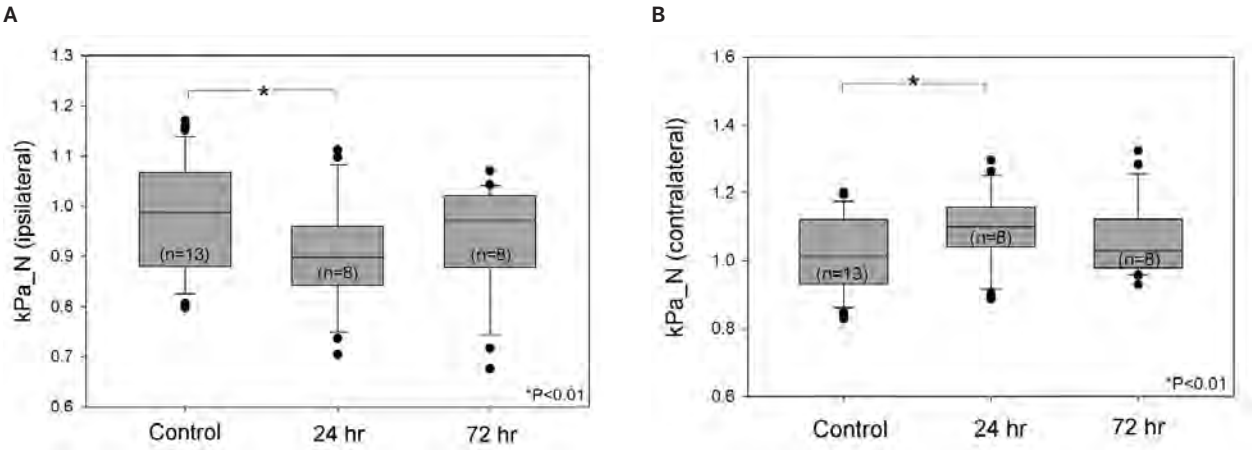

Table 1. Non-Normalized and Normalized Shear Modulus Values for Control, 24-Hour, and 72-Hour Populations

Parameter	Control	24 h	72 h
Ipsilateral non-normalized, kPa	4.32 ± 1.44	3.85 ± 0.96	3.66 ± 1.02
Contralateral non-normalized, kPa	4.49 ± 1.32	4.86 ± 1.79	4.23 ± 1.49
Ipsilateral normalized	0.98 ± 0.11	0.90 ± 0.10	0.94 ± 0.10
Contralateral normalized	1.02 ± 0.11	1.10 ± 0.10	1.06 ± 0.10

Values are mean ± SD.

Limitations

The work as presented takes advantage of the averaging performed within the ultrasound machine to develop estimates of the intrahemispheric average of brain tissue stiffness. This process is at the cost, however, of the requirement that we minimize the influence on our analysis of the imaging artifacts that arise through the imaging procedure itself. To reduce the influence of these features in the images on our quantitative results, we performed individual analyses of each shear wave image in triplicate, in a blinded fashion, to highlight portions of the brain likely independent of those artifacts that also overlap with damage assessed separately, via histologic examination. We have also made careful comparisons with the same shear wave image analysis on control tissue. Performing more detailed analysis requires access to the shear wave propagation data themselves (again, Figure 1), so that we can analyze down to the millimeter scale the propagation of a given shear wave within a given hemisphere of brain. Mace et al[12] have successfully performed this detailed analysis in large and normal rat brains through a large cranial window, using a research version of the commercial device we had for our use. We have begun this kind of analysis and anticipate reporting on it in future work.

Our analysis allow us to hypothesize that a variety of physiologic processes associated with stroke (edema formation, intracranial pressure variations, and alterations of cerebral blood flow) explain the changes in the mechanical properties of brain tissue we observed using intrahemispheric averages of the ultrasound-derived brain tissue shear modulus. Clearly, future studies are required to test these hypotheses. Specifically required are measurements of intracranial pressure and the extent and time course of edema in both hemispheres of the brain along with cerebral blood flow simultaneous with direct imaging of intrahemispheric structures within the brain to verify and further analyze the features of the brain we inferred after stroke.

Figure 6. Comparison of normalized mean shear modulus values of ipsilateral and contralateral hemispheres for control, 24-hour, and 72-hour populations. *$P < .01$; **$P = .04$.

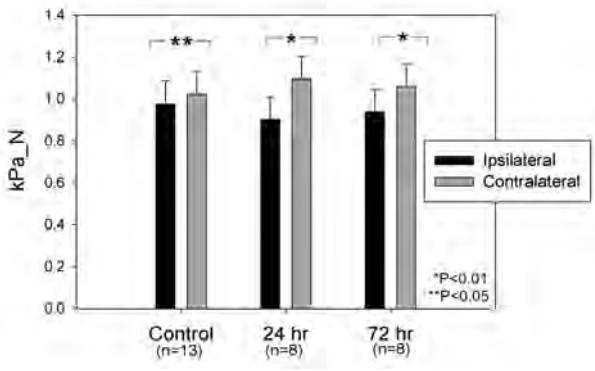

Future Work

Changes in the distribution of fluids within the brain (blood and edema) as well as intracranial pressure have been observed after stroke, based on MRI and positron emission tomography as well as direct analysis of tissue in both the ipsilateral and contralateral hemispheres.[1,3,4,14,16] Using ultrasound-based elastography, we have observed changes in brain stiffness consistent with those physiologic observations, including diaschisis. Successful testing of these hypotheses should motivate future imaging work in humans after stroke and the possible application of this imaging modality in the clinic. For example, the portable and economical aspects of the technology we have used may prove to have an impact on the management and detection of stroke in areas where computed tomography and MRI are not readily available or appropriate.

References

1. Andrews RJ. Transhemispheric diaschisis: a review and comment. *Stroke* 1991; 22:943–949.
2. Han DH, Jung HW, Lee SH, Kim HJ, Choi KS, Sim BS. Acute cerebral infarction and changes of regional cerebral blow flow (rCBF) following

experimental middle cerebral artery (MCA) occlusion. *Neurol Res* 1988; 10:203–212.

3. Gotoh O, Asano T, Koide T, Takakura K. Ischemic brain edema following occlusion of the middle cerebral artery in the rat, I: the time courses of the brain water, sodium and potassium contents and blood-brain barrier permeability to ^{125}I-albumin. *Stroke* 1985; 16:101–109.
4. Izumi Y, Haida M, Hata T, Isozumi K, Kurita D, Shinohara Y. Distribution of brain oedema in the contralateral hemisphere after cerebral infarction: repeated MRI measurement in the rat. *J Clin Neurosci* 2002; 9:289–293.
5. Garra BS. Elastography: current status, future prospects, and making it work for you. *Ultrasound Q* 2011; 27:177–186.
6. Kruse SA, Rose GH, Glaser KJ, et al. Magnetic resonance elastography of the brain. *Neuroimage* 2008; 39:231–237.
7. Tanter M, Bercoff J, Athanasiou A, et al. Quantitative assessment of breast lesion viscoelasticity: initial clinical results using supersonic shear imaging. *Ultrasound Med Biol* 2008; 34:1373–1386.
8. Derieppe M, Delmas Y, Gennisson JL, et al. Detection of intrarenal microstructural changes with supersonic shear wave elastography in rats. *Eur Radiol* 2012; 22:243–250.
9. Fromageau J, Brusseau E, Vray D, Gimenez G, Delachartre P. Characterization of PVA cryogel for intravascular ultrasound elasticity imaging. *IEEE Trans Ultrason Ferroelectr Freq Control* 2003; 50:1318–1324.
10. Mourad P. Biological effects of ultrasound. In: Webster JL (ed). *Encyclopedia of Electronics and Electrical Engineering*. Vol 2. Philadelphia, PA: John Wiley & Sons; 1999:368–386.
11. Green MA, Bilston LE, Sinkus R. In vivo brain viscoelastic properties measured by magnetic resonance elastography. *NMR Biomed* 2008; 21:755–764.
12. Mace E, Cohen I, Montaldo G, Miles R, Fink M, Tanter M. In vivo mapping of brain elasticity in small animals using shear wave imaging. *IEEE Trans Med Imaging* 2011; 30:550–558.
13. Larrat B, Pernot M, Aubry JF, et al. MR-guided transcranial brain HIFU in small animal models. *Phys Med Biol* 2010; 55:365–388.
14. Rosenberg GA. Ischemic brain edema. *Prog Cardiovasc Di*s 1999; 42:209–216.
15. Kuroiwa T, Ueki M, Ichiki H, et al. Time course of tissue elasticity and fluidity in vasogenic brain edema. *Acta Neurochir Suppl* 1997; 70:87–90.
16. Rousseaux M, Steinling M. Crossed hemispheric diaschisis in unilateral cerebellar lesions. *Stroke* 1992; 23:511–514.
17. Martin A, Mace E, Boisgard R, et al. Imaging of perfusion, angiogenesis, and tissue elasticity after stroke. *J Cereb Blood Flow Metab* 2012; 32:1496–1507.
18. Jiang X, Cheng CB, Fang M, Jiang WQ, Zhu GF, Zeng HK. Effect of hydroxyethyl starch on intracranial pressure and plasma colloid osmotic pressure in rats with cerebral ischemia/reperfusion injury [in Chinese]. *Zhongguo Wei Zhong Bing Ji Jiu Yi Xue* 2011; 23:166–168.
19. Warner L, Yin M, Glaser KJ, et al. Noninvasive In vivo assessment of renal tissue elasticity during graded renal ischemia using MR elastography. *Invest Radiol* 2011; 46:509–514.
20. Kim SU, Kim JK, Park YN, Han KH. Discordance between liver biopsy and Fibroscan® in assessing liver fibrosis in chronic hepatitis B: risk factors and influence of necroinflammation. *PloS One* 2012; 7:e32233.

Detection of mild traumatic brain injury in rodent models using shear wave elastography: preliminary studies.

Zinnia S. Xu[1], Anning Yao[1], Stephanie S. Chu[1], Marla K. Paun[2], Abbi M. McClintic[2], Sean P. Murphy, Ph.D.[3], Pierre D. Mourad, Ph.D.[1,2,3].

[1]Department of Bioengineering
University of Washington
Box 356470
Seattle, WA 98195

[2]Applied Physics Laboratory
University of Washington
Box 355640
Seattle, WA 98195

[3]Department of Neurological Surgery
University of Washington
Box 356470
Seattle, WA 98195

Corresponding Author:
Pierre D. Mourad
Department of Neurological Surgery
University of Washington
Box 356470
Seattle WA 98195

(main)	206-543-3570
(fax)	206-543-6785
(office & voicemail)	206-543-9125
(email)	pierre@apl.washington.edu

for submission to European Radiology

Abstract

Objectives: Traumatic brain injury (TBI) can cause adverse physiological changes in fluid content within brain, which may lead to changes in tissue elasticity (e.g., stiffness). This study evaluated the ability of ultrasonic shear wave elastography (SWE) imaging to observe these changes in brain after TBI, *in vivo*.

Methods: Mice and rats received a mild TBI or sham surgery and were imaged acutely or 24 hours after injury using SWE and the hemispheric stiffness values were compared.

Results: Stiffness values were consistent across brain hemispheres of sham TBI rodents. By 24 hours after TBI, relative brain-tissue stiffness values for mice and rats each decreased ipsilaterally and increased contralaterally, both relative to each other and as compared to sham TBI rodents ($p<0.05$). The absolute value of tissue elasticity increased for rats ($p<0.05$) but not for mice.

Conclusion: Differences between intra-hemispheric stiffness values of rodent brain by 24 hours after mild TBI may reflect the observed edema and hemorrhage ipsilateral to TBI, and the known reduction of cerebral blood flow in both brain hemispheres. If these hypotheses hold true, ultrasonic shear wave elastography may offer a method to detect adverse changes in fluid content within brain after mild TBI.

Keywords: Brain; Edema; Elastography; Ultrasound; Traumatic Brain Injury;

Key Points – 3 to 5 points (each point can be 12 words max)

- Ultrasound elastography detects changes in brain stiffness following traumatic brain injury (TBI)
- Edema, hemorrhage, and reduced intra-cerebral blood flow occur after TBI.
- Ultrasound elastography visualizes these occurrences by detecting changes in tissue fluid content.
- This technique may find clinical utility if applied transcranially to humans.

Abbreviations and acronyms

TBI: Traumatic Brain Injury.

CCI: Controlled Cortical Impact.

ICP: Intracranial Pressure.

CPP: Cerebral Perfusion Pressure

Introduction

Incidence of traumatic brain injury (TBI) has increased significantly in recent years owing to the growing use of improvised explosive devices (IEDs) in operations in the Middle East [1]. TBI also occurs among civilians, primarily caused by falls, motor vehicle accidents, struck by/against events, contributing up to 30% of injury-related deaths [2].

CT and MRI are the current civilian standards for imaging traumatic brain injury, with CT more commonly available, thanks to its speed and relatively low cost. It is therefore generally used acutely, if available, while MRI finds more use a few days after initial injury because of its sensitivity to blood products [3]. Both imaging technologies are often insufficiently accessible for military TBI (Ken Curley, MD, personal communication) with the additional requirement of patient transport to the imaging site, relevant in either the civilian or military context. Transcranial ultrasound imaging offers a rapid, portable and point-of-care system for imaging brain but lacks sufficient contrast to provide much diagnostic utility [4].

Here we consider ultrasonic shear wave elastography (SWE) as a possible alternative or adjunct to CT and MR imaging. SWE creates images of Young's Modulus, a measure of the resistance to such that larger values describe stiffer tissue. Therefore, maps of Young's Modulus describe the spatial dependence of tissue shear elasticity or stiffness. The SWE system works by generating within tissue a rapid, net axial displacement of tissue. This spatially focal impulse force then creates a shear wave that propagates outward from the 'pushed' region [5-7]. SWE systems use diagnostic ultrasound to track the propagating shear wave, with the existing commercial system from SuperSonic Imagine (SSI) translating the square of that local speed into a local value of Young's Modulus [5].

SWE via the SSI clinical system has found well-documented use on humans for large and primarily homogenous organs such as breast [5, 8-9]. Studies exist that have used the clinical system in animal models of disease such as kidney [10] and ischemic cerebral stroke [11]. Relevant here, Xu et al [11] resolved inter-hemispheric differences in the stiffness of mouse brain after complete occlusion of the middle cerebral artery. They hypothesized that known formation of edema and ischemia due to stroke ipsilateral to the occlusion and diaschisis contralateral to the occlusion caused the observed inter-hemispheric differences in stiffness.

When using small animal models internal scatter of the shear wave can produce aliasing in stiffness images [10-12]. Indeed, Macé et al. [12] used a research version of the

SSI to remove this aliasing effect by tracking individual shear waves between scattering events. Their maps of brain-tissue stiffness displayed intra-hemispheric features in exquisite detail.

As a first step towards the goal of making SWE applicable to human brain, we used SWE images from the SSI of the brains of rats and mice that received a focal traumatic brain injury to analyze the temporal evolution of the stiffness of brain associated with that injury.

Materials and methods

All animal procedures were approved by the Institutional Animal Care and Use Committee (IACUC) of the University of Washington and the US Army Medical Research and Materiel Command (USAMRMC) Animal Care and Use Review Office (ACURO).

Animal techniques

Surgery

Fifteen male Sprague Dawley rats (250-300 grams, Charles River) and fifteen male mitoCFP mice (20-30 grams, bred at the University of Washington [13]) were used. These were divided into three experimental groups for both rats and mice: sham TBI group (n=5), acute TBI group (n=5) and 24-hour TBI group (n=5). We induced mild TBI following the controlled cortical impact (CCI) protocol of Lighthall [14] as refined by Dixon et al [15], which produced a repeatable and localizable cortical contusion.

Anesthesia was induced via inhalation isoflurane (5% isoflurane for rats; 3% for mice) and maintained (2-3% isoflurane for rats; 1-2% isoflurane for mice) during surgery and cortical impact. The surgical technique was nearly identical for rats and mice; therefore we describe the procedure generally referring to the subjects as "rodents."

The rodent was placed in a stereotaxic device within a pneumatic controlled cortical impact device (AmScien Instruments, Richmond, VA, USA) to hold the head steady. A heating pad was used to maintain the core body temperature of approximately 37° C. The surgical site was prepared by shaving the top of the head then application of a lotion hair remover. Prior to surgery, lidocaine (1 mg/kg) was injected subcutaneously to the surgery site. For TBI rodents allowed to survive 24 hours after injury, bupivacaine (1 mg/kg) was also injected subcutaneously to the surgery site and buprenorphine (0.05 mg/kg) was delivered as an intraperitoneal injection.

After establishing an anesthetic plane via toe pinch and respiratory observation, an incision was made from the bregma to just posterior of the lambda suture line and the skull was exposed. A small (of order 1 mm) hole was drilled in the right (ipsilateral) parietal portion of the skull bone using a surgical drill (Dremel, Racine, WI). Bone rongeurs were used to enlarge the drilled hole to approximately 4 mm in diameter between the bregma and lambda of the right parietal bone of each of mice and rats. (For mice this cranial window encompassed nearly the entire cranial vault above the ipsilateral hemisphere of brain. For rats, this hole took up less than 40% of available ipsilateral cranial vault.) The

cranial window was then aligned with the tip of the cortical impact device. At this point sham animals were removed from the apparatus. For TBI animals, the cortical impact device was then fired to create an impact at the surface of the brain of a velocity of 3.5 m/s and a depth of 1.0 mm for rats and 0.5 mm mice.

For sham and acute TBI rats, the ipsilateral cranial window was enlarged after impact to approximately the entire right parietal bone up to the bregma, lambda, and sagittal suture line. For mice we worked with the existing ipsilateral cranial window. For each of the sham and acute TBI rats and mice an identical cranial window was then created on the contralateral side of the skull.

For the rodents in the 24-hour TBI groups, after impact the unilateral cranial window was filled with bone wax. The surgery site was then closed with 3-0 nylon sutures (Covidien, Mansfield, MA, USA) and the rodents were returned to their cages. After 24 hours, these received bilateral craniectomies as described above.

SWE Image Acquisition

After the creation of bilateral cranial windows we imaged the brains of each rodent with a linear SL15-4 MHz transducer of an Aixplorer Multiwave Ultrasound System (SuperSonic Imagine, Aix-en-Provence, France). The transducer's imaging frequency ranged between 4.0-15.0 MHz, with a standard center frequency of 8.5 MHz. Two types of images were collected, Shear Wave Elastography (SWE) and standard B-mode. Images were collected with an elasticity range of 0-180 kPa to minimize gross imaging artifacts associated with the surrounding tissue and skull while blinding the user to intra-hemispheric features at low values of Young's Modulus, which generally lie between 2 and 25 kPa [11-12,16-18].

A micro-positioner was used to maintain the SWE transducer over the rodent's head perpendicular to show coronal slices. Multi-purpose ultrasound lotion (Polysonic, Cone Instruments, Solon, OH, USA) was used to maintain ultrasound conduction between the transducer and the head.

The brain was first imaged using traditional B-mode; combined B-mode and SWE imaging began when the brain had been located and centered in the B-mode image (Fig. 1 A). Significant effort was made to minimize creation of imaging artifacts in the SWE images. These artifacts (e.g., Fig. 1 C,D) are areas of high Young's Modulus that do not correlate with the neuroanatomy [11-12,16-17]. For each rodent, we collected 10 – 30 images. We

selected 3 images where both the impact site was identifiable in the B-mode imaging and had minimal elasticity artifacts.

After imaging the animals were sacrificed and perfused and the brains were harvested for histological analysis. The brains were sectioned through the injury site at 8-10 micron thick that were stained with hematoxylin and eosin (H&E) and, separately, cresyl violet (CV). The slides were digitized and the extent of TBI damage was quantified by manual selection of the injured area using ImageJ.

Post-processing of SWE Images

Image post-processing was completed using MATLAB (Natick, MA, USA). The entire brain region was manually selected in the SWE-mode image obtained from the Aixplorer (Fig. 1 B). The brain region in the SWE image was selected based on the structure of the skull as seen in the corresponding B-mode image.

After the selection of images, the elasticity map of the selected brain region was reduced to display an elasticity range of 0-35 kPa (Fig. 1 C,D), down from 0-180kPa (Fig. 1 A,B). Regions of interest from within each hemisphere of brain tissue within the skull were then manually selected directly from the elasticity map (Fig. 1 D). Regions of comparable size and location but free of imaging artifacts were selected from both hemispheres.

Regional selection and analysis was performed three times for each image and then averaged together to produce the intra-hemispheric average of brain-tissue stiffness for each of the two hemispheres of brain within the image.

Data Analysis

For each image for each rodent, a representative value of the Young's Modulus value of each hemisphere was used directly for analysis as well as normalized by dividing the average value of Young's Modulus for a given hemisphere by the average of the two hemispheres. The normalized Young's Modulus therefore provides a measure of the elasticity of a given hemisphere relative to the average value across the entire brain.

Kruskal-Wallis One Way Analysis of Variance tests on Ranks (ANOVA) was applied to the data using SigmaPlot (Systat Software, San Jose CA).

Results

Quantification of areal extent of damage in H&E and Creysl Violet.

We quantified the anatomical extent of TBI damage as shown histologically (Fig. 1 E,F). There was no difference between groups with regard to the extent of damage shown by H&E versus cresyl-violet stains nor in the extent of damage between the acute and 24-hour groups for either species (Table 1).

Directly measured values of Young's Modulus for rats.

Figure 2 shows directly measured average values of Young's Modulus for each hemisphere of sham, acute, and 24-hour TBI rats. There was no significant difference between average Young's Modulus values within any of the sham or acute or 24-hour TBI groups (Fig. 2 A). We did, however, observe changes in average Young's Modulus between groups. Specifically, each of the contralateral and ipsilateral hemispheric values of the acute and 24-hour TBI groups have values of Young's Modulus that increased significantly relative to their respective values for the sham TBI group (Fig. 2 B).

Normalized values of Young's Modulus for rats.

Figure 3 shows normalized Young's Modulus values for each hemisphere of sham, acute, and 24-hour TBI rats. There was no significant difference between average Young's Modulus values within the sham or acute TBI groups while by 24 hours there existed a significant difference between ipsilateral and contralateral hemispheric averages of normalized Young's Modulus (Fig. 3 A). With regard to between-group changes, by 24 hours after TBI the ipsilateral values of normalized Young's Modulus decreased with time while the contralateral values increased with time (Fig. 3 B).

Directly measured values of Young's Modulus values for mice.

Figure 4 shows directly measured values of Young's Modulus for each hemisphere of sham, acute, and 24-hour TBI mice. There was no significant difference between average Young's Modulus values within the sham group while there exist significant differences between the average ipsilateral and contralateral values of Young's Modulus both acutely and at 24 hours after TBI (Fig. 4 A). Relative to the sham value of Young's Modulus the ipsilateral value decreased by 24 hours after TBI while the contralateral value increased

acutely before returning to a value comparable to the sham value of Young's Modulus (Fig. 4 B).

Normalized values of Young's Modulus for mice.

Figure 5 shows normalized Young's Modulus values for each hemisphere of sham, acute, and 24-hour TBI mice. There was no significant difference between average Young's Modulus values within the sham group. In contrast, the average value of Young's Modulus for the ipsilateral hemisphere was significantly smaller than that of its contralateral value both acutely and at 24 hours after TBI (Fig. 5 A). In addition, by 24 hours after TBI the ipsilateral values of normalized Young's Modulus decreased with time while the contralateral values increased with time (Fig. 5 B).

Discussion

We created mild traumatic brain injury (TBI) in mice and rats using the controlled cortical impact (CCI) paradigm. We then used a commercial diagnostic ultrasound machine to measure intra-hemispheric averages of brain-tissue stiffness (the Young's modulus, a measure of shear resistance of tissue) of the brains both acutely and 24 hours after TBI induction. We presented analysis of both the absolute value and normalized values of brain stiffness, the latter documenting changes in brain-tissue stiffness relative to the average value of the entire brain at a given time point.

We note that tissue stiffness values inferred by ultrasound shear-wave elastography are sensitive to the tissue's net fluid content. For example, all else being equal more fluid as a percentage of tissue decreases the measured stiffness, while less fluid increases the measured stiffness [5]. One can appreciate this view by considering Derieppe et al. [10], whose study of ischemia in kidney showed a decrease in SWE-derived stiffness, and Xu et al. [11], whose study of ischemia in mouse brain showed a decrease in stiffness ipsilateral to injury (a region of extensive edema) and an increase in stiffness contralateral to injury (a region of known reduced cerebral blood flow). Paraphrasing the literature analysis of Xu et al. [11], ischemic brain within a cranium doesn't sag while ischemic kidney within a belly does.

We start with our results for rats. The absolute value of Young's modulus increased through time in each of the ipsilateral and contralateral hemispheres compared to controls (Fig. 2). There exist many physiological processes that occur after TBI that can alter the fluid content of brain that may explain our observations, subject to direct testing. For example, our observed global increase in measured brain-tissue stiffness across hemispheres through time may have arisen due the combined effect of reduced peripheral blood pressure and increased in ICP, which can work together to reduce cerebral perfusion pressure (CPP) hence cerebral blood flow throughout the brain. This hypothesis is consistent with the observations of some researchers [19-20] though not all [21]. Also contributing to this net increase in brain-tissue stiffness may have been a reduction in cerebral spinal fluid (CSF) within the cranium [20]. We note that these hypotheses require that global peripheral (blood pressure) and intracranial (ICP; CPP; cerebral blood flow; CSF) processes more than compensate for the focal increase in fluid content within TBI brain ipsilateral to the injury caused by the observed edema and hemorrhage. That increase in

focal fluid content may itself balance in part the focal ischemia observed by others after CCI [21]. Attention to the normalized data highlights these potentially competing, focal effects.

Specifically, we note that by 24 hours after TBI the normalized value of brain-tissue stiffness within the ipsilateral hemisphere reduced in magnitude relative to controls while its counterpart within the contralateral hemisphere increased in magnitude relative to controls (Fig. 3). Moreover, by 24 hours after TBI the ipsilateral value of normalized brain tissue stiffness was significantly reduced relative to the contralateral value. Because of our choice of normalization technique, these results document changes in brain-tissue stiffness that occur relative to the global rise in the absolute value of brain-tissue stiffness reported above.

With regard to the observed reduction in relative ipsilateral brain-tissue stiffness, we first note the presence and time course of edema and hemorrhage demonstrated by our histology (Fig. 1 E, F and Table 1) and consistent with other's observations[22-23]. In addition to edema, others have documented ischemia measured using laser Doppler velocimetry and whole-brain autoradiography techniques. Specifically, Bryan et al. [21] observed immediate ipsilateral ischemia after severe CCI that lasted at least four hours after injury. We therefore hypothesize that the observed edema formation ipsilateral to injury by 24 hours lowered the normalized value of the measured intra-hemispheric average of brain elasticity compared to that of sham TBI in a manner that more than compensated for the likely effect of ischemia known to occur in at least severe CCI, but undocumented within our experiment, all riding on a wave of global reduction in blood flow due to elevated ICP. This complex hypothesis, besides requiring verification in future studies, is consistent with recent observations of reduced brain-tissue stiffness at the site of CCI in mice relative to the rest of the brain, based on images created with magnetic resonance elastography [24-25].

With regard to the observed increase in contralateral relative brain-tissue stiffness, our observations and those cited above show no edema formation contralateral to the injury while [19], for example, observed decreased cerebral perfusion pressure and reduced cortical perfusion contralateral to the injury, both consistent with our observations.

Our results for normalized values of brain-tissue stiffness observed for mice after TBI (Fig. 5) are consistent with what we observed for rats (Fig. 3). This suggests it possible that the same interplay of ipsilateral edema versus ischemia and global reduction in cerebral blood flow that can occur for rats may also have occurred for mice. Consistent with this idea, Lundblad et al. [26] observed after *severe* CCI significant edema in ipsilateral

cortex, a reduction of cortical blood flow in ipsilateral cortex on time scales of hours to 24 hours and in contralateral cortex by 24 hours. Comparable studies are lacking for mild CCI and warrant future work.

Our measurement of the absolute value of intra-hemispheric brain-tissue stiffness of mouse brain differs significantly, however, from what we observed for rat brain. For example, ipsilateral to the injury site the absolute value of Young's modulus value decreased by 24 hours, rather than increased as for rats. Also, the absolute value of Young's modulus increased acutely contralateral to the injury as for rats, but returned to baseline values by 24 hours after TBI, unlike in rats, which continued to increase. This difference may have arisen due to the large discrepancy in areal extent between the ipsilateral craniectomy required for mice versus that for rats. Specifically, the craniectomy uncovered essentially the entire hemispheric cranial vault for mice while less than half of that vault for rats. Perhaps this relatively large craniectomy reduced the possibility of elevated ICP, hence reduced CPP and cerebral blood flow in our mice. The mouse model may, therefore, only display the effects of intra-hemispheric dynamics (edema, local ischemia) and reduced global cerebral blood flow due to changes in systematic blood pressure rather than the additional effects of global intracranial dynamics (elevated ICP, hence a further decrease in CPP and therefore in cerebral blood flow).

Limitations

This study had several limitations due to its preliminary nature. First and foremost, we've generated a series of largely untested hypotheses regarding the possible impact on measured brain-tissue stiffness due to the relative weights of different fluid sources within brain tissue, motivated by our direct observations and the published literature. These hypotheses require direct testing. Also, out of necessity we performed a relatively large craniectomy to facilitate the CCI method for mice, which may have altered the effects of elevated ICP and reduced CPP known to occur in these animal models. Future studies should target use of larger animal models of TBI to mitigate this possible effect. In addition, we used SWE technology not optimized for rodent brain encased in a skull. The artifacts we observed associated with the skull produced elasticity values that are not consistent with other, published measurements of brain-tissue stiffness, forcing us to carefully select around these artifacts so that they did not confound our data.

Conclusion

We used ultrasound shear-wave elastography to measure absolute as well as normalized values of intra-hemispheric stiffness of rodent brain both acutely and at 24 hours after TBI via the controlled cortical impact (CCI) method. These observed changes in brain-tissue stiffness after TBI may reflect multiple physiological processes known to occur within brain after TBI caused by CCI. These processes include the initial formation of edema and hemorrhage known to develop ipsilateral to TBI and observed by us, as well as the known but un-assayed by us (a) formation of ischemia ipsilateral to TBI, (b) reduction in cerebral perfusion pressure and (c) blood flow observed both ipsilateral and contralateral to TBI. Ultrasound-based elastography may therefore offer a method to monitor subtle changes in brain after TBI.

Future work should target testing the links we have hypothesized between observed changes in brain-tissue stiffness and the underlying physiology of TBI. In addition, future work should address currently identified problems in the translation of this technology to human use, including delivery in a transcranial fashion of a shaped pulse of ultrasound energy sufficient to generate usefully observable shear waves, and the known large-scale anisotropy of human brain and its likely impact on the formulae used to translate shear-wave propagation into estimates of brain-tissue stiffness.

Acknowledgements

We received support for this work from the Congressionally Directed Medical Research Program (CDMRP), Award Number W81XWH-11-2-0109.

Figure Captions

Fig. 1. Image Processing. (A) Aixplorer images in SWE mode (top) and B-mode (bottom) (B) The brain region was selected from the elastographic image (0-180 kPa) with reference to the B-mode image. (C) The SWE image of the brain was rescaled to 0-35 kPa to enhance the contrast. (D) Regions of Interest selected manually to avoid skull and artifacts (large values of Young's Modulus greater than that of brain). (E) Hematoxylin and Eosin and (F) Cresyl Violet staining of corresponding brain.

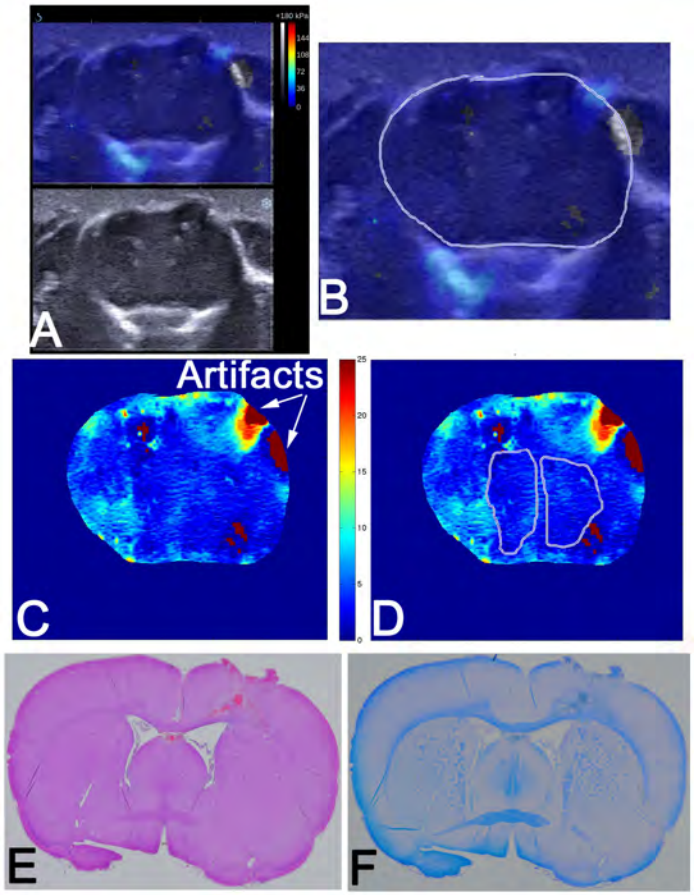

Fig. 2. Directly measured values of Young's Modulus for ipsilateral and contralateral hemispheres of the brains of rats for all test groups. * = $p < 0.05$ between the two indicated groups.

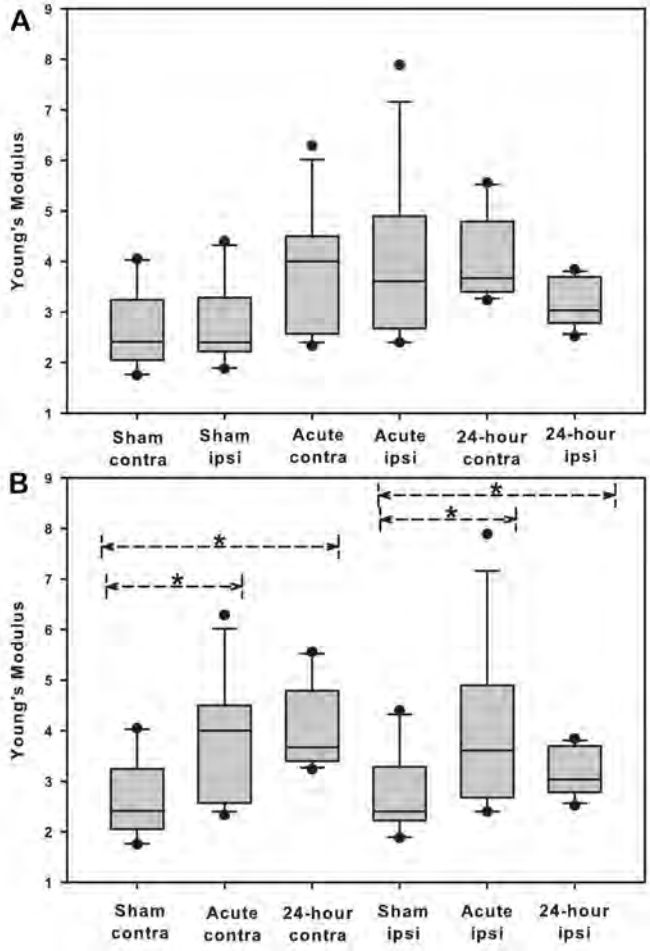

Fig. 3. Values of normalized Young's Modulus for ipsilateral and contralateral hemispheres of the brains of rats for all test groups. * = $p < 0.05$ between the two indicated groups.

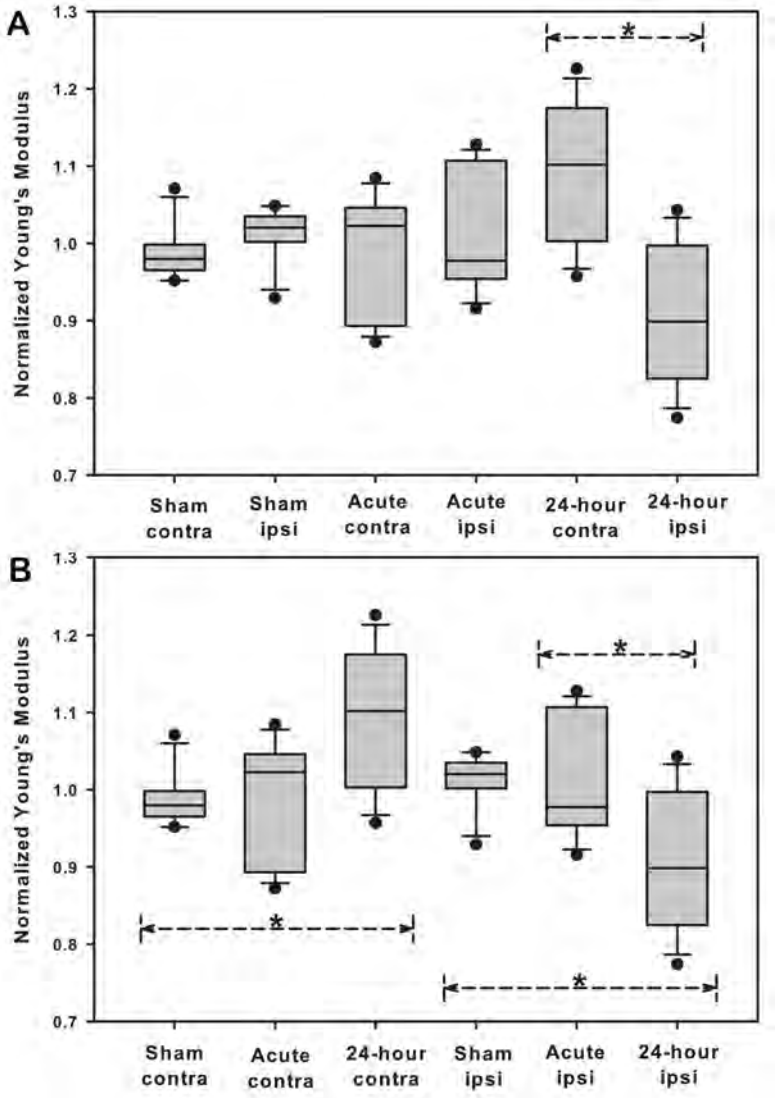

Fig. 4. Directly measured values of Young's Modulus for ipsilateral and contralateral hemispheres of the brains of mice for all test groups. * = $p < 0.05$ between the two indicated groups.

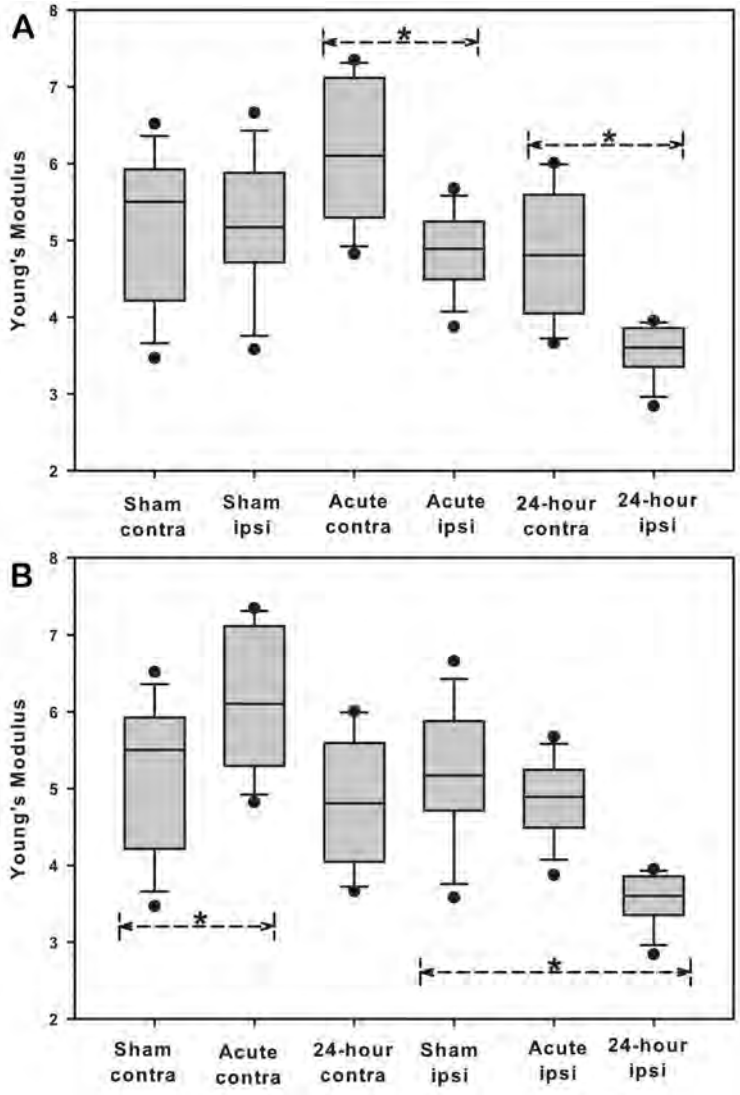

Fig. 5. Values of normalized Young's Modulus for ipsilateral and contralateral hemispheres of the brains of mice for all test groups. * = $p < 0.05$ between the two indicated groups.

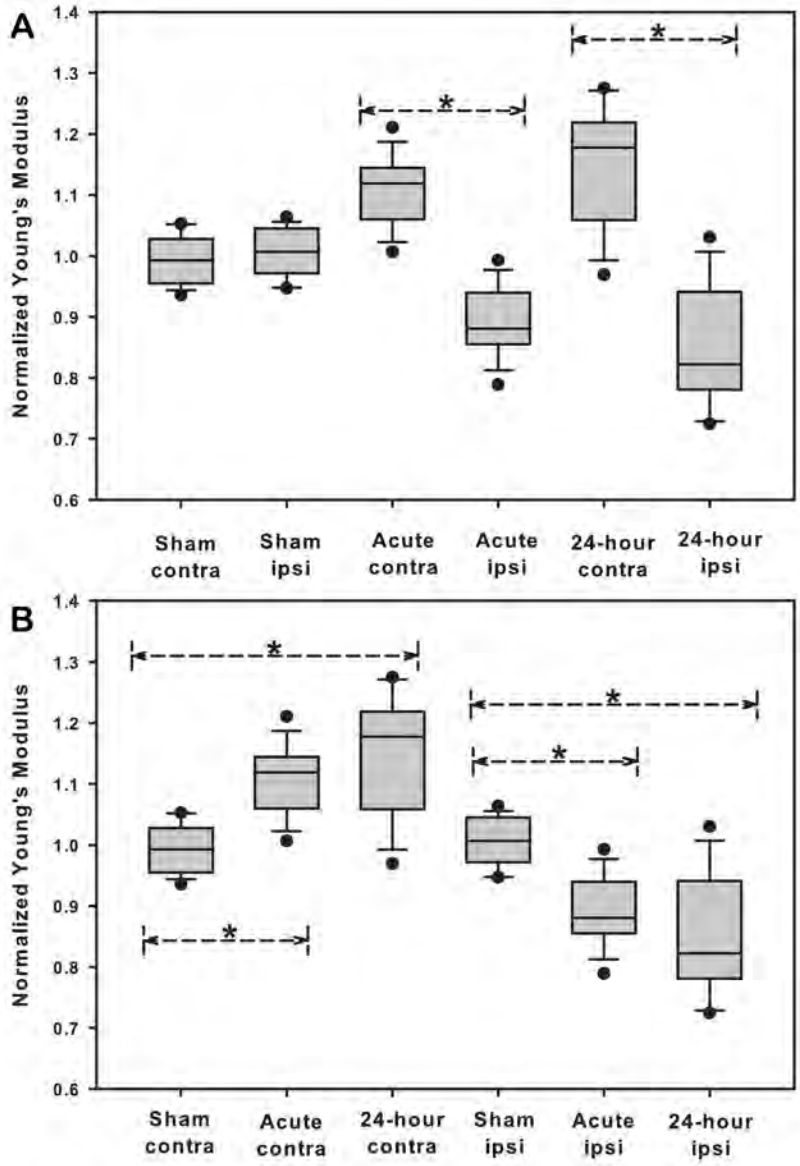

Table 1

Table 1: % extent of damage of TBI in histological analysis.

Stain	Acute Mice	24 Hr Mice	Acute Rats	24 Hr Rats
H&E	8.02% +/- 2.2%	14.2% +/- 7.5%	4.62% +/- 2.7%	7.57% +/- 1.6%
CV	8.33% +/- 0.6%	11.2% +/- 2.7%	4.95% +/- 0.1%	6.98% +/- 2.1%

References

1. Meyer K, Helmick K, Doncevic S, and Park R (2008) Severe and Penetrating Traumatic Brain Injury in the Context of War. J Trauma Nurs 15:185-189.
2. Faul M, Xu L, Wald MM, Coronado VG. Traumatic brain injury in the United States: emergency department visits, hospitalizations, and deaths. Atlanta (GA): Centers for Disease Control and Prevention, National Center for Injury Prevention and Control; 2010.
3. Lee B and Newberg A (2005) Neuroimaging in Traumatic Brain Imaging. NeuroRx 2:372-383.
4. Fryback DG, Thronbury JR (1991) The Efficacy of Diagnoistic Imaging. Med Decis making 2:88-94.
5. Tanter M, Bercoff J, Athanasiou A, Deffieux T, Gennisson JL, Montaldo G, Muller M, Tardivon A, and Fink M (2008) Quantitative assessment of breast lesion viscoelasticity: initial clinical results using supersonic shear imaging. Ultrasound Med Biol 34:1373-86.
6. Deffieux T, Gennisson JL, Larrat B, Fink M, Tanter M (2012) The variance of quantitative estimates in shear wave imaging: theory and experiments. IEEE Trans Ultrason Ferroelectr Freq Control 59(11):2390-410.
7. Gennisson JL, Deffieux T, Fink M, Tanter M (2013) Ultrasound elastography: principles and techniques. Diagn Interv Imaging 94(5):487-95.
8. Athanasiou A, Tardivon A, Tanter M, Sigal-Zafrani B, Bercoff J, Deffieux T, Gennisson JL, Fink M, and Neuenschwander S (2010) Breast lesions: quantitative elastography with supersonic shear imaging--preliminary results. Radiology 256:297-303.
9. Garra BS (2011) Elastography: current status, future prospects, and making it work for you. Ultrasound Q 27:177-86.
10. Derieppe M, Delmas Y, Gennisson JL, Deminière C, Placier S, Tanter M, Combe C, and Grenier N (2012) Detection of intrarenal microstructural changes with supersonic shear wave elastography in rats. Eur Radiol 22:243-50.
11. Xu ZS, Lee RJ, Chu SS, Yao A, Paun MK, Murphy SP, Mourad PD (2013) Evidence of Changes in Brain Tissue Stifness After Ischemic Stroke Derived From Ultrasound-Based Elastography. J Ultrasound Med 32:485-494.
12. Macé E, Cohen I, Montaldo G, Miles R, Fink M, and Tanter M (2011) In vivo mapping of brain elasticity in small animals using shear wave imaging. IEEE T Med Imaging 30:550-8.
13. Misgeld T, Kerschensteiner M, Bareyre FM, Burgess RW, and Lichtman JW (2007) Imaging axonal transport of mitochondria *in vivo*. Nat Methods 4(7):559-561.
14. Lighthall JW (1988) Controlled cortical impact: a new experimental brain injury model. J Neurotrauma 5(1):1-15.
15. Dixon CE, Clifton GL, Lighthall JW, Yaghmai AA, Hayes RL (1991) A controlled cortical impact model of traumatic brain injury in the rat. J Neurosci Meth 39:253-262.
16. Green MA, Bilston LE, and Sinkus R, (2008) In vivo brain viscoelastic properties measured by magnetic resonance elastography. NMR Biomed 21:755-64.
17. Kruse SA, Rose GH, Glaser KJ, Manduca A, Felmlee JP, Jack CR Jr., and Ehman RL (2008) Magnetic resonance elastography of the brain. Neuroimage 39:231-7.
18. McCracken PJ, Manduca A, Felmlee J, Ehman RL (2005) Mechanical transient-based magnetic resonance elastography. Mag Reson Med 53(3):628-39.

19. Cherian L, Robertson CS, Contant CF Jr., Bryan RM Jr. (1994) Lateral Cortical Impact Injury in Rats: Cerebrovascular Effects of Varying Depth of Cortical Deformation and Impact Velocity. J Neurotrauma 11(5):573-585.
20. Colgan NC, Cronin MM, Gobbo OL, O'Mara SM, O'Connor WT, Gilchrist MD (2010) Quantiative MRI Analysis of Brain Volume Changes due to Controlled Cortical Impact. J Neurotrauma 27:1265-1274.
21. Bryan RM Jr., Cherian L, Robertson C (1995) Regional Cerebral Blood Flow After Controlled Cortical Impact Injury in Rats. Anesth Analg 80:687-95.
22. Baskaya MK, Dogan A, Temiz C, and Dempsey RJ (2000) Application of 2,3,5-triphenyltetrazolium chloride staining to evaluate injury volume after controlled cortical impact brain injury: role of brain edema in evolution of injury volume. J Neurotrauma 17:93-9.
23. Elliott MB, Jallo JJ, and Tuma RF (2008) An investigation of cerebral edema and injury volume assessments for controlled cortical impact injury. J Neurosci Meth 168:320-4.
24. Boulet T, Kelso ML, Othamn SF (2011) Microscopic magnetic resonance elastrography of traumatic brain injury model. J Neurosci Meth 201:296-306.
25. Boulet T, Kelso ML, Othman SF (2013) Longterm *in vivo* imaging of viscoelastic properties of the mouse brain following controlled cortical impact. J Neurotrauma. doi: 10.1089/neu.2012.2788.
26. Lundblad C, Grande PO, and Bentzer P (2004) A mouse model for evaluation of capillary perfusion, microvascular permeability, cortical blood flow, and cortical edema in the traumatized brain. J Neurotrauma 21:741-53.